University of Southampton Research Repository

University of Southampton

Nonlinear Dynamics Characterisation of Silicon Nanoelectromechanical Resonators

by

Fang Ben

ORCID: 0000-0002-8486-5583

Thesis for the degree of Doctor of Philosophy

FACULTY OF ENGINEERING AND PHYSICAL SCIENCES
School of Electronics and Computer Science
Group of Smart Electronic Materials and Systems

Supervisors: Dr. Yoshishige Tsuchiya

Dr. Jun-Yu Ou

Dr. Maurits de Planque

August 2023

UNIVERSITY OF SOUTHAMPTON

<u>ABSTRACT</u>

Faculty of Engineering and Physical Sciences
School of Electronics and Computer Science
Group of Smart Electronic Materials and Systems

<u>Doctor of Philosophy</u>

Nonlinear Dynamics Characterisation of Silicon Nanoelectromechanical Resonators

by Fang Ben

Nano-electro-mechanical system (NEMS) resonators have been widely used in multiple applications. However, their nonlinear behaviour has been considered as a nuisance until recent breakthroughs have illuminated the potential applications of nonlinear NEMS resonators such as neuromorphic computing and dynamic range enhancement for sensing applications. A comprehensive characterisation of the nonlinear behaviour is crucial for effective control, particularly in these emerging applications. This thesis reports a novel method to characterise nonlinear dynamics in doubly-clamped NEMS resonators by employing a novel parameter β_m extracted via perturbation series to quantify mechanical nonlinearity. Electrostatic nonlinearity is derived into explicit expression to incorporate with β_m to define the overall nonlinearity of the system. This method successfully explains the observed dependencies of nonlinear characteristics on DC actuation voltage and driving power under frequency modulation and 1-ω mixing measurement schemes. Result shows the value of β_m for NEMS with length of 2, 1.5, 1 μm is -1.5 × 10^{-5}, -5.4× 10^{-5}, -2.8 × 10^{-5} m^{-2}, respectively, regardless of measurement schemes, indicating the β_m is an intrinsic property that only relates to the NEMS material and design. Moreover, this research presents a novel method for identifying the onset of hysteresis with β_m. Through the analysis of NEMS beams of dimensions 2 μm and 1 μm, the hysteresis is expected to occur when DC at 1.61 V and 3.58 V, respectively. This result is later verified by experimental evidence. Furthermore, this study achieves the analysis systematic nonlinear response up to frequencies of 221 MHz, offering insights applicable to scaled NEMS resonators and emerging applications reliant on essential nonlinearity for device and system operations.

List of Content

v

List of Figures

ix

x

List of Tables

Declaration of Authorship

I, Fang Ben, declare that this thesis entitled 'Silicon Nanoelectromechanical Resonator Nonlinear Dynamics Characterisation' and the work presented in it are my own and has been generated by me as the result of my own original research.

I confirm that:

- This work was done wholly or mainly while in candidature for a research degree at this University.
- Where any part of this thesis has previously been submitted for a degree or any other qualification at this University or any other institution, this has been clearly stated.
- Where I have consulted the published work of others, this is always clearly attributed.
- Where I have quoted from the work of others, the source is always given. With the exception of such quotations, this thesis is entirely my own work.
- I have acknowledged all main sources of help.
- Where the thesis is based on work done by myself jointly with others, I have made clear exactly what was done by others and what I have contributed myself.
- Parts of this work have been published as research journals and conference papers. A list of publication is presented within this thesis.

Signed: ……………………………………………………………

Date: ……………………………………………………………

Acknowledgement

I would like to express my heartfelt gratitude to the countless individuals who have supported me throughout my Ph.D. journey within this section.

First and foremost, I want to sincerely thank my supervisor, Dr. Yoshishige Tsuchiya, who has been a steadfast source of support since my master year. His meticulous guidance on my research, patient instruction on the use of measurement systems, and consistent weekly discussions on research-related topics, even during the lockdown period, have been crucial to my development as a researcher. His attention to detail, patience, and encouragement have been instrumental in improving my experimental skills and scientific writing abilities, leading to my successful publication of my first research paper during the COVID-19 pandemic.

I also want to express my appreciation to my second supervisor, Dr. Jun-Yu Ou (known as Bruce), for his invaluable support throughout the project. From the beginning of the project, Bruce has been actively involved in discussions regarding my research data. His assistance in setting up the mixing measurement in my project was essential and greatly contributed to the success of my research. I would also like to extend my gratitude to another supervisor, Dr. Maurits de Planque. His guidance and inspiration during my M.Sc. studies encouraged my interest in pursuing a Ph.D., and I also received his invaluable support during my Ph.D. application process. As one of his last classes of Ph.D. students, I am deeply appreciative of his help, even though he may not have the chance to see this thesis. I wish all the best to his families. R.I.P Maurits.

To my colleague and co-author, James Fernando, throughout many long days and

nights in the laboratory, we supported and encouraged each other. As a non-native English speaker, I was fortunate to have James, who generously proofread my papers for me. He was an excellent helper and friend throughout my four-year Ph.D. journey. I would also like to deliver my appreciation to other friends in SEMS group and ECS who have been supportive of my academic journey. Thank you for your support throughout these unforgettable four years. Please forgive me if I have inadvertently left out any names in my acknowledgments.

Last but not least, I would like to express my sincerest appreciation to my family. I want to thank my cousin, Dr. Yunxiao Zhang from Imperial College, who has been a role model throughout my Ph.D. journey. He provided crucial advice and assistance on my MATLAB usage. Furthermore, I want to express my heartfelt gratitude to my fiancée, Dr. Jinyuan Luo, who has been by my side for the past 10 years. Your love and encouragement during my moments of uncertainty has been instrumental in helping me persevere through my Ph.D. studies. Even though we were more than 10,000 km apart, I can always feel your constant support and affirmation every step of the way. Lastly, I want to pass my deepest appreciation to my parents. They are the utmost reliable harbor of me throughout my Ph.D. journey. They provided all-around support, both mentally and financially, and I could not have imagined pursuing a Ph.D. without them. Their support was the most solid foundation for me to complete my studies in a foreign country.

List of Abbreviations

2D	Two dimensions
4th R-K	4th order Runge-Kutta
AC	Alternating current
A-f	Amplitude-to-frequency
Au	Gold, 'Aurum in Latin'
BAW	Bulk acoustic wave
BESOI-MEMS	Back etched silicon-on-insulator micro-electro-mechanical system
BSIM	Berkeley short-channel insulated-gate-FET Model
CEA-LETI	Commissariat à l'Energie Atomique et aux Energies Alternatives Laboratoire d'électronique des technologies de l'information
CMOS	Complementary metal-oxide semiconductor
CMP	Chemical-mechanical polishing/planarization
CNT	Carbon nanotube
DC	Direct current
DETF	Double-ended tuning fork
DFT	Dynamic field theory
DIBL	Drain-induced barrier lowering
EBT	Euler-Bernoulli theory
FEA	Finite element analysis

FM	Frequency modulation
GIDL	Gate-induced drain leakage
GUI	Graphical user interface
IC	Integrate circuit
IEEE	Institute of Electrical and Electronics Engineers
IoT	Internet of thing
Si-NEMS	nano-electro-mechanical resonator
IP-NEMS	In-plane nano-electro-mechanical system
I-V	Current voltage characterization
MEMS	Micro-electro-mechanical system
MNE	Micro and Nano Engineering
MoS$_2$	Molybdenum disulfide
MOSFET	Metal–oxide–semiconductor field-effect transistor
NEMS	Nano-electro-mechanical system
NRI	Newton-Raphson iteration
OAFM	Optimal auxiliary function method
ODE	Ordinary differential equation
PDE	Partial differential equation
P-G (PGM)	Petrov-Galerkin method
P-L	Poincaré-Lindstedt
PSD	Phase-sensitive detector
PZR	Piezoresistive
RBW	Resolution bandwidth
RC	Reservoir computing

RF	Radio frequency
RMSE	Root mean square error
RRMSE	Relative root mean square error
SDOF	Single degree of freedom
SEM	Scanning electron microscope
SG-MOSFET	Suspended-gate metal–oxide–semiconductor field-effect transistor
Si-NEMS	Silicon nano-electro-mechanical system
SiNW	Silicon nano-wire
SiO$_2$	Silicon dioxide
SNR	Signal-to-noise ratio
SOI	Silicon-on-insulator
TMN	Thermomechanical noise
VCO	Voltage-controlled oscillator
VHF	Very high frequency
VLSI	Very large-scale integration
XeF$_2$	Xenon difluoride

List of Symbols

$\bar{H}_{exp}^i$ i-th point of experimental data in RRMSE evaluation

$\bar{H}_{model}^i$ i-th point of modal data in RRMSE evaluation

$A_n(\omega), B_n(\omega)$ Orthogonal displacement in in-phase and out-of-phase

A_0, B_0 Initial in-phase and out-of-phase displacement

C_c Critical damping factor

C_g Gate-beam capacitance

D_j distance to the j-th object of DFT MEMS neurons

F_{elec} Electrostatic force

G_{ac} Lock-in gain of AC signal amplifier

$I_{Lock-in}^{FM}$ Lock-in detected FM current output

I_{bg} Background current of mixing measurement

I_0 Input current valule

J_e Current density (electron)

M_{eff} Effective mass of beam

S_{iz} Scaling factor for FM measurement signal conversion

$S_{v,sys}$ System spectrum density

$S_{v,th}^{1/2}(\omega)$ Voltage spectrum density of thermomechanical noise

S_x Displacement spectrum density

V_{ω_L} Reference signal amplitude of mixing measurement

V_{AC}, V_{ac}	Voltage of alternating current
V_{DC}, V_g^{DC}, V_{dc}	Voltage of direct current
V_{MEMS}	DFT MEMS neuron's actuation voltage
V_{PSD}	Lock-in phase shift detector output voltage
$V_{b,i}$	DC bias for DFT MEMS neurons
V_i	Lock-in input signal amplitude
V_{ref}, V_L	Lock-in external reference signal amplitude
V_{sensor}	DFT MEMS neuron's output voltage
V_0, V_{in}	Coupled MEMS DFT Neuron's threshold voltage and input voltage
$dR(\lambda_j)/d\lambda_j$	Differential of reflected power with respect to the wavelength change
d_0	Initial deflection
$f_{max}(B)$	Frequency at maximum amplitude for magnetic driven NEMS
f_{res}, f_0	Resonance frequency
$f_0 \times Q$	Bandwidth of resonance
g_0	Initial gap between beam and gate
k_B	Boltzmann's constant
k_e	Equivalent electrical linear stiffness
k_l	Linear stiffness
k_{nl}	Nonlinear stiffness
$k_0, k_1 \dots k_n$	Stiffness coefficient in n-th order perturbation series
m_b	Mass of beam (effective)
n_e	Electron concentration

t_B	Thickness
$w_{sensor,j}$	Weight applied to the input voltage from j-th sensor
z_h	High order terms of displacement
$\mathcal{R}^2$	Square of responsivity
$\Lambda_0(B)$	Zero order displacement for magnetic driven NEMS
β_e	Equivalent electrical nonlinear stiffness
β_m	Mechanical nonlinear stiffness
δ_{ij}	Kronecker delta function in DFT MEMS
μ_e	Electron mobility
ξ_{0p}	Peak value of vibrational amplitude
ω_c, ω_Δ	High-frequency carrier component, frequency deviation in FM
ω_l	Angular resonance frequency with respect to linear stiffness
ω_0, ω_{0r}	Angular frequency of resonance
ϕ_L	Lock-in reference signal phase
$\phi_0(x)$	Deflection profile
A, S	Area of parallel capacitive plates ($L \times W$)
$B(t)$	Magnetic field strength
C	Damping factor
E	Young's modulus
$E(t)$	Electrical field intensity
G	Conductance
$G(A, B, \omega)$	Galerkin function of residuals
J	The Jacobian matrix of Galerkin function
K	Overall amount of stiffness

L, l, I_B, I_C	Length
P	Power level, in dBm
Q	Quality factor
$R(t)$	Time-dependent residual force
$R(t)z(t)$	Residual energy
$Re[\delta z(\omega)]$	The real-part of the displacement derivatives
T	Temperature in K
V	Voltage
W, w_B	Width
$at.cm^{-3}$	Atom per volume in cm^3, concentration of dopant
e	Single electron charge
f	Frequency
$f(z,t)$	Duffing oscillator driven force
h	Bandwidth
j	Cavity mode index
k	Stiffness
nm	Nano-meter
t	Time
$w(x,t)$	Deflection
$z(t)$	Displacement
$\Delta\lambda_j$	Change of wavelength
ΔH	Thermomechanical noise displacement
ΔR	Reflected power
$\alpha(B)$	Total amount of nonlinearities for magnetic driven NEMS

$\beta, \beta_{overall}$	The total amount of nonlinearity
$\delta G/\delta V_{DC}$	Mixing measurement transconductance
$\delta f(B)$	Shift of resonance frequency for magnetic driven NEMS
$\varepsilon, \varepsilon_0$	Permittivity, permittivity in vacuum
$\theta, \Delta\theta$	Phase, shift of phase
μ	Damping coefficient for magnetic driven NEMS
μm	Micro-meter
ξ	Damping ratio
π	Pi, ratio of circle's circumference to its diameter
ρ	Density
$\sigma(t)$	Charge density
ω	Angular frequency

List of Publications

Journal Papers

(1) Fang Ben, James Fernando, Jun-Yu Ou, Cécilia Dupré, Eric Ollier, Faezeh Arab Hassani, Hiroshi Mizuta and Yoshishige Tsuchiya. 'Characterisation and modelling of nonlinear resonance behaviour on very-high-frequency silicon nanoelectromechanical resonators' *Micro and Nano Engineering*, 2023: 100212.

(2) Fang Ben, James Fernando, Jun-Yu Ou, Yoshishige Tsuchiya. 'Model Development for the Analysis of Nonlinear Silicon NEMS Resonator Characterisation' In preparation, to be submitted to *Nanotechnology*

(3) James Fernando, Fang Ben, Jun-Yu Ou, Yoshishige Tsuchiya. 'Thermo-mechanical Noise Characterisation and Tunning Effect for Silicon NEMS Resonators' In preparation, to be submitted to *Micro and Nano Engineering*.

International Conference Papers

(4) Fang Ben, James Fernando, Jun-Yu Ou, and Yoshishige Tsuchiya. 'Development of Systematic Fitting Model for Nonlinear Nanoelectromechanical Resonance Analysis'. *IEEE MEMS, Gainesville, United States (Online). 25-29 Jan. 2021*. pp 611-614.

(5) Fang Ben, James Fernando, Jun-Yu Ou, and Yoshishige Tsuchiya. 'Analysis of hysteresis behaviour in nonlinear resonance of silicon nanoelectromechanical resonators'. *47th International Conference of Micro and Nano Engineering, Turin, Italy (Online) 20-23 Sept. 2021*

(6) Fang Ben, James Fernando, Jun-Yu Ou, and Yoshishige Tsuchiya. 'Modelling of Nonlinear Resonance Behaviour in 1-ω Mixing Measurement for 125-MHz Silicon Nanoelectromechanical Resonator'. *48th International Conference of Micro and Nano Engineering, Leuven Belgium* 19-23 Sept. 2022 (Oral)

(7) James Fernando, Fang Ben, Jun-Yu Ou, and Yoshishige Tsuchiya. 'Spectral Characterization and Tuning Effect of Picometre-scale Thermomechanical Motion for Silicon NEMS Resonators'. *47th International Conference of Micro and Nano Engineering, Turin, Italy 20-23 Sept. 2021* (Oral)

Internal Conference

(8) Fang Ben, James Fernando, Yoshishige Tsuchiya. 'Silicon Nano-electro-mechanical Resonator Voltage Tunning Characterisation with FM' SEMS Group Seminar Individual Talk. 2019

(9) Fang Ben, James Fernando, Jun-Yu Ou, Yoshishige Tsuchiya. 'Nonlinear Dynamics of Silicon NEMS Resonator and its applications' SEMS Group Seminar, April 2022

(10) Fang Ben, James Fernando, Jun-Yu Ou, Yoshishige Tsuchiya. '1-ω mixing measurement and novel nonlinear model for silicon NEMS resonator'. Three Minutes Thesis. July 2022.

In this thesis, the relationship between each chapter and the aforementioned publications is as follow:

- Chapter 3 encompasses the theory content from publication (1, 2, 4, 5, 6)
- Chapter 4 encompasses the experiment and result from publication (2, 4, 5)
- Chapter 5 encompasses the experiment and result from publication (1, 6)
- Chapter 6 encompasses the theory and result content from publication (3, 7)

To my families for their unwavering support and love

CHAPTER 1

Introduction

1.1. MEMS and NEMS

Continual progress in the miniaturization of semiconductors and cost reduction are persistent demands in the field of integrated circuits (IC) research. Despite the significant achievement made, challenges such as off-state current leakage due to short channel effect [1] drain-induced barrier lowering (DIBL) [2], gate-induced drain leakage (GIDL) [3] or self-heating effect [4], are inevitable. Figure 1.1 shows the roadmap for semiconductor smart devices and presents main topics in micro- and nanoelectronics domain including 'More Moore' and 'More than Moore'. In 'More than Moore' technologies, diversification in non-digital devices including hybridization with various platform offers diverse functionalities and also contributes miniaturization of electronic systems [5]. Wearable and portable devices which can enhance the human and environment interactions associated with intelligent sensors are further benefits of the 'More than Moore' platform. Micro-electro-mechanical systems (MEMS) provide a horizontal integration along with conventional IC platforms. This co-integration leads to the development of ultra-high-sensitivity and highly-integrated sensors that can detect, control, and interact with the physical world, paving the way towards advanced intelligent system.
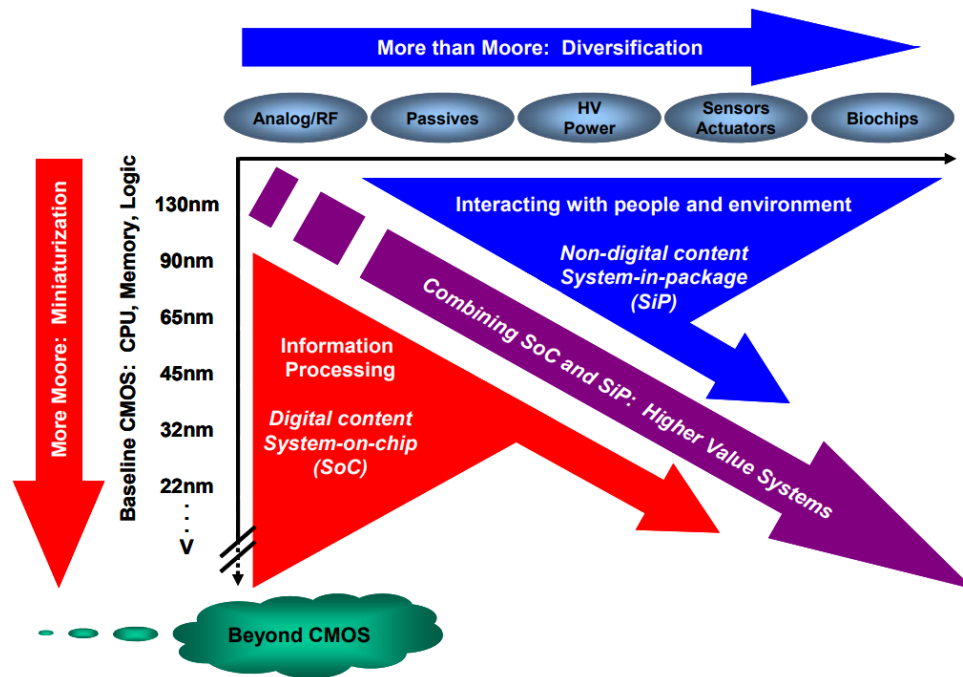
Figure 1.1 The International Technology Roadmap for semiconductors recognizes a growing demand for both digital and non-digital features within a unified system, which is reflected in two key trends: the shrinking of digital functions through miniaturization, known as "More Moore," and the expansion of diverse functions beyond digital, known as "More-than-Moore." [5, 6].

The rapid development of MEMS since 1970s has successfully boosted many fields including aeronautics, automobiles, and consumer applications. From 1990s, MEMS has been widely used as horizontal architectures as a part of mini circuit. For instance, (i) micro-accelerometers have been widely integrated on a large scale into cars, consoles, and mobile phones [7], (ii) MEMS switches are an ideal choice because of its extremely low OFF-state current thanks to switching in mechanical structure, while it also allows higher current in ON-state than conventional transistor [8], and (iii)MEMS memory, reported by [9], behaves as a suspended gate (SG) MOSFET that utilizes the charging of the gate dielectric by direct mechanical contact of the gate to achieve bi-stability and hysteresis in the current-voltage (I-V) characteristics, allowing controllable state operation without significant degradation for up to 10^5 cycles. These achievements are considered as substantial solutions for the challenges in era of 'More than Moore' and 'Beyond CMOS (complementary metal-oxide

semiconductor)'.
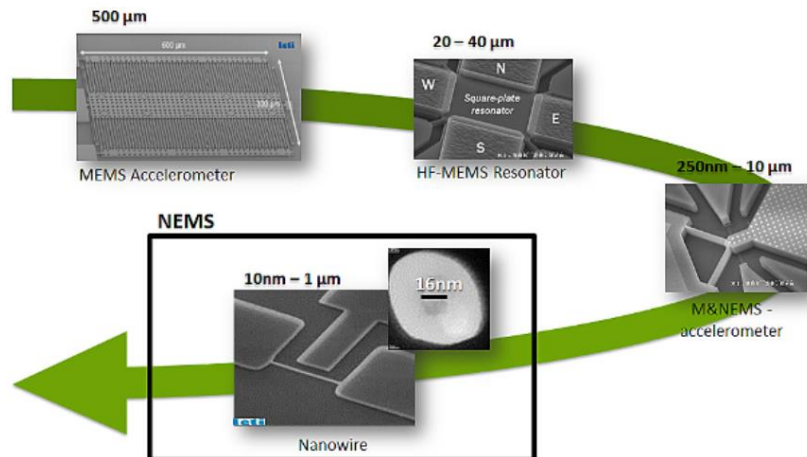
Figure 1.2 Typical sizes from MEMS to NEMS [10].
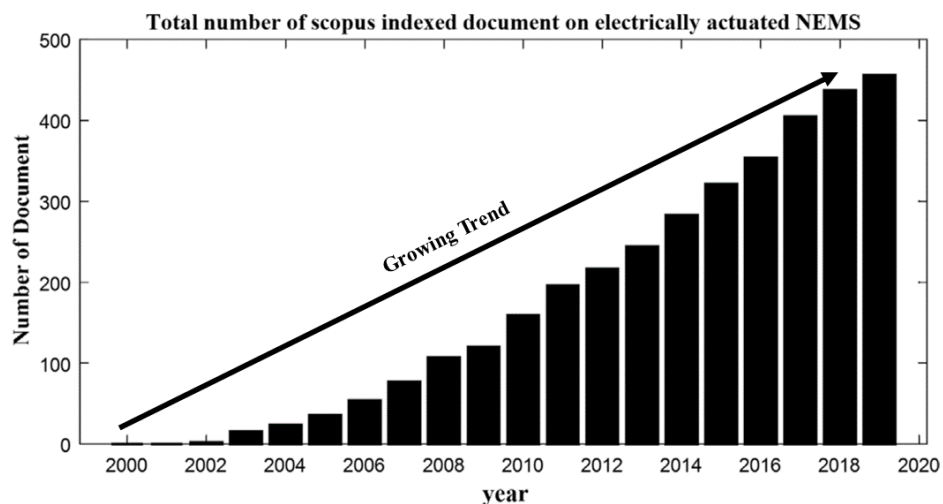
Figure 1.3 Total number of indexed documents recorded in Scopus dataset from 2000 to 2020 [10].

The development of technology to scale down silicon devices pave the way to continuously shrink the size of MEMS device. Therefore, when the critical dimension of lithography approached to the nanoscale in early 2000s, an idea of Nano-Electro-Mechanical system (NEMS) emerged. Figure 1.2 shows an example of the typical sizes and designs from MEMS to NEMS. The benefits of building electro-mechanical

structure in nanoscale include low power consumption, high sensitivity, and low current leakage. Among studies of various NEMS devices, NEMS resonators are one of the significant parts associated with their high-frequency operation and potential applications for high-sensitivity sensors due to their ultrasmall scale. Figure 1.3 shows the growing trend of NEMS research since 2000s. Many have reported that NEMS possess great potential for applications in atomic-level mass sensing [11, 12], nano-radio detection [13], and fundamental physics investigation [14]. These applications demonstrate the versatility of NEMS resonators in various fields.

While the NEMS resonators are getting great attention, one cannot ignore their nonlinear behaviour. The nonlinear response of MEMS/NEMS resonators was firstly reported by Andres et al. [15] in 1987. In recent years, there has been a growing interest in the nonlinear behaviour of NEMS resonators due to their small mass and size, which allow the nonlinear resonance regime to be easily reached [16]. While nonlinear behaviour is generally considered undesirable in common MEMS/NEMS devices operating in the linear regime, there have been cases where nonlinear characteristics are actively utilized to improve device performance or achieve desired functionality. Sansa et al. [17-21] demonstrated a concept of a nonlinear detection scheme to amplify the resonance response and to enhance the dynamic range for sensing applications. This approach allows for more sensitive detection of signals, which can be particularly useful in applications where signals are weak. Another example of utilizing nonlinear behaviour is the implementation of a neural network using coupled MEMS oscillator arrays. In this case, the nonlinear behaviour of MEMS resonators with hysteresis characteristics can play a pivotal role in demonstrating fading memory functionality [22]. An alternative approach for neuromorphic computing hardware based on nonlinear MEMS oscillators has also been proposed in [23] and [24]. In general, the use of nonlinear behaviour in MEMS/NEMS resonators has become an increasingly popular topic of research, particularly in the development of advanced sensing and computing systems.

1.2. Motivation and Scope of Thesis

1.2.1. Reasons for the Nonlinear Analysis

In nature, linearity is merely a conceptual framework in mathematics, representing an idealization. In truth, no physical system adheres precisely to the principles of linearization. Nevertheless, numerous natural phenomena and engineering systems exhibit behaviour closely resembling linearity, allowing for the development of mathematical models based on this assumption. Examples in mechanics include the constitutive laws for elastic materials like metals, structures experiencing minimal deformations, and linear viscous damping. For centuries, engineering has predominantly employed a linear methodology for design, modelling, and analysis, which has maintained simplicity. Due to this, nonlinear behaviour is often considered undesirable, therefore, its exploitation in certain contexts has the potential to improve device performance and enable new functionality. The continued exploration of nonlinear behaviour in MEMS/NEMS resonators is likely to lead to further advances in a variety of applications. This trend strongly suggests importance of detailed analysis of nonlinear dynamic behaviour of MEMS/NEMS resonators. In particular, towards highly-integrated MEMS/NEMS resonator arrays for neuromorphic computing or active system-level integration of MEMS/NEMS sensor arrays for Internet-of-Things (IoT) applications, it is very important to develop analytical or mathematical models to describe the operation of MEN/NEM resonators including their nonlinear behaviour with a certain level of accuracy. This research project began with the follow-up study based on the research by F.A Hassani and Y. Tsuchiya [25-27]. A doubly-clamped silicon NEMS resonator was fabricated as a part of European FP7 NEMSIC project [25, 26] where DC and power dependence characterized in linear regime was later reported by Y. Tsuchiya et al in 2018 [27]. Among the past study on NEMS, nonlinear behaviour was observed but an in-depth understanding on its characteristics was missing. In the meantime, the numbers of reports related to nonlinear MEMS/NEMS potential applications further inspired this project to be motivated and work towards the nonlinear characterisation. A systematic model that

can be implemented to the analysis with respect to experimental data is an ideal method to not only reveal the origins of nonlinearity within the device but also to give thorough understanding and controllability of such a feature at system level. Hence, the analysis and modelling of nonlinearity in NEMS resonators are critical steps for the development of high-performance sensing and computing devices in future.

1.2.2. Scope of Thesis

This thesis has focused on the study of nonlinearity of the NEM resonators. The nonlinearity of NEMS stems from various origins. Mechanical nonlinearities consist of two sources, which are geometric nonlinearity and intrinsic material features. Tiwari et al., [28] summarized the details regarding how geometric nonlinearity affects the mechanical behaviour for MEMS/NEMS when it performs distinct effect with asymmetric device design. In our case, because of the symmetric design Hence, in this thesis, regarding the mechanical nonlinearity, theory and model focused on the study for intrinsic material effect.

Another significant characteristic is how external excitation can not only tune the frequency resonance but also enlarge the nonlinearity. As a continuing study based on Y. Tsuchiya reports [27] in 2018, this thesis provides with an explicit mathematic explanation on how voltage is changing the overall stiffness in both linear and nonlinear regime with an integrate model that fitted with data from multiple experimental technique such as frequency modulation (FM), 1- ω mixing measurement, and thermomechanical noise by spectrum analyser.

As a summary, this thesis proposes a novel method to study the nonlinear characterization on doubly-clamped Si-NEMS resonator. Scaling effect is covered where the lengths of Si-NEMS resonator are 2, 1.5, and 1 μm, the widths of Si-NEMS are 135, 105, and 75 nm. The nonlinear characteristic is explained from the origin of intrinsic mechanical nonlinearity β_m and the electrostatic force nonlinearity β_e where the frequency resonance voltage-tuning effect is also explained via a new linear

6

electrical stiffness k_e. Each of the terms possess physical meaning and will be described further in chapter 2.

1.3. Novelty Statement

The scope of the thesis has covered the objective of the project. Novel contributions during the project are listed as follow:

1) <u>Resonance voltage tuning effect for Si-NEMS resonator</u>. This project proposes explanation for how external voltage (DC, RF) alters the overall linear stiffness. For a very high-frequency (VHF) system operating at the nano-scale, the effect of the non-zero order terms in the Maclaurin series cannot be neglected, and its first-order term is therefore extracted for the linear stiffness study. This work is implemented with experimental data and has successfully explained the resonance voltage tuning effect with frequencies up to 220 MHz

2) <u>Nonlinearity voltage tuning effect for Si-NEMS resonator</u>. This thesis gives an explicit theory to explain the nonlinearity voltage tuning effect for the silicon-based NEMS resonator. The model for the voltage-dependent nonlinearity is proposed where the simulation of model fits well with the experimental data.

3) <u>Intrinsic mechanical nonlinearity</u>. This thesis proposes a new way to define the intrinsic amount of nonlinearity and proves it as a constant. The novel part of this point is that in past research, the amount of the intrinsic mechanical nonlinearity with a separated discussion besides the voltage-dependent nonlinearity is lack of study. It is, for the first time, that a model is successfully fitted with both DC and RF power dependence with only one constant nonlinearity, which successfully defines the 'intrinsic' property, leading to a potential way to quantify and control the nonlinearity in nanoscale and VHF.

4) <u>Hysteresis behaviour study</u>. In experiment, an optimization for recording the data is completed to achieve a 'forward' and 'backward' frequency sweep,

allowing an effective way to study the hysteresis behaviour of the Si-NEMS resonator frequency response. In model, the hysteresis behaviour is explained based on bifurcation theory for a cubic nonlinear system. Numerical approach is introduced to obtain multiple steady-state solutions under each of input frequency so that the simulation can be used to fit hysteresis response.

5) Frequency Modulation (FM) Displacement to current conversion. To fit the experimental current signal data, a study regarding how to convert simulated displacement signal into current signal is completed. For FM method, traditional way is to introduce a 'scaling factor', which remains unknown in physical meaning. This thesis explained how 'scaling factor' is changed with respect to the DC and RF power and a detailed mathematic derivation is given. It is essential in nonlinear analysis as current signal detected by FM measurement was only applicable within linear regime in past research [29]. Once an explicit expression of conversion factor is given, it can be imported into the nonlinear model and give nonlinear response in current form and fulfil the fitting with FM measurement in nonlinear regime.

1.4. Organization of the Thesis

Chapter 2 provides with the literature review regarding the MEMS/NEMS nonlinearity characterization study in past few decades. Starting from the ground-breaking observation on MEMS nonlinear behaviour completed in 1980s, this chapter summarizes the progress of the nonlinearity investigation based on its source, material, designs and measurements. After that, this chapter also covers the most up-to-date research on potential applications that utilizes nonlinear MEMS/NEMS as sensing enhancement, reservoir computing virtual node, and neuromorphic computing method with coupled oscillators. Chapter 3 shows the details of the nonlinear modelling theory for the Si-NEMS resonator. The derivation of parameters including dimensions (length, width, gap), voltages, RF signals, resonance characterization parameters are described individually. This chapter also explains the physical meaning of these

Chapter 1: Introduction

parameters within the model and how those parameters affect the experimental result, leading to an insightful understanding towards the modelling fitting. In addition, this chapter includes details of the displacement calculations by solving the model with Petrov-Galerkin Method (PGM) and Newton Raphson iteration. Calculation is completed by MATLAB, codes, fitting process, and parameters extraction, which are illustrated in this chapter. Chapter 4 is the results and discussion designated for frequency modulation (FM) measurements. First, this chapter described the scheme of the experimental setup of FM with a brief explanation of current modulation techniques in this scheme. Later, the displacement to current conversion factor and its derivation are described. The corresponding section explains the mathematical relationship between FM conversion factor with respect to the external DC voltage and RF power signal. Then, DC dependence, RF power dependence, and hysteresis behaviour tested under FM are shown with respect to different sample sizes. All the results are followed by model fitting and key parameters extracted from the fitting are discussed in this chapter. Chapter 5 is the results and discussion designated for 1-ω mixing measurements. This chapter begins with the description of the 1-ω mixing setup where the signal detection mechanism is explained in detail. To have a closer link between the model and experiment, this part also covers the basis of the conversion between the current and displacement under the mixing measurement scheme. Then, a similar study method is applied for the mixing scheme where the DC dependence, RF dependence, and hysteresis behaviour are studied and followed by comprehensive model fitting, and then extracted parameters and overall nonlinear characteristics are discussed. Chapter 6 is an introduction of the investigation regarding the thermo-mechanical noise of the Si-NEMS resonator. Chapter 7 summarises the work during the four-year research. Insightful comments and future plans regarding the project are given in the later section of this chapter.

CHAPTER 2

Nonlinear MEMS/NEMS: Review

MEMS and NEMS are scalable devices that co-integrate mechanical structure with electronics (e.g., piezoresistive pressure sensor). However, the nonlinearity, which arises due to the nonlinear response of materials, geometries, and motions at the micro/nano scale, can impact the performance and it emerges rapidly when critical dimension of structure is miniaturized into nano-scale. The nonlinear phenomena generally present as the deviation from the linear response of a system to an external stimulus. The investigation and thorough understanding of nonlinear behaviour in MEMS/NEMS is essential to exploit their dynamic response. In past several decades, studies of nonlinear phenomena in micro- and nano-systems have been a growing research field. From the perspective of using nonlinearity, many studies have proposed the use of various interesting phenomena stemming from nonlinearity such as bifurcation, chaos, and hysteresis which are the fundamentals for many applications. However, nonlinearity can be also harmful and cause undesirable effects such as reducing the sensitivity, increasing the noise level, limiting the operational range. For this reason, understanding of the nonlinear behaviour of MEMS/NEMS is crucial for designing and optimizing these devices. This chapter will focus on reviewing the nonlinearity studies specifically in the field of MEMS/NEMS, including an introduction of the source of nonlinearity, typical behaviour of the nonlinearity, history of relevant nonlinearity studies in MEMS/NEMS, and discussion

about potential nonlinear MEMS/NEMS applications.

2.1. The Origin of Nonlinearity in M/NEMS

Nonlinearities in micro- and nanoscale systems can come from a large variety of origins. Hence, an in-depth understanding is essential for accurate modelling, performance optimization, robustness analysis, and design improvement. For Si NEMS resonators, various sources of nonlinearities can be exhibited leading to impacts towards their behaviour and performance. A summary of previously reported common sources of nonlinearities in such resonators are [28, 30, 31]:

1) Geometric nonlinearities: These nonlinearities arise due to large deformations in the resonator structure. For example, when the amplitude of oscillation is large, the resonator may undergo significant deformation, causing change of the stiffness of the resonator lead to nonlinear response. This can affect the resonance frequency, amplitude, and quality factor of the resonator.

2) Material nonlinearities: Silicon doubly-clamped NEMS resonators are made of silicon, which has its own nonlinear material properties. Nonlinearities in material properties such as Young's modulus, thermal expansion coefficient, and damping coefficient can lead to nonlinear behaviour of the resonator.

3) Contact-induced nonlinearities: In some cases, the resonator may come into contact with its supporting structure, resulting in nonlinear anchor loss that can affect the resonance frequency and damping of the resonator.

4) Electrostatic nonlinearities: NEMS resonators are often actuated and sensed using electrostatic forces. These forces can exhibit nonlinear behaviour due to nonlinear capacitance-voltage relationships or due to nonlinearities in the position-dependent electrostatic forces.

5) Environmental nonlinearities: The behaviour of the resonator can also be affected by the environment it is operating in, such as changes in temperature, pressure, or gas composition. Nonlinearities in the environmental response can

11

affect the resonance frequency and damping of the resonator.

6) <u>Nonlinearities due to fabrication imperfections</u>: Fabrication imperfections such as residual stresses, surface roughness, and variations in the material properties can also lead to nonlinearities in the behaviour of the resonator.

In general, nonlinearities due to contact and fabrication imperfections are a result of external reasons that lead to abnormal frequency response. Considerations for these origins will need detailed observations of nanoscale sample structures for identification. In terms of environmental nonlinearities, controls of temperature, pressures and surroundings are significant. These experiments are taken via electrical prober station in a vacuum chamber, where conditions are kept at room temperature in vacuum throughout all the test measurements. This review will be more focused on the origin of other nonlinearities.

2.1.1. Mechanical Nonlinearities

The geometric nonlinearity and material nonlinearity are both intrinsic and they are usually categorized as mechanical nonlinearity. For a flexural device, the mechanical nonlinearity can be no longer ignored when there is a large displacement where the dynamic changes in spring constants is a function of displacement [28]. The nonlinear coefficient can be modelled by classical Euler-Bernoulli beam theory or Duffing oscillator theory, but the assumption depends on the actual design of the device. Especially, the domination of geometric nonlinearity arises when the design of device is asymmetric.

Sansa et al., [19, 20] proposed a novel asymmetric design of silicon nanowire (SiNW) to enhance the piezoresistive (PZR) transduction. The asymmetric beam shape at rest successfully enables highly sensitive linear detection of vibration of low-resistive silicon beams. According to their study, as shown in Figure 2.1(a), the maximum deflection at rest d_0 contributes as the control of linear transduction threshold. In Figure 2.1(b), they presented a study of the mechanism of transduction where the

linear transduction dominates when the deformation during vibration a_n is less than $4d_0$. Their later experimental result further proves that the initial strain caused by the asymmetric beam deflection at rest can lead to the onset of nonlinearities. S. Tiwari et al., and C. Mendez et al., have also reported their findings regarding the geometric nonlinearity stemming from the asymmetric design or actuation [28, 32].
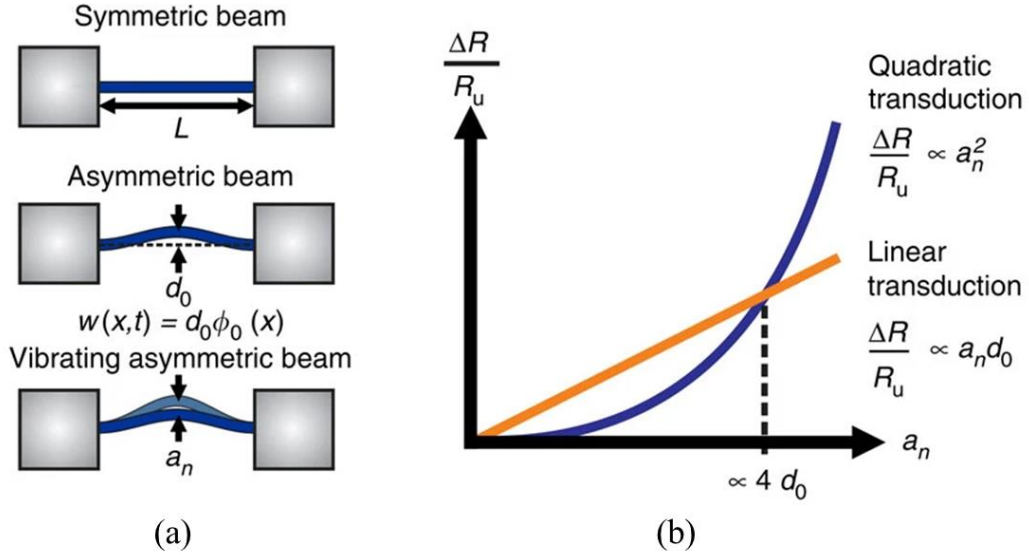
Figure 2.1 Asymmetric design of a piezoresistive (PZR) silicon nanowire (SiNW) by Sansa et al., in 2014. (a) A scheme shows the beam in symmetric structure and asymmetric structure with initial deflection at d_0. The total deflection $w(x, t)$ is given by the sum of deflection profile $\phi_0(x)$ and d_0. a_n is the amplitude of vibration. (b) Study of the transduction mechanism in different amplitude of vibration [19].

Euler-Bernoulli vs Duffing: Two common models to describes the mechanism of oscillator motions are Euler-Bernoulli equation and Duffing equation, which are used under different scenarios. When dealing with the geometric nonlinearity in structural analysis, the Euler-Bernoulli equation is more widely used. In detail, Euler-Bernoulli beam theory (EBT) is a partial differential equation (PDE) that tells the deformation of a loaded beam, which considers the axial, bending, and the shear deformations. The basis of EBT is derived from the assumption that the strains are small, and the curvature is constant, which intrinsically makes it ideal for linear analysis. In case, where the deformation is large and nonlinear, modification based on EBT is required

to analyse the geometric nonlinear. Herisanu et al., [33] built two Euler-Bernuolli carbon nanotube (CNT) beams embedded on nonlinear foundations. To investigate axial nonlinearity, they proposed a model based on EBT and used Galerkin-Bubnov method to govern the PDE [34]. They successfully obtained analytical solutions that can be applied to study the geometric nonlinearity under forced vibration through optimal auxiliary function method (OAFM) without considering simplifying hypothesis. Matheny et al., from Roukes group, which is one of the pioneers in MEMS/NEMS field, proposed their attempts in applying EBT into the nonlinear mode-coupled nanomechanical system [35]. They reported a novel model based on EBT in the presences of nonlinear axial stress to predict the intra- and intermodal nonlinearity for a doubly-clamped NEMS beam. Their achievement, to the best of my knowledge, was the first confirmation of the quantitative predictions of EBT for tension-induced geometric nonlinearities and paved the way to further nonlinearity studies that involves coupled-mode micro- and nano-structure. In addition to geometric nonlinearity, material nonlinearity is more frequently considered as it is an intrinsic property especially for silicon-based devices. In this case, when it comes to mass-spring system, Duffing equation is used with a cubic nonlinear spring [36]. Zhu et al. [37] conducted a study to assess how material nonlinearity affects the dynamic response of MEMS. They discovered that there is significant material nonlinearity in single crystal silicon. To determine this, they utilized *ab initio* simulations to extract the shear properties of single crystal silicon and used them to determine the nonlinear response. They integrated the calculated shear stress-strain response of bulk silicon into their model, which aligned with experimental outcomes. The researchers found that, for a high-Q resonator, even slight nonlinearities due to material can have a significant impact on the performance.

2.1.2. Electrostatic Nonlinearities

Electrostatic force is another one of the major origins of nonlinearities when MEMS/NEMS devices are primarily driven by voltage. Modelling the MEMS/NEMS

as the parallel plates, the electrostatic force is given as,

$$\varepsilon A V^2 / 2d^2 \tag{2.1}$$

where ε, A, V, d are the permittivity, area of plates, voltage, and gap between plates, respectively. The force is quadratically proportional to the voltage, which makes the system nonlinear intrinsically. On the other hand, the increase of displacement leads to large deformation. The change of the gap d due to the displacement can no longer be ignored. The modified electrostatic force is presented as,

$$\frac{\epsilon A V^2}{2(d-z)^2} \tag{2.2}$$

where z is the motional displacement. This change nonlinearly affects the instantaneous electrostatic force and makes the forces depend on the displacement nonlinearly.
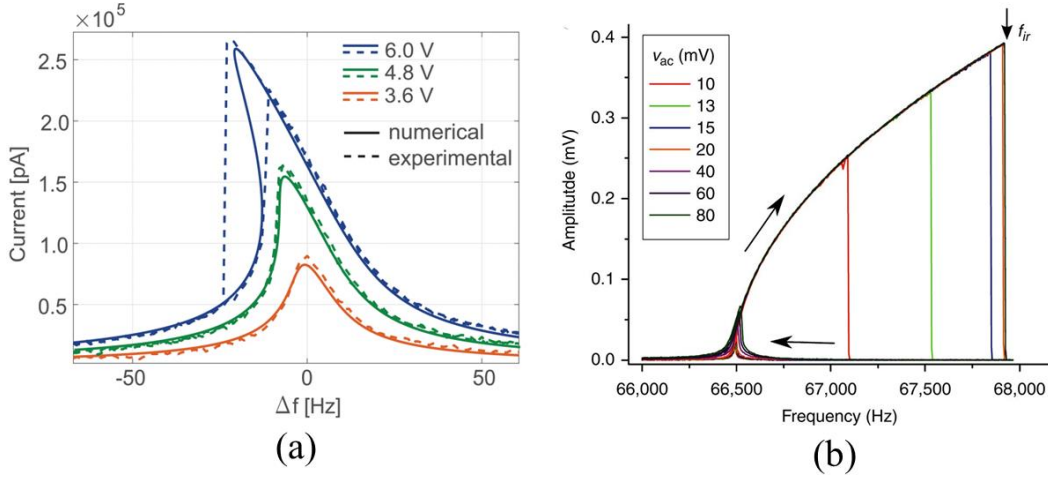
Figure 2.2 Studies regarding electrostatic nonlinearity. (a) Zega et al., reported the DC bias nonlinearity for the frequency response of the Two Double-Ended Tuning Fork (DETF). (b) Antonio et al., reported the AC signal nonlinearity under a fixed DC bias [30, 38].

The total electrostatic force is contributed by the interaction between DC bias via the actuator and AC or RF signal going through the beam. Hence, the nonlinearities work in the same way, leading to the nonlinear behaviour in the DC or AC dependence.

Figure 2.2 shows the recent studies of nonlinear electrostatic force dependence on DC (Figure 2.2 (a)) and AC (Figure 2.2 (b)) signals, respectively [30, 38]. The asymmetric resonant curve is a typical sign of the existence of nonlinearity. In relevant researches [28, 37, 39-44], asymmetry resonance curves that shift to left and right are also named as nonlinear 'softening' and 'hardening'. In summary, the electrostatic force induced nonlinearity is directly related to the external input. Studies to reveal its mechanism have been widely reported [28, 37, 39-44], but to make a close link between fundamental mechanism and experiments, a systematic method for analysis is required. The next subsection covers the trend of nonlinear research in the MEMS/NEMS field and gives study cases to introduce the history of this topic and its impact.

2.2. Past Studies in Nonlinear MEMS/NEMS

Thorough understanding of the origin of nonlinearity requires applicable theoretical or numerical methods, devices, and experimental tools. This section will review the past studies regarding the nonlinear behaviour in MEMS/NEMS field. In early stage, one of the representative nonlinearity studies was reported in 1987 by M. V. Andres et al. [15]

(a)   (b)
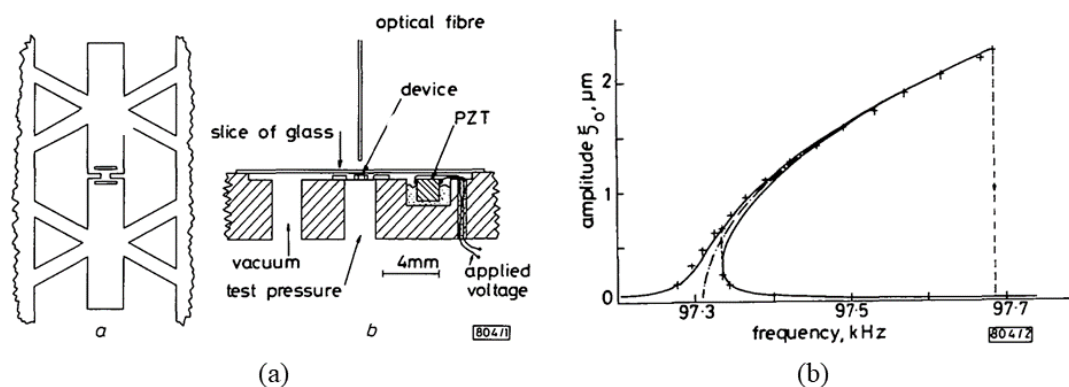
Figure 2.3 Study by Andres et al., in 1987 about nonlinear vibration observation. (a) Diagram of the resonator and its holder. (b) Resonance curve with strong nonlinear behaviour with frequency at 97.3 kHz [15].

16

They proposed their observation of a nonlinear response and hysteresis of micromachined silicon resonators [15]. Clear nonlinear behaviour occurs when large amplitudes of vibration are excited. Figure 2.3(a) schematically presents the geometry of a micromachined silicon resonator. With the coupled pair of suspended rectangular plates due to its higher Q-factor, this design enabled more precise measurement of its properties. In analysis, by the given width of the curves, the Q-factor of each resonance can be determined. When the voltage applied to the piezoelectric transducer is increased, causing the amplitude of vibration to rise, the response curve becomes somewhat unbalanced, indicating the onset of nonlinearity. For instance, Figure 2.3(b) shows the strong nonlinearity [15] given around at the resonance frequency of 97 kHz. According to the theory Dinca et al., [45] proposed in 1973, the reason behind the hysteresis behaviour can be attributed to the slightly anharmonic response of the vibrators. When the restoring force of the system deviates from being purely linear, and instead shows a minor nonlinear dependence on the displacement such as a small cubic contribution, then the resonance frequency will exhibit a minor quadratic dependence on the amplitude of vibration. The analysis for Figure 2.3(b) gives the quality factor Q at 21000 where the amount of total nonlinearity is 1.94×10^{-3} μm^{-2}, which is the first quantitative estimation of the nonlinearity from MEMS devices. The quantification of nonlinearity in MEMS devices assumes paramount importance due to its pivotal role in facilitating a comprehension of their intricate dynamic responses that only relate to its dimensional properties. This critical assessment informs the refinement of design parameters and optimisation strategies. The acquired insights find applicability in refining predictive models for enhanced accuracy and optimising control methodologies. These advancements hold the potential to propel the utilisation of MEMS-based technologies across domains encompassing precision sensing, actuation, and signal processing. To explain the onset of hysteresis, they have proposed a novel theory that if the amplitude is boosted enough, the response curve will exhibit even stronger nonlinearity. And when the shift exceeds the certain limits by the bandwidth, the system will show hysteresis. The following equation explains the relationship between the bandwidth h, resonance frequency ω_{0r}, minimum value of peak amplitude required to develop hysteresis ξ_{0p}, and nonlinearity amount β [15];

$$\xi_{0p}^2 > \frac{8h}{3\omega_{0r}|\beta|} \tag{2.3}$$

Equation (2.3) is the very first model that explicitly explained the threshold or onset point of the hysteresis behaviour. To apply the equation, the parameters h and β can be determined first via model fitting. The damping coefficient can be calculated from measurements or by giving a Q value, $Q = \omega_{0r}/2h$ when a small amplitude of the force is applied. h is established by observing the system's response under conditions of small amplitude excitation, prior to the point at which the resonance exhibits a subtle degree of asymmetry. In other words, the parameter Q is characteri2ed within the linear region, aiming to prevent ambiguous determination of the bandwidth in the presence of a significantly nonlinear resonance [15].

As Equation (2.3) shows, the onset of strong nonlinearity is directly relevant to the resonance frequency ω_{0r} which is further linked with the design and dimensions of the device itself. Based on Hooke's Law, the system frequency is expressed as $\omega = \sqrt{k/m_b}$ where k is stiffness and m_b is effective mass [46]. When the dimensions are reduced down into nanoscale, due to the increase of stiffness and reduction of the effective mass, the resonance frequency is largely increased in both ways in general.
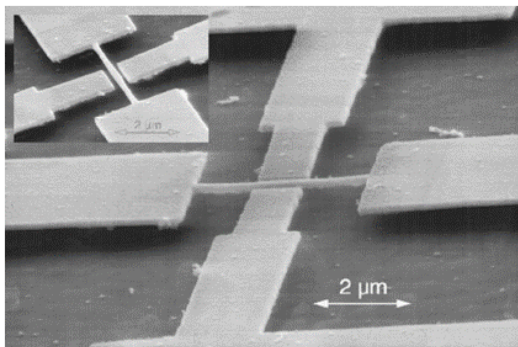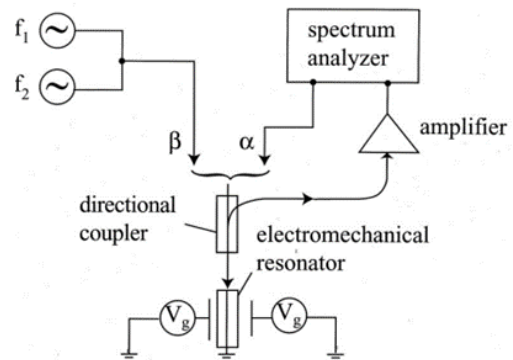
(a)   (b)

Figure 2.4 Study by Erbe et al., in 2000 about nonlinear vibration observation based on NEMS resonator. (a) Scanning electron-beam micrograph of the NEMS resonator. (b) Experimental setup for sampling the mechanical properties of the suspended beam [47].
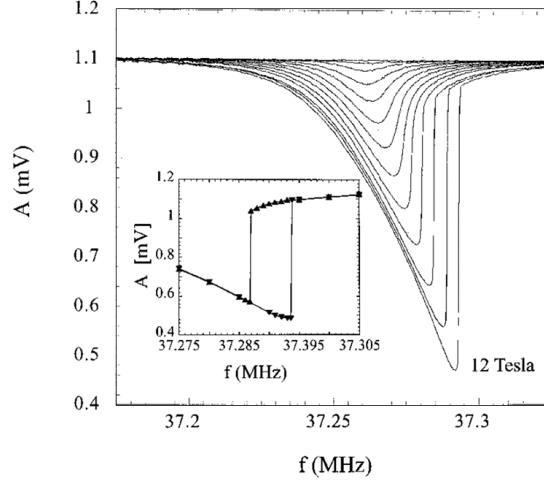
Figure 2.5 Characterisation of the nonlinear response of the suspended beam by ramping the magnetic field from 0 T up to 12 T [47].

Figure 2.5 illustrates the radio-frequency response of the beam near resonance as the magnetic-field strength B increases from 0 T to 12 T. The excitation power of the spectrum analyser was set to -50 dBm, and the resonator being tested had a mechanical quality factor Q of 2330 in the linear regime. The magnetic-field strength dependence indicates the close link to nonlinear resonance. Erbe et al [47] proposed their method to analyse the amount of nonlinearity based on the shift of resonance frequency as,

$$\delta f(B) = f_{max}(B) - f_0 = \frac{3\alpha[\Lambda_0(B)]^2}{32\pi^2 f_0} \qquad (2.4)$$

where $\delta f(B)$, $f_{max}(B)$, and f_0 are the shift of the resonance frequency, the frequency at maximum amplitude, and initial resonance frequency, respectively as shown in Figure 2.5. The α is the total amount of nonlinearity in the system, and $\Lambda_0(B)$ is the zeroth order displacement of the beam, which is given by

$$\Lambda_0(B) = \frac{lI_0 B}{4\pi f_0 \mu m_b} \qquad (2.5)$$

where l, I_0, μ, m_b are the length of the beam, input current value, damping coefficient of the system, and effective mass of the beam, respectively. Erbe et al. have

19
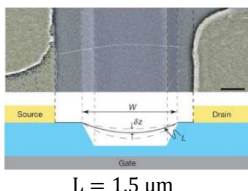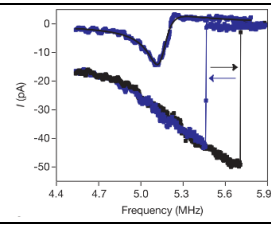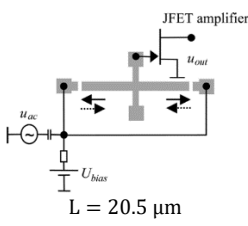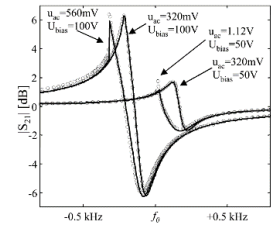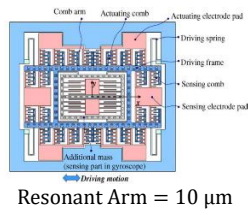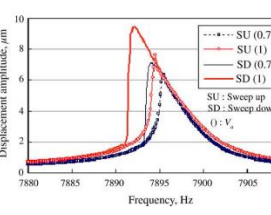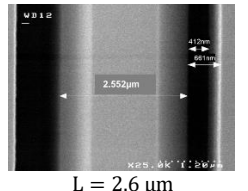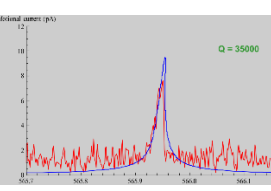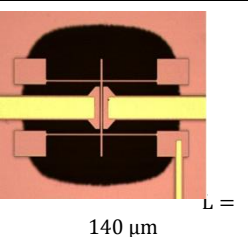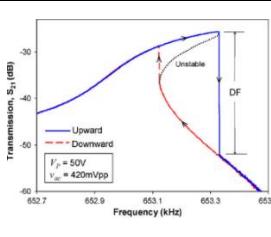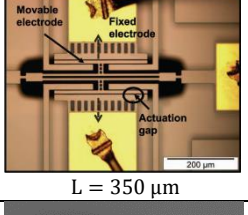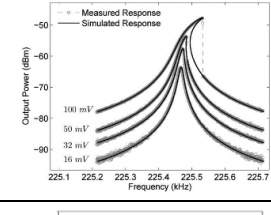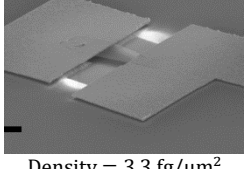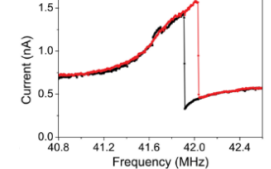
successfully demonstrated the nonlinear response for a strongly magnetic-field driven NEMS resonator which was used as a mechanical mixer in the radio-frequency (RF) regime [47]. Besides, they have shown a good agreement with the help of numerical calculations on the prototype NEMS resonator, which is a breakthrough as the very early stage of nonlinear study for NEMS resonator in 2000. The aforementioned nonlinearity studies by Andres et al., in 1987 and Erbe et al., in 2000 [15, 47] are the foundational contributions in the field of MEMS and NEMS, respectively Starting from 2004, investigation into micro-scale resonators that are directly excited electrically without magnetic field have thrived through both analytical and experimental approaches. Among the different attempts focusing on systems that are actuated electrostatically, Table 2.1 summarised notable examples with various designs, materials, and measurement techniques. Sazonova et al., [48] has firstly reported the nonlinearity study on carbon nanotube (CNT) NEMS resonators in Nature in 2004. They achieved nonlinear bifurcation observation by mixing measurement techniques via lock-in amplifier with resonance frequency at 5.3 MHz with applying the gate voltage of only 2.2 V and the mixing signal amplitude of 40 mV. The ultralow actuation used to present nonlinearity proves the advantages in the use of nanoscale devices regarding nonlinearity studies. Furthermore, the nanotube was used not only for the resonator to amplify the signal, but also as a mixer to couple the reference signal so that the lock-in amplifier can capture the resonance and then can present the result. This novel method helps then avoid unnecessary complications due to capacitive currents between the gate and the drain electrodes. Their study in signal modulation throughout the mixing techniques offers an ideal and direct way for later research in nonlinear signal detection [48].

Kaajakari et al. [40] in 2004 studied the nonlinear response of bulk acoustic wave (BAW) resonators made of silicon. The study showed that compared to their flexural counterparts, these systems had significantly higher energy storage capabilities. The other example was the work of Jeong and Ha [49] in 2005, which created a predictive model for the linear displacement limits of comb-driven resonant actuators. Three years later, the study by Palaniapan et al., in 2008 [50] introduced silicon-on-insulator (SOI) technology to a doubly-clamped MEMS resonator with the potential to co-

integrate with CMOS, while in 2013, the study by Agrawal et al. [51] designed a double-ended tuning fork silicon micro-resonator and reported nonlinear voltage dependence. In the meantime, a mathematical model based on the specific design they proposed is successfully validated via the open-loop electrical measurement, which is one of the early but comprehensive attempts of a systematic nonlinear model fitting with respect to the voltage dependence [51].

Table 2.1 Summary of nonlinearity studies in the field of MEMS/NEMS

Device	Design	Measurement	Result	
Doubly-Clamped CNT (V. Sazonova et al.,*Nature*, 2004) [48]	L = 1.5 μm	Electrical signal Mixing Measurement		Nonlinearity at $V_{DC} = 2.2$ V $f_0 = 5.1$ MHz $Q = 80$
Single-Crystal Bulk Acoustic Wave Resonator (V. Kaajakari et al., *J-Microelectromech Syst,* 2004) [40]	L = 20.5 μm	Electrical signal with network analyser, resonance signal was buffered by JFET preamplifier		Nonlinearity at $V_{DC} = 100$ V $f_0 = 11.7$ MHz $Q > 100,000$
Resonant Comb-Drive Micro-Actuator (H. M. Jeong, et al., *Sens. Actuator A.* 2005) [49]	Resonant Arm = 10 μm	Electrical signal mixing measurement with comb-drive actuator for dynamic analysis		Nonlinearity at $V_{DC} = 1.35$ V $f_0 = 7895$ Hz $Q = 3,610$
Doubly-Clamped Silicon Beam (N. Kacem et al., *Nanotech*, 2008) [52]	L = 2.6 μm	Electrical signal lock-in mixing measurement		Nonlinearity at $V_{DC} = 5$ V $f_0 = 56$ kHz $Q = 35,000$
SOI Doubly-Clamped beam (M. Palaniapan et al., *Sens. Actuator A.* 2008) [50]	L = 140 μm	Wire-bonded resonator on PCB with network analyser measurement		Nonlinearity at $V_{DC} = 50$ V $f_0 = 640$ kHz $Q = 12,000$
Double-Ended Tuning Fork Si-Micro-resonator (D. K. Agrawal, et al. *IEEE Trans. Ultrason*, 2013) [51]	L = 350 μm	Electrical signal open-loop measurement		Nonlinearity at $V_{DC} = 25$ V $f_0 = 225$ kHz $Q = 27,480$
MoS$_2$ Nano-mechanical Resonator (C. Samanta, et al., *Appl. Phys. Lett.* 2015) [53]	Density = 3.3 fg/μm^2	Frequency Modulation & Mixing measurement		Nonlinearity at $V_{DC} = 12$ V $f_0 = 41.5$ MHz $Q = 680$

With the reduced length, Kacem et al., [52, 54] reported their study and analysis on a doubly-clamped silicon beam. While the design is simple, the bridge-like design proves to be a convenient way to find physical conditions without complication in design and modelling. To anticipate the behaviours of resonators, they proposed an analytical model that considers all sources of nonlinearities. This analytical model, which is based on a reduced-order model derived from the Galerkin [34] and solved through the averaging method, offers the benefit of being straightforward and effortless for MEMS designers to apply. Furthermore, their model makes it possible to enhance the dynamic range of MEMS resonators by counterbalancing both the hardening and softening behaviours.

Novel material can be an alternative change that leads to clearer nonlinear response. Samanta et al reported a NEMS resonator made by two-dimensional (2D) material, Molybdenum disulfide (MoS_2). Thanks to the ultrathin thickness, with small actuation, the vibration displacement is enhanced. The mass density of the fabricated MoS_2 resonator [53] proposed is 3.3 fg/μm^2.
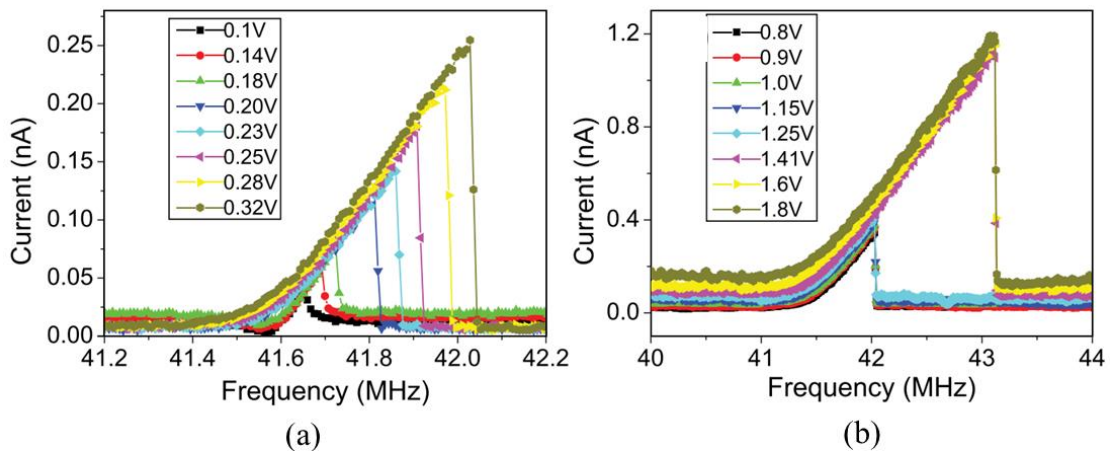
Figure 2.6 Nonlinear behaviour with respect to voltage dependence reported by Samanta et al., in 2015. (a) AC signal dependence (b) DC bias dependence [53].

The fundamental resonance mode frequency and quality factor measured by 1ω mixing technique, and frequency modulation (FM) are 41.8 MHz and 680, and 41.8 MHz and 533, respectively. Figure 2.6 shows more details about the voltage

dependence. Clear resonance 'jump' can be seen with even 0.1 V AC signal and 0.8 V DC Bias. This is attributed to the ultrasmall mass of the device where much less electrostatic force is required, compared to aforementioned devices, to drive the beam and to present substantial displacement required for the dynamics in nonlinear regime. Later in 2018, Samanta et al [39] reported their continuous study on the MoS_2 NEMS resonator by giving a much comprehensive analysis regarding the nonlinearity tuning effect.

(a)　　　　　　　　　　　　　　　(b)
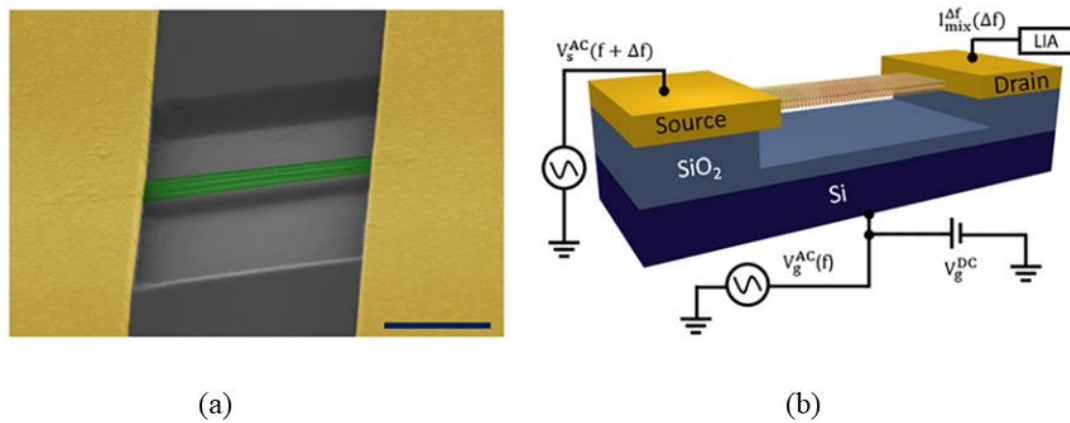
Figure 2.7 Continuous research on 2D MoS_2 NEMS resonator by Samanta et al reported in 2018 (a) A scanning electron micrograph image of the MoS_2 resonator. (b) A scheme of the measurement setup [39].

The suspended device used for the measurements is depicted in Figure 2.7(a) with a field effect mobility of approximately 15 cm^2/Vs. Figure 2.7(b) shows a simplified measurement setup and a schematic of the resonator. The measurements were conducted at room temperature and in a vacuum with a pressure below 10^{-7} Torr. During their observation, the mechanism of the domination of mechanical nonlinearity and capacitive-induced electrical nonlinearity have been determined for the first time in nano-scale. Figure 2.8 presents examples of the nonlinearity dependence with respect to the different DC bias conditions. Their study has proved the displacement level is the key to the nonlinear dynamics in the system [39].
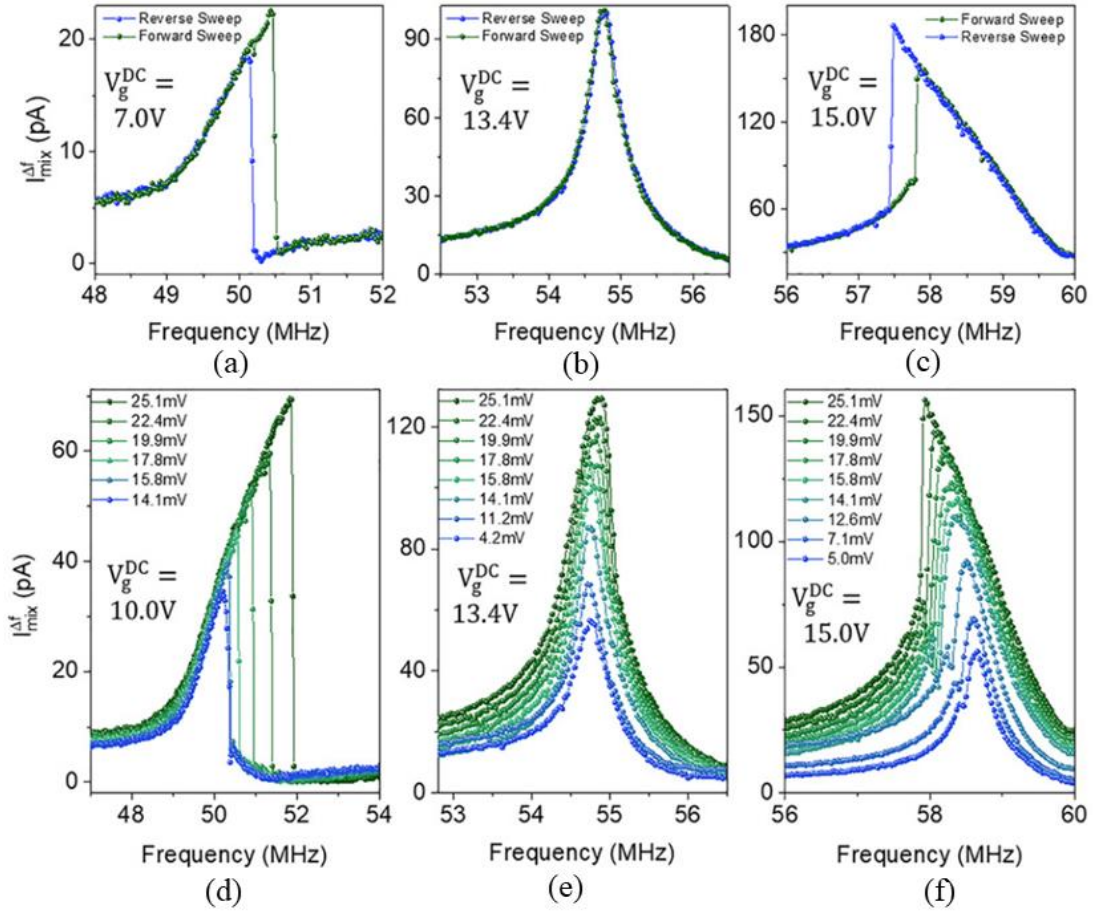
Figure 2.8 Nonlinearity tuning effect (a) to (c) Nonlinearity dependence with respect to DC bias change. (b) to (e) Nonlinearity dependence with respect to AC signal amplitude under difference fixed DC bias [39].

Figure 2.8 (a) to (c) presents the successful observation of the nonlinearity tuned from hardening under DC actuation at 10 V (Figure 2.8(a)) to linear under DC actuation at 13.4 V (Figure 2.8(b)) and to softening under DC actuation at 15 V (Figure 2.8(c)). Their result shows that the electrostatic nonlinearity of MoS$_2$ can be controlled by different DC actuation. In nonlinear theory, the flexural mode actuated resonator typically exhibits a softening effect in electrostatic nonlinearity. This effect is manifested as a shift towards higher frequencies in resonance as the DC bias increases. In Chapter 3 of this thesis, a detailed explication will be undertaken through the utilisation of high-order expansions tailored to the electrostatic force. Contrarily, the results presented in [39] demonstrate that at relatively lower DC biases (DC < 10), the

nonlinearity assumes a hardening effect. This observation can be attributed to the intrinsic mechanical nonlinearity of MoS_2, which inherently presents a hardening effect, diverging from the electrostatic nonlinearity. Generally, the degree of overall nonlinearity is positively correlated with the total driven force. Therefore, at lower driven force levels, mechanical nonlinearity governs the overall nonlinearity. As the DC bias progressively increases, electrostatic nonlinearity gradually counters mechanical nonlinearity (DC = 13.4 V) until it emerges as the predominant determinant of overall nonlinearity (DC = 15 V) [39].

2.3. Thermomechanical Noise

Mechanical motions of resonator are generally detecting the changes in electrical or optical properties, such as capacitance or reflection responsivity. However, in nanoscale, due to the ultra-sensitivity, thermal fluctuations become the significant factor which can no longer be ignored. As a natural feature, thermo-mechanical Noise (TMN) is a non-force response that can induce mechanical motion even without external excitations and therefore cause undesired oscillations and limit the sensitivity, resolution of device, and measurement errors. A NEMS resonator is known to be even more sensitive to the change due to fluctuations. Since 2000s, due to the scaling down of machining devices in micro- and nano-scale, the sensitivity was boosted and therefore TMN became one of the essential parts to be studied. Due to the ultrasmall signal, experimental method and modelling analysis are two most significant part to study TMN. In 2003, Todd et al., proposed their study on TMN in a MEMS microstructure [55].
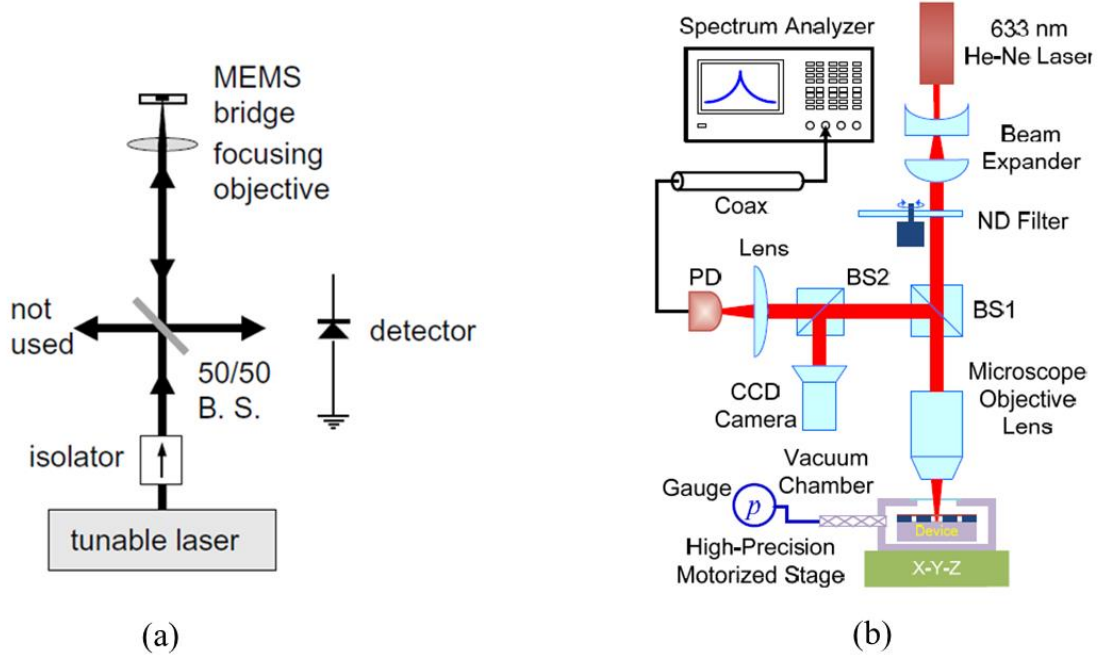
Figure 2.9 The optical setup to measure reflected power by (a) Todd et al in 2003 [55], (b) Lee et al., in 2013 [56].

Shown in Figure 2.9 (a), an absolute measurement of TMN is reported to be cooperated with a simple but high-resolution optical technique by using an optical microcavity interferometry tool, which enables displacement resolution on the order of hundreds of femto-meters per root Hz at frequencies of tens of kHz. The motion of MEMS bridge can result in the change of reflection power ΔR and because of the ultrahigh resolution, the motion due to TMN in femto-meters can be detected [55].

$$\Delta H = \frac{j+1}{2}\Delta\lambda_j = -\frac{j+1}{2}\Delta R\left(\frac{dR(\lambda_j)}{d\lambda_j}\right)^{-1} \tag{2.6}$$

Equation (2.6) is reprinted from the research by Todd et al., that explains the conversion between displacement ΔH, change of wavelength $\Delta\lambda_j$, cavity mode index j, and most importantly the change of reflected power ΔR. With this conversion path, the displacement can be directly obtained from the experiment even within femto-meters by TMN. In previous section, MoS_2 has been reported as an ideal material for innovating NEMS resonator and transducers due to its ultrathin properties. However,

27

because of the difficulties not only in fabrication of the movable devices throughout the time, but also in the vanishingly miniscule motions detection, MoS_2 NEMS resonators with resonance in very-high-frequency (VHF) bands was not yet reported until work by Lee et al. in 2013 [56]. They were inspired by Todd et al., [55] and further improved the measurement techniques, shown in Figure 2.9(b) and proposed a comprehensive model, shown in Equation (2.7) to analyse TMN for a motional-coupled MoS_2 NEMS resonator, The conversion between resonance and spectrum density is shown as below [56]:

$$S_{v,th}^{1/2}(\omega) = \sqrt{\mathcal{R}^2 \left[\frac{4k_BT}{QM_{eff}} \cdot \frac{1}{(\omega^2 - \omega_0^2)^2 + \left(\frac{\omega\omega_0}{Q}\right)} \right] + S_{v,sys}} \qquad (2.7)$$

where $S_{v,th}^{1/2}(\omega)$ is the spectrum density given by TMN motion, $k_B, T, Q, \omega_0, M_{eff}$ are Boltzmann's constant, temperature in Kelvin, angular resonance frequency, quality factor, and the effective mass of the device, $S_{v,sys}$ is the baseline of spectrum density, which can be seen as the 'noise floor'. By the given spectrum density experimental data, the Equation (2.7) can be used to extract the responsivity $\mathcal{R}$, which is a conversion factor that equals to $\sqrt{S_v/S_x}$ where S_x is the displacement spectrum density. By using the model, they achieved displacement sensitivity of 30.2 fm/Hz$^{1/2}$ and with the fundamental mode resonance-quality factor product $f_0 \times Q$ up to 2×10^{10} Hz [56].

The study in TMN not only shows the basis of the motion by a non-forced resonator, but also offers a possible and effective method to capture and analyse ultrasmall level of motions. In terms of nonlinear response analysis, the effective displacement detection technique with a resolution of pico-meter or even femto-meter scale is interesting because emergence of nonlinearity can be investigated for scaled NEMS resonators. Hence, an understanding of TMN characteristics in nonlinear NEMS devices is crucial for advancing the development and applications of nonlinear NEMS devices which have the potential for a wide range of applications including sensing,

signal processing, and communication.

2.4. Nonlinear MEMS/NEMS Applications

The origins of nonlinearity and past research on it have been introduced in previous sections. However, the potential use of nonlinearity is another factor that motivates researchers to maintain their enthusiasm on overcoming challenges in this field. Understanding the potential applications of nonlinear MEMS/NEMS is crucial because nonlinearity allows for enhanced functionality and performance in these devices. Not only can nonlinearity introduce new and unique behaviours that cannot be achieved with linear systems, such as chaos, hysteresis, and multi-stability but also it can provide unique and beneficial behaviours that are not achievable with linear systems, enabling improved sensing, energy harvesting, and signal processing capabilities. This section will present applications that utilise nonlinear MEMS/NEMS.

2.4.1. Sensing Enhancement

The improvement of output amplitude level is an ideal way to enhance the signal-to-noise ratio (SNR). Because nonlinearities can arise from large vibrational amplitudes, in the meantime, the asymmetric appearance of the amplitude-to-frequency (A-f) also reduces the stability of the oscillator. Hence, MEMS/NEMS have been limited within the linear region in many applications.

2.4.1.1. Sensor With Nonlinear MEMS/NEMS

Since 2010, novel sensing methodologies coupled the utilisation of the nonlinear have been introduced into applications to enhance the sensitivity. Younis et al. [57] explored innovative strategies for mass detection employing electrostatically actuated structures founded on nonlinear dynamics. Their investigation centered on the vibrations of microstructures near primary and secondary resonance frequencies, proposing the concept of a switch activated through the pull-in phenomenon upon the addition of mass. Similarly, Zhang et al. [58] formulated and empirically validated an innovative mass sensing principle based on parametric excitation. Their approach involved the detection of added mass through the measurement of frequency shifts at the boundary of the first-order parametric resonance.

With more exploration in nonlinearity on-going, the benefits of using nonlinearity are revealed. In 2011, Lee et al., [59] demonstrated stable operation of the MEMS oscillator beyond the critical vibration amplitude. A single-crystal-silicon double-ended tuning fork (DETF) resonator was embedded in a variable-phase closed-loop system so that the strong nonlinear regime can be recorded by tracking the bifurcated A-f characteristics of the resonator. In the experiment, they successfully proved that power-handling performance of the MEMS oscillator can be improved by operating them in nonlinear regime [59]. Their success inspired more researchers to exploit more possibilities for MEMS/NEMS to be used stably in nonlinear regime. Years later, it has been reported in Ref. [59-63] that nonlinear miniature resonators possess the potential benefits for SNR and frequency stability. Meanwhile, Ref.[60, 64] proved that noise reduce can be achieved by operating near or at bifurcation point.

Bouchaala et al. [65] proposed a nonlinear-based MEMS sensor and switch for gas detection. Their study highlights the importance of using the nonlinear response of an electrostatically actuated resonator for gas sensing. By employing a clamped-clamped microbeam coated with the sensitive thin-film layer, real-time frequency shifts and added mass detection are achieved, triggering switches upon reaching specific thresholds. Their research presents two switch concepts based on resonator behavior

shifts, offering potential for immediate responses to hazardous gas detection, though sub-micron and nano-scale resonator scaling may intensify noise concerns.

2.4.1.2. Real-time Sensing Dynamic Range Enhancement

Sansa et al., [18] reported their achievement in the real-time sensing enhancement by operating the NEMS resonator in nonlinear regime. Shown in Figure 2.10(a), a doubly-clamped silicon NEMS resonator ($L = 10\,\mathrm{\mu m}$, $W = 300\,\mathrm{nm}$) with electrostatic actuation and piezoresistive (PZR) detection was used experimentally.

(a)   (b)
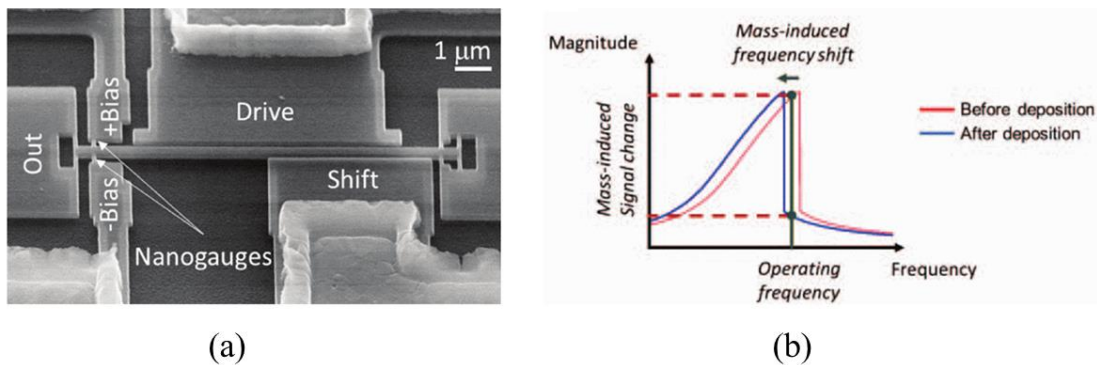
Figure 2.10 (a) A doubly-clamped crystalline silicon NEMS resonator fabricated by (b) Real-time nonlinear measurement near bifurcation point. [18].

During the real-time frequency response measurement, the resonator was operated at a bifurcation point with clear bi-stability presented in A-f response. As shown in Figure 2.10 (b), with a small mass-induced shift of the resonance frequency, a significant frequency change is detected in real-time. Based on this setup, they demonstrated the great sensitivity enhancement of frequency shifts of 200 Hz corresponding to the deposited mass of 15 ag [18].

2.4.1.3. Energy Harvesting

Energy conversion is the most significant part in the field of energy harvesting for next generation green electronics. Among the applications, most are using vibrational energy which is then converted into electrical form of power through a piezoelectrical material, electromagnetic or electrostatic transducer. Many of energy harvester are based on mechanically resonant devices which are operated within the linear regime and collect a narrow band of vibrations. However, as many ambient vibrations stem from a wide range of forms including seismic noise, vehicle motion, TMN, or all other types of noisy equipment. Therefore, proposing a method that can enhance the sensing range can largely improve the efficiency of the energy harvesting devices.

Ando et al., [66] proposed a prototype of MEMS for energy harvesting based on the bistable structure. The new attempt of utilizing nonlinearity to enhance the sensing range allows the energy to be collected from a wide spectrum of frequencies than traditional linear system. They initially demonstrated the principle on a macro cantilever prototypes in millimetre scale [66] and later downscaled their design into microscale. A bistable back etched SOI MEMS (BESOI-MEMS) was fabricated, shown as Figure 2.11, with a permanent magnet next to BESOI-MEMS, the vibration of the beam can change the distance between two magnets. When the fixed magnet is close enough to the tip of the beam, the behaviour of the beam is nonlinear where the new equilibrium positions appear, so a bistable potential energy function imposes the dynamic.
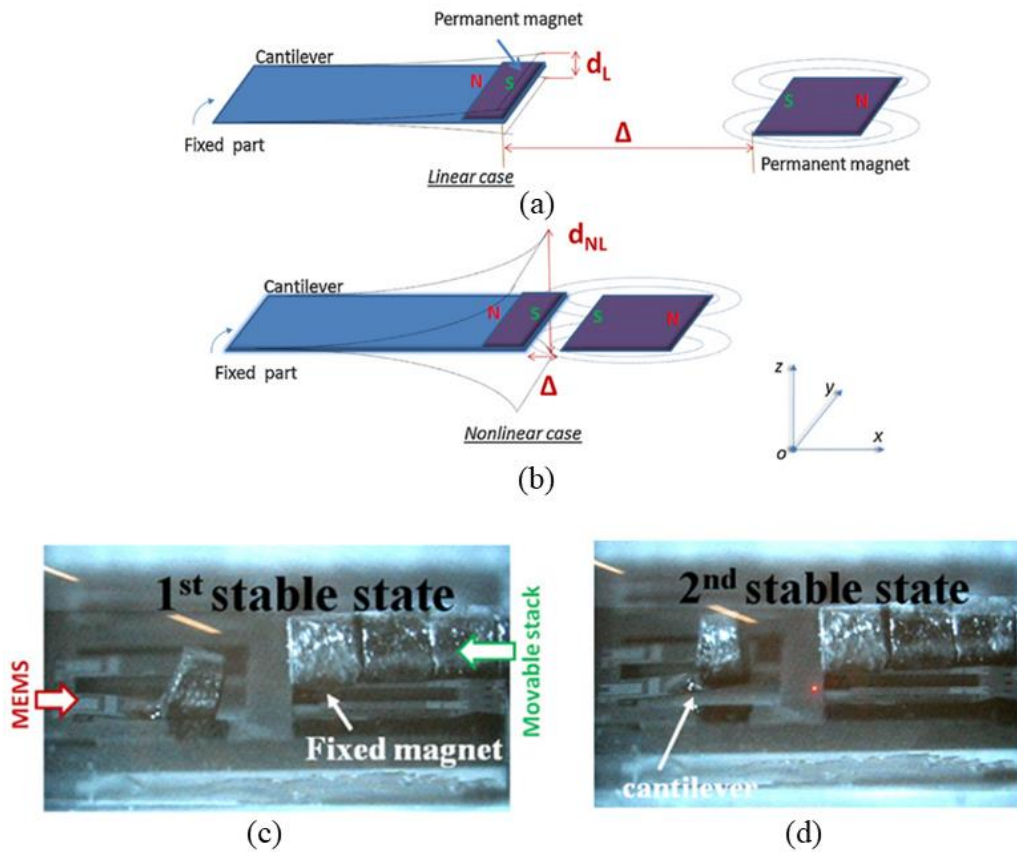
Figure 2.11 BESOI-MEMS cantilever. (a) Far from permanent magnet, operating in linear regime. (b) Close to permanent magnet, operating in nonlinear case. (c) and (d) SEM image [66]
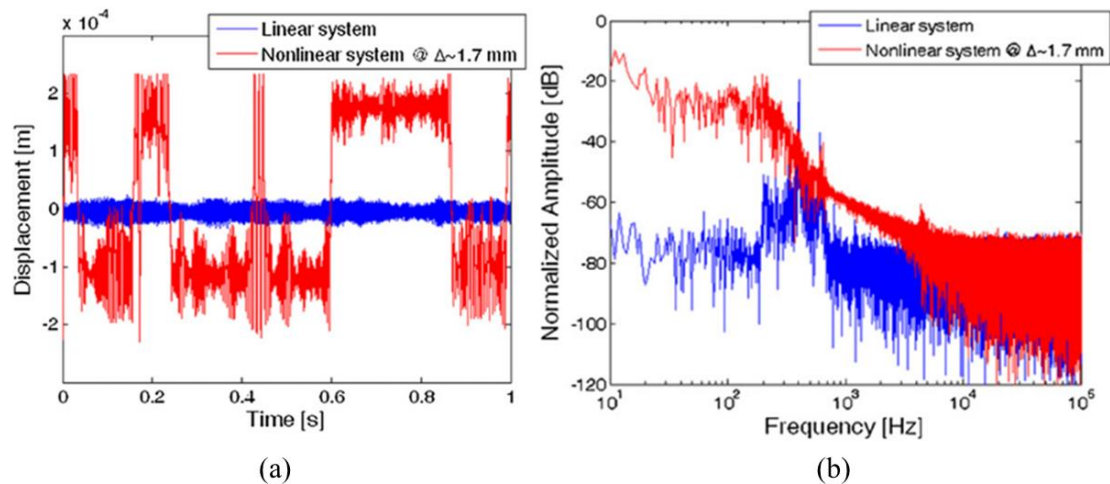
Figure 2.12 Experimental results by Ando et al., (a) Displacement of the cantilever tip (b) Displacement spectrum [66].

Figure 2.12 presents the interesting result in the perspective of energy harvesting applications. Figure 2.12 (a) shows the evolution of the displacement where Figure 2.12(b) shows the frequency response of the displacement. Both results show the improvement of the nonlinear system with respect to the displacement and spectrum that appear wider compared to the linear case. The experimental results confirmed that the MEMS device successfully demonstrated the nonlinear bistable behaviour principle. Additionally, it was shown (as predicted by the simulations) that the device significantly improved the conversion of kinetic energy from external vibrations across a wide frequency range, compared to a linear resonant device [66].

2.4.2. Nonlinear Coupled MEMS/NEMS in Neuron Network

Nonlinear MEMS and NEMS devices have been proved to possess significant importance in neuron network applications in recent years due to their ability to mimic the behaviour of neurons and synapses in biological systems. They can create spiking neural networks that simulate the behaviour of biological systems more accurately. Also, these devices have small sizes, low power consumption, and can be integrated into complex systems, making them ideal for constructing high-density neural networks. They can operate at high frequencies, enabling real-time processing of neural signals in applications such as brain-machine interfaces. Additionally, nonlinear MEMS/NEMS devices can be used for signal processing and filtering, removing noise and artifacts from neural signals, improving the accuracy of neural signal processing and reducing the risk of errors.
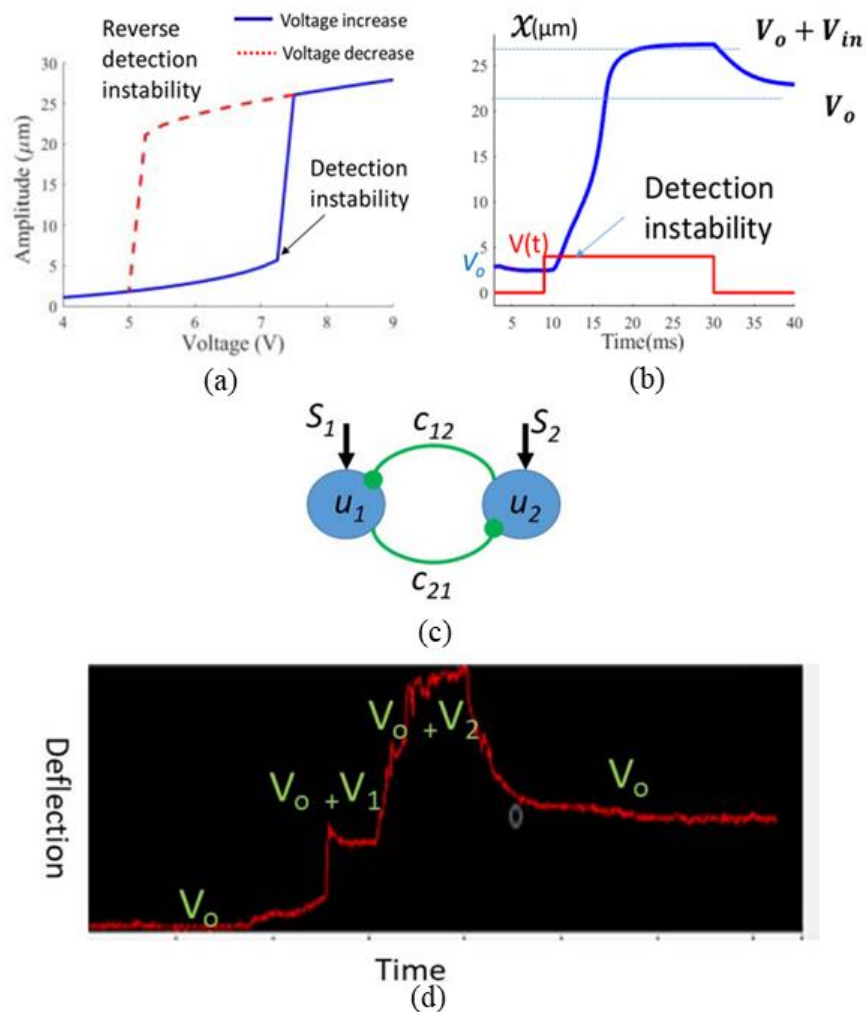
Figure 2.13 Dynamics of a coupled DFT neuron (a) Detection neuron by producing high amplitude jump. (b) Memory neuron by retaining high amplitude position after the excitation lost. (c) A scheme of the dynamics of two DFT neuron. (d) Experimental data of the memory neuron when detection neuron is instable [24].

In 2018, Alsaleem et al., [24] proposed their novel concept for the MEMS neural computing unit, which is a qualitative neuron approach to model cognition and human behaviour, based on the neuron rate model theory which is the basis of the dynamic field theory (DFT).

The concept of using nonlinear dynamics of MEMS resonators, bi-stability more specifically, is the key to simulate the detection and memory of a single rate model

neuron. Figure 2.13 presents the work by Alsaleem et al regarding dynamics of DFT neuron. Two DFT neurons (detection neuron and memory neuron) are coupled with each other as Figure 2.13 (c) shows. Figure 2.13 (a) is the bi-stability behaviour of detection neuron with external voltage-controlled nonlinearity. Figure 2.13 (b) is the memory neuron, when the detection neuron becomes instable, the memory neuron received the signal from the coupled detection neuron, retaining high amplitude position. Figure 2.13 (d) is the experimental real-time result that confirms the detection instability and what appears to be a memory behaviour using the nonlinear MEMS devices.

Their research successfully demonstrates that a MEMS device with electrical resonance activation or initial curvature behaves similarly to a DFT neuron in terms of dynamics. This makes it a promising option as an analogue-based building block for a new type of computing unit based on the human neuron. Therefore, this new MEMS neuron-computing unit has the potential to create analogue brains consisting of devices that respond to stimuli in a manner similar to human neurons. In 2019, researcher Rafaie et al from Alsaleem's group [23] proposed their further attempt by building a recurrent neural network with 14 nonlinear MEMS neurons, schematically shown in Figure 2.14.
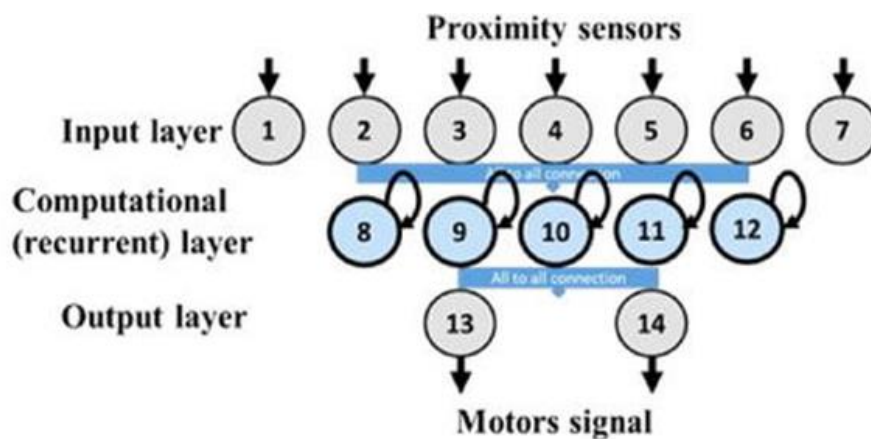
Figure 2.14 A recurrent neural network by 14 nonlinear MEMS neurons [23].

Each of the MEMS retains the memory of past inputs via bi-stability and hysteresis

36

and receives weighted feedback from other coupled devices in the network. MEMS is actuated via electrostatic force $V_{MEMS,i}$, makes it an ideal way to control and monitor the signal. A model of a general neural network with the voltage across each of MEMS device is given by Rafaie et al., [23] as follows,;

$$V_{MEMS,i} = V_{b,i} + \sum_{j=1}^{M}\left[w_{sensor,j}V_{sensor,j}(D_j)\delta_{ij}\right] + \sum_{j>1}^{n}\left[w_{ij}V_{out,j}(z_j)\right] \qquad (2.8)$$

where M is the number of input MEMS neurons, n is the number of the total number of MEMS neurons in the network, $V_{b,i}$, δ_{ij}, $w_{sensor,j}$, V_{sensor}, D_j are the DC bias, Kronecker delta function (in the dynamic field theory), weight applied to the input voltage from j-th sensor, the sensor output voltage, and the distance to the object, respectively [23]. This model describes how signal passes within each j-th sensor and gives the principle of how weight w_{sensor} is affected by the voltage on MEMS neurons, leading to the success on training the MEMS neural network with preset electrical signals. More details is in [23]. Coulombe et al., [22] from Sylvestre group reported their novel trails on the success of reservoir computing (RC) based on coupled nonlinear MEMS as virtual neurons. As a preliminary study from their team, the result demonstrated that the network of nonlinear MEMS oscillators with linear coupling are able to carry out intricate computations. Numerical simulation was used to present by testing a single network on two very different benchmarks tasks (computing parity functions and spoken words classifying). One year later, Sylvestre group reported the continuous study on coupled nonlinear MEMS in RC applications. They used delay-coupled MEMS to perform the time series classification tasks with error rates below 0.1% and accuracy of $(78 \pm 2)\%$ for spoken word recognition benchmark [67].

2.5. Summary

Nonlinearities in MEMS/NEMS have been explored for decades. In this chapter, the various origins of nonlinearities in MEMS/NEMS have been studied. The constant investigation in nonlinear MEMS/NEMS inspired researchers to propose vast types of designs such as doubly-clamped beam, comb-driven micro-plate, and DETF beam, which has presented their strengths to study geometric nonlinearities. In the nonlinearity characterisation, the customary approaches typically entail modelling and characterising it by considering distinct origins of nonlinearity. Various groups of researchers have employed diverse modelling methodologies to characterise nonlinear behaviours. For instance, Andres et al., [15] adopted an analytical approach in the early 1980s to model the nonlinear components separately. In contrast, Erbe et al., [47] focused their analysis on modelling the frequency shift induced by nonlinearity. Samanta et al., [39] meanwhile, combined observations of MoS_2 with the Duffing equation to connect nonlinear frequency response with voltage dependence. They conducted numerical analysis using the 4th-order Runge-Kutta method. This series of studies not only unveiled the omnipresence of nonlinearity in distinct microsystems and materials but also underscored the application of third-order response coefficients to quantify nonlinear traits. These insights have served as inspiration for the nonlinear modelling theory in this thesis. Historically, the characterisation of nonlinearities typically involved separate modelling of nonlinear regions, analytical approaches, or common numerical analysis methods. While these methodologies proved effective in their individual projects, disparities between their models and actual systems endured. Analytical analysis often led to significant fitting errors, particularly evident in the fitting of VHF band data, as demonstrated by Zega et al., [30, 38] due to the natural phenomenon that third-order system has no analytic solution. Previous numerical approaches either focused on independently modelling nonlinear regions or directly employed general numerical analysis packages for computer-based computations. These approaches lacked a direct connection to MEMS/NEMS oscillators. Moreover, they did not incorporate the voltage dependence of the system's nonlinear frequency response into the model, constraining their discussions to experimental outcomes and

phenomenological levels. Building on this context, this thesis introduces an innovative modelling methodology that disentangles the intrinsic and electrostatic nonlinearities of the system, ultimately amalgamating them into a comprehensive model.

CHAPTER 3

Si-NEMS Resonator Structure and Modelling

The performance of semiconductor devices constantly benefits from the progress of scaling down, such as higher integration density and lower power consumption. However, because of the increasingly complex in the design and structure, challenges in characterization have been the key for further development and optimization. For the characterization of classic static semiconductor devices such as field-effect-transistors (FETs), one of the prior studies is completed by using modelling techniques, for instance, the Berkeley Short-Channel IGFET Model (BSIM) [68], which has provided a convenient way to gain the understanding of the characteristics. For the motional nano-scale device like NEMS, modelling becomes even more important, because direct observation of the vibrational characteristics in its high-frequency or very-high-frequency (VHF) range is indeed difficult. Interdisciplinary physics including electro-mechanical coupling makes it more difficult understand full device operation accurately.

Powerful tools such as COMSOL [69] and ANSYS [70] are widely used to perform detailed and accurate finite-element-analysis (FEA) simulations of NEMS resonators and other NEMS-based physical systems. They offer graphical user interface (GUI) that allows users to build and solve multi-physics problems in a convenient and direct

way. However, due to the nature of nonlinearity, not only the convergence of FEA could be computationally expensive and time-consuming, but also a way to describe the underlying physical phenomena that give the rise of its behaviour is essential but cannot be covered fully. Nonlinear behaviour in NEMS can arise from a variety of physical phenomena, such as nonlinear material properties, mechanical instabilities, and coupling between mechanical and electrical properties. These phenomena can be difficult to understand and predict without a mathematical model that captures their essential features.

This chapter will focus on the methodology about the nonlinear behaviour of doubly-clamped Si-NEMS resonators. First, in relation to the structure explanation, device fabrication process will be introduced briefly. Later, the process of building a mathematic nonlinear model associated with actual Si-NEMS resonators will be explicitly presented within the third section of this chapter, including solving the steady-state solutions for the equation with the cubic nonlinear term. Lastly, the experimental techniques including frequency-modulation (FM) and 1-ω mixing measurement will be described in detail.

3.1. Device Fabrication

Doubly-clamped silicon NEMS resonators (Si-NEMS) are used for the nonlinearity study in this project. Samples were designed by F. A. Hassani et al., [25] and fabricated by my collaborators in Commissariat à l'Energie Atomique et aux Energies Alternatives Laboratoire d'électronique des technologies de l'information (CEA-LETI) under the former EU FP7 NEMSIC project. Because a thorough understanding of the structural feature of the Si-NEMS is required prior to the modelling, first, we start with the introduction of fabrication process, which is based on CEA-LETI technology, given in Figure 3.1.
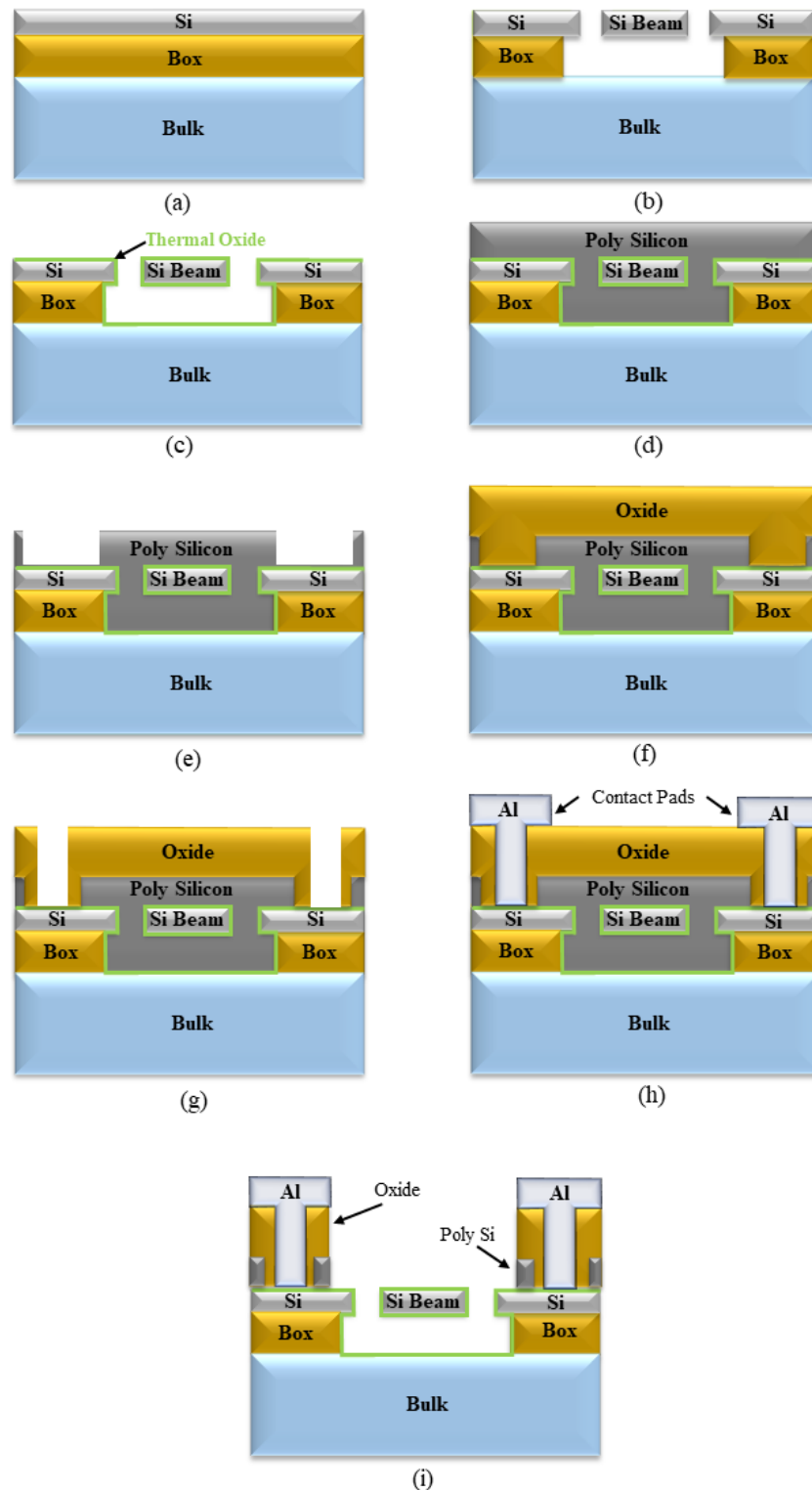
Figure 3.1 Scheme for fabrication process of Si-NEMS: (a) SOI substrate preparation. (b) Doubly-Clamped beam structure definition (c) Thermal oxidation (d) Sacrificial layer deposition (e) Contact area open(f) Oxidation (g) Contact holes open within oxidation layer (h) Metallization (i) Polysilicon etching [25].

The NEMS resonators were fabricated based on silicon-on-insulator (SOI) platform. The thickness of SOI layer and the box layer are 45 nm and 150 nm, respectively. The SOI wafters were heavily n-type doped with the concentration at 4×10^{19} at.cm^{-3}. The beams were pattern defined and released with vapor HF as shown in Figure 3.1(b). For passivation and minimizing the surface states, a 14-nm-thick silicon dioxide (SiO$_2$) layer was then developed via thermal oxidation (Figure 3.1(c)) around the surface of the device and the suspended beam. Then, the poly silicon was deposited on the surface to fill the etched area around the beam and followed by chemical-mechanical polishing/planarization (CMP) in order to protect the beam from further processing steps.

The holes for contact in Figure 3.1(e) were patterned by etching the poly silicon sacrificial layer with the etch stop at thermal oxide layer. Later, an oxidation layer was deposited on the surface (Figure 3.1(f)) to fill the contact holes. The holes for contact pads were defined in Figure 3.1(g) and aluminium was deposited to pattern the contact pads in Figure 3.1(h). Figure 3.1(i) is the final step where xenon difluoride (XeF$_2$) was used to open a window in oxide and polysilicon above the beam to form the suspension of the beam. With the actuation applied via bottom gate, the beam oscillates periodically along with the RF signal applying through the beam. In this thesis, the fundamental mode is focused, in other words, beam oscillates vertically in out-of-plane mode. COMSOL simulation for NEMS resonators have been comprehensively completed by Hassani et al., [25] and their result displayed the fundamental mode frequencies of beams with various dimensions. This outcome is employed within this paper to ascertain the experimental resonance modes. This holds significance due to distinct resonance modes implying differing beam oscillation patterns. Given that the paper's modeling method predominantly targets the fundamental mode, this approach ensures the accurate determination of the resonance mode aligned with the study.

Figure 3.2 shows the detail of design and the SEM view of sample to prove the success of the suspended beam formation. Table 3.1 summarises the dimension details of samples, which will be further studied and modelled in later sections.

Table 3.1 Sample dimension summary (Unit: nm)

Sample	I_B	w_B	I_c	g_0
S1	2000	105	1840	
S2	2000	135	1840	
S3	1500	105	1340	80
S4	1500	135	1340	
S5	1000	105	840	
S6	1000	45	840	
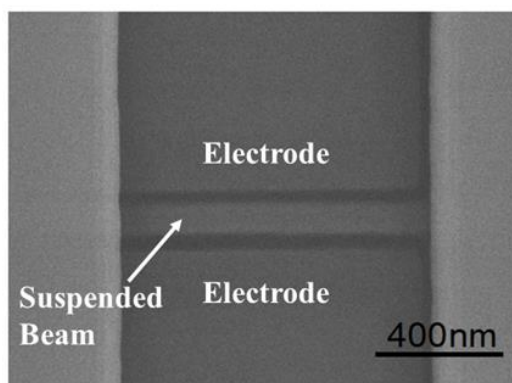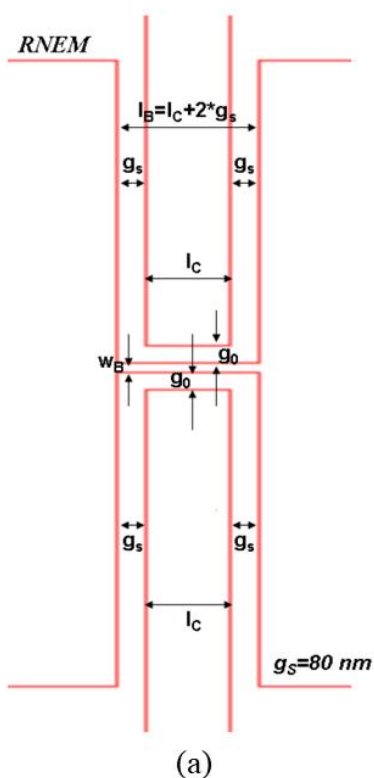
Figure 3.2 Structure of Si-NEMS (a) Design and parameter definition. I_B, I_C, g_S, g_0, w_B are the beam length, side-gate length, gap from side-gate to source/drain, gap between gate and beam, and the beam width, respectively [25]. (b) SEM observation

The doubly-clamped Si-NEMS resonator is conductive due to the heavily doped feature. As the design is based on the similar structure of a common transistor, the input and output of the NEMS resonators are therefore correspondingly named as Source and Drain. The two lateral located electrodes are side electrodes, and the substrate serves as the back electrode. The following section will introduce the model for the characterisation of NEMS resonators. Noted that, for the convenience of expression, the dimensional parameters length, width, thickness, and gap between beam and electrodes is marked as L, W, t, and g_0 which correspond to l_B, w_B, and SOI layer thickness, respectively.

3.2. Model

3.2.1. Duffing Equation

Section 2.1.1 introduces the difference between EBT and Duffing model. Because of the symmetric sample design, the geometric nonlinearity is negligible. On the other hand, nonlinearities induced by imperfections are typically unrelated to frequency and the strength of the input signal. Consequently, they manifest as disorderly, random phenomena, causing instability in experiment. However, in this work, after extensive prolonged testing, such phenomena were not observed. Additionally, within the low-intensity signal input range, the resonance exhibited stable symmetric peaks. Furthermore, I conducted scanning electron microscopy (SEM) observations on selected samples and did not identify significant structural imperfections. Thus, within this work, I assume that the NEMS beams fabricated by Hassani et al. at CEA-LETI are devoid of imperfection-induced nonlinearity. Therefore, nonlinearities due to fabrication and contact are also ignored. Hence, Duffing equation is more applicable as mechanical and electrical nonlinearities are focused on this research [71]. The first use of Duffing equation associated to nonlinear analysis can be traced back to 1928 where Lachmann et al., used Duffing equation to solve a forced vibrational of pendulum problems [72]. Later Friedrichs et al., proposed the first trail to introduce a

cubic nonlinear term to specify the order of nonlinear restoring force in the series of lectures in Brown University [73]. This nomenclature has become a widely accepted way to describe the nonlinear behaviour for a Duffing oscillator to very recent decade [74].
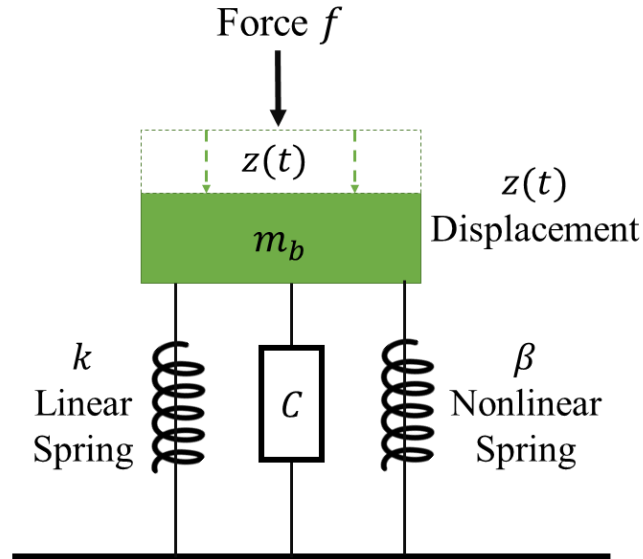
Figure 3.3 Scheme of a driven SDOF mechanical nonlinear oscillator

In general, Duffing equation describes the states of an oscillator in its equilibrium position based on Newton's law. For an n-th degrees of freedom system, it takes the form as follows:

$$[M]z'' + [C]z' + [K]z = f^N(z,t) \tag{3.1}$$

where z'', z' and z are displacement, velocity, and acceleration of the oscillator. $[M]$, $[C]$, and $[K]$ are $N \times N$ matrix of mass, damping, and linear stiffness respectively. $f(z,t)$ is a component that depends on the time domain displacements of the oscillator comprising all the external forces applied on the oscillator and elastic force. Equation (3.1) is known as the second-order Duffing equation.

In this thesis, only single degree of freedom (SDOF) is considered as it is sufficient to

understand the utility and applications for a single nonlinear doubly-clamped beam. For the coupled oscillator network, two or multiple degrees of freedom should be taken into consideration based on the model proposed in this thesis.

3.2.2. Mechanical Nonlinear Coefficient

To model the origin of nonlinearity, I start from the very basis of the motion. SDOF universal equation of motion based on Newton's Law is considered:

$$m_b \frac{\delta^2 z(t)}{\delta t^2} + C \frac{\delta z(t)}{\delta t} + Kz(t) = f(z,t) \qquad (3.2)$$

where m_b, K, C, and $f(z,t)$ are beam mass, spring, damping, and driven force. Correspondingly, each term in the equation represents different portion contributing in the system, where $m_b \, \delta^2 z(t)/\delta t^2$ stands for the inertia, $C \, \delta z(t)/\delta t$ is damping, $Kz(t)$ is the restoring force. From a basic theory of the origin of nonlinearity described in Chapter 2, the mechanical nonlinearity stems from the intrinsic mechanical properties of the spring. Hence, the spring constants K can be considered as an integrated factor that possesses multiple orders of spring constants [23, 26, 28, 44]. We process the restoring force $Kz(t)$ with perturbation series expansion, written as,

$$Kz(t) = k_0[z(t) + k_1 z(t)^2 + k_2 z(t)^3 + \cdots + k_{n-1} z(t)^n + \cdots] \qquad (3.3)$$

where k_0 is the linear stiffness coefficient and k_n is defined as a stiffness coefficient of a $z(t)^{n+1}$ term. In a flexural model, for other geometries such as bulk acoustic wave resonator the even-order restoring force (n = 2, 4, 6 …) like k_1 is nonzero due to geometric nonlinearity [40]. However, as for the symmetric design of the structure in my case, the geometric nonlinearities can be ignored as the even-order nonlinear

47

restoring force are balanaced against each other and only odd-order restoring force exists. One the other hand, the displacement $z(t)$ remains less comparable to the initial gap g_0, so the higher order terms of n > 4 are negligible. The $z(t)^3$ term remained represents nonlinearity deduced from the mechanical stiffness term and the cofficient k_2 is equivalent to the mechanical nonlinear stiffness β_m;

$$Kz(t) = k_0 z(t) + k_0 \beta_m z(t)^3 \qquad (3.4)$$

Figure 3.3 presents the scheme of an elementary SDOF mechanical oscillator driven by the force $f(z,t)$.

$$m_b \frac{\delta^2 z(t)}{\delta t^2} + C \frac{\delta z(t)}{\delta t} + k_0 z(t) + k_0 \beta_m z(t)^3 = f(z,t) \qquad (3.5)$$

where $k_0 \beta_m$ is the nonlinear spring β in Figure (3.3). Although Equation (3.5) is structurally identical to a commonly-known Duffing equation, it is important to discuss the origin of nonlinearity because this emphasizes the discussion of nonlinear origins to improve accuracy of modelling. The process of expanding and handling perturbations on the restoring force in this thesis reflects the discussion and contemplation of mechanical nonlinearity and geometric nonlinearity. Furthermore, the way of how to treat different k_n coefficients in the Equation (3.3) is entirely based on the actual device we have. As a result, this part of the process also makes my modelling more closely aligned with the actual Si-NEMS resonator device.

In Equation (3.5), C can be substitute as the function of resonance frequency ω_0 and quality factor Q. They are given by the following derivation process.

$$C = \xi C_c \qquad (3.6)$$

where ξ and C_c are damping ratio and critical damping coefficient. They have the relationship with stiffness and quality factor as below,

$$C_c = 2\sqrt{k_0 m_b} \tag{3.7}$$

$$\xi = \frac{1}{2Q} \tag{3.8}$$

As k_0 stands for the fundamental mechanical stiffness, it can be substitute by the simple mass-spring equation as,

$$k_0 = \omega_0^2 m_b \tag{3.9}$$

Substitute ξ and C_c in Equation (3.6) with Equations from (3.7) to (3.9), we have,

$$C = \frac{\omega_0 m_b}{Q} \tag{3.10}$$

By substituting k_0 and C by Equation (3.9) and (3.10), the mass normalised Equation (3.5) is therefore written as,

$$\frac{\delta^2 z(t)}{\delta t^2} + \frac{\omega_0}{Q}\frac{\delta z(t)}{\delta t} + \omega_0^2 z(t) + \omega_0^2 \beta_m z(t)^3 = \frac{f(z,t)}{m_b} \tag{3.11}$$

3.2.3. Electrical Nonlinear Coefficient

As aforementioned in Chapter 2, for an electrical-driven resonator, electrostatic force is another important source of nonlinearity. At the start of this project, Tsuchiya et al. [27] have reported the experimental observation regarding the voltage dependence with Si-NEMS resonator, shown as Figure 3.4

(a)   (b)
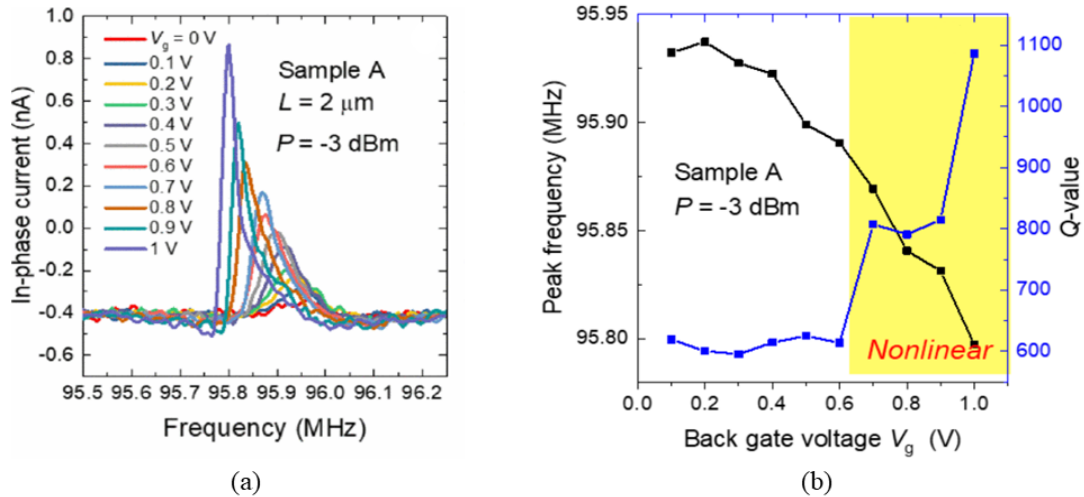
Figure 3.4 Voltage dependence observation by Tsuchiya et al. (a) Resonance peak with respect to increase of back gate voltage V_g for sample $L = 2$ μm (b) The summary of peak resonance and quality factor Q with respect to back gate voltage [27].

The result of experimental observation by Tsuchiya et al shows the increase of V_g leads to the softening effect for resonance. In the meantime, when V_g exceeds 0.6 V, the resonance curve starts to 'bend' to left, causing an asymmetric shape of resonance. This indicates the existence of higher-order frequency response term is gradually dominating the resonance. In other words, this study clearly presented the evidence of the occurrence of electrical nonlinearity in Si-NEMS resonator. Hence, as the continuous research, the modelling for electrical nonlinear resonance is important. Considering the resonator beam and back gate as a scheme of parallel capacitive plates, shown in Figure 3.5 as below,

50
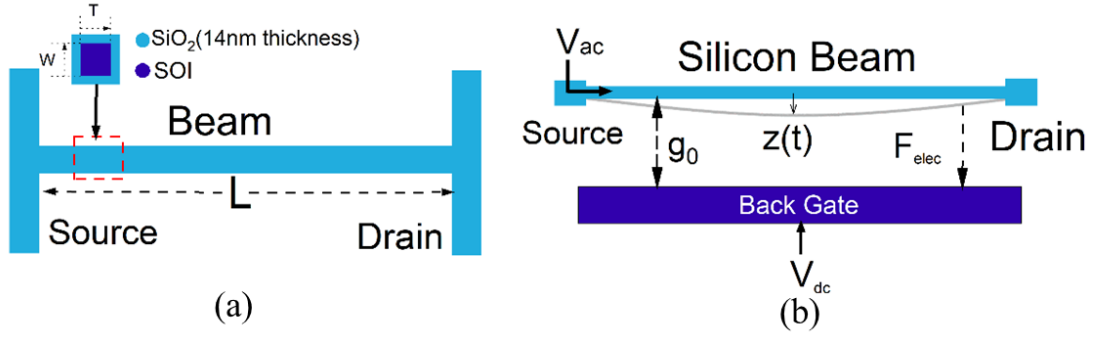
Figure 3.5 Scheme of Si-NEMS electrical characteristics (a) A top view of the NEMS beam. (b) A scheme of a cross-sectional view showing silicon nano-beam vibration characteristics

Given the RF signal with the amplitude V_{AC}, the DC bias on the back gate as V_{AC}, the net voltage between beam and back gate is

$$|V(t)| = V_{AC} + V_{AC} \tag{3.12}$$

Noted that in time-domain, V_{AC} is in form of $V_{AC}e^{i\omega t}$ where ω is the angular frequency. The following derivation focuses on the instantaneous amplitude of displacement; therefore, Equation (3.6) uses the amplitude of RF to calculate the absolute value of $V(t)$. The surface charge density σ on the plates can be found using the relationship between the electric field and charge density as,

$$\sigma(t) = \varepsilon_0 E(t) \tag{3.13}$$

where ε_0 is the permittivity in vacuum ($\varepsilon_0 \approx 8.85 \times 10^{-12}$ F/m) and $E(t)$ is the electric field that equals to $V(t)/g_0$. Having the electrostatic force F_{elec} as,

$$F_{elec} = \frac{1}{2}\sigma(t)E(t)S \tag{3.14}$$

where S is the area which is the product of length L and width W. Substitute

51

$\sigma(t), E(t)$ and S in Equation (3.14) with Equation (3.12) and (3.13), I have,

$$F_{elec} = \frac{\varepsilon_0 LW (V_{DC} + V_{AC})^2}{2g_0^2} \tag{3.15}$$

Nonlinearity often occurs when the displacement z is not negligible compared to the gap g_0. By considering z, I have,

$$F_{elec} = \frac{\varepsilon_0 LW (V_{DC} + V_{AC})^2}{2[g_0 - z(t)]^2} \tag{3.16}$$

To extract the high order terms from electrostatic force F_{elec}, I process Equation (3.16) with Maclaurin expansion [75] near the initial equilibrium point $z = 0$,

$$F_{elec} = \frac{\varepsilon_0 LW (V_{DC} + V_{AC})^2}{2g_0^2} \left[1 + \frac{2}{g_0} z(t) + \cdots \frac{n+1}{g_0^n} z(t)^n \right] \tag{3.17}$$

By using the same criteria as illustrated in previous section, due to the symmetry of design and ultrasmall scale of displacement, we extract first order term (n = 1) and third term (n = 3) from the Maclaurin series, giving the simplified equation as,

$$F_{elec} = F_{elec}^0 + \frac{\varepsilon_0 LW (V_{DC} + V_{AC})^2}{g_0^3} z(t) + \frac{2\varepsilon_0 LW (V_{DC} + V_{AC})^2}{g_0^5} z(t)^3 \tag{3.18}$$

where F_{elec}^0 stands for the initial electrostatic force which is identical to Equation (3.15). The coefficient of $z(t)$ contributes the overall linear function of stiffness where the coefficient of $z(t)^3$ contributes the overall nonlinear function of stiffness. As they are voltage dependent, hence, they explain the mechanism of voltage-tunning effect with respect to resonance shift due to linear stiffness change and nonlinear voltage dependent effect, respectively. For the convenience, I mark them as k_e and β_e,

which stands for linear and nonlinear equivalent electrical stiffness, respectively, being given as,

$$k_e = \frac{\varepsilon_0 LW(V_{DC} + V_{AC})^2}{g_0{}^3} \tag{3.19}$$

$$\beta_e = \frac{2\varepsilon_0 LW(V_{DC} + V_{AC})^2}{g_0{}^5} \tag{3.20}$$

Merging the above equation with Equation (3.11), I express the motional characteristics of Si-NEMS resonator as in one equation including the voltage-dependent electrical stiffness and mechanical stiffness in both linear and nonlinear regime.

$$z(t)'' + \frac{\omega_0}{Q} z(t)' + \left(\omega_0^2 - \frac{k_e}{m_b}\right) z(t) + \left(\omega_0^2 \beta_m - \frac{\beta_e}{m_b}\right) z(t)^3 = \frac{F_{elec}^0}{m_b} \tag{3.21}$$

The increase of voltage will lead to the increase of k_e and correspondingly the overall stiffness $\omega_0^2 - k_e/m_b$ will then decrease, causing the left shift of resonance frequency, which is the softening effect. Same theory applied on the nonlinearity where the increase of voltage leads to the decrease of cubic stiffness, showing as the result in Figure 3.4 that the top of resonance curve 'bend' to left.

Noted that m_b is the sum of effective mass of silicon and the surrounding SiO_2 where the actual width and thickness of silicon layer should be corrected by considering the growth of SiO_2 via thermal oxidation. 8 nm-thick Si is sacrificed during the oxidation process to grow 14 nm-thick SiO_2. Hence, the designed width and thickness of Si will need to be corrected accordingly. As for effective mass calculation, it requires complex consideration including crystalline structure of Si and SiO_2. Density function theory or experimental observation are commonly considered to obtain the effective mass. For simplicity, the effective mass is calculated by considering the theory

proposed in [12] and [26] as;

$$m_b = 0.735\rho W_B L t_B \tag{3.22}$$

where m_b is effective mass, ρ is the density of beam, W_B, L, t_B are the beam's width, length, and thickness, respectively. Equation (3.21) is the target model which is a time-domain form with the cubic nonlinear term that makes analytically unsolvable. The following section will present a novel way of utilizing a computational numerical method to obtain the steady-state solutions for Equation (3.21).

3.3. Model Solution and Simulation

In solving a differential equation like Duffing equation with a cubic nonlinear term, due to its inherent complexity arising from the nonlinear term, the precise analytical solution has been conclusively demonstrated to be unattainable through mathematical approaches. Consequently, throughout the extensive research process, indirect solution methodologies have emerged as a prevailing consensus among scholars. In the theory of Nonlinear Dynamics, there are several methods to obtain analytics and numerical solutions. Some of the most well-known methods are the harmonic balance method, Petrov-Galerkin (P-G) method [34], Poincaré-Lindstedt (P-L) method [76, 77], and 4th order Runge-Kutta (4th R-K) method [78]. P-G and 4th R-K method are commonly used to obtain numerical solutions, where P-G is known ideal to solve differential equations with a symmetric system that contains odd order terms only and to convert the time domain form into the frequency domain form. The P-L method is to obtain uniformly approximating periodic solutions to the ordinary differential equation in a weak nonlinear system, within the perturbation theory. Harmonic balance is a common method to solve both linear and nonlinear problems when the equation consists of secular terms $t\sin(\omega t)$ [79, 80].

3.3.1. Steady-State Solutions for Linear Oscillators

As aforementioned, the nonlinearity is often natural and intrinsic. In many scenarios, oscillators are able to work within a linear or quasi-linear regime via certain designs and input control. To understand the behaviour of Si-NEMS resonators vibrating in linear regime, this subsection will introduce the approach to obtain analytic solution for the model illustrated in 3.2.

set nonlinear coefficient to zero to linearize the equation,

$$\omega_0^2 \beta_m - \beta_e = 0 \tag{3.23}$$

According to the Theory of Vibration by W. Thomson [81], if the system is driven by a sine wave, a dynamic of mechanical systems whose equation of motion have a general form as Equation (3.23) has its time dependent solution given by the Fourier Series form as,

$$z(t) = A_0(0) + \sum_{n=1} [A_n \cos(n\omega t) + B_n \sin(n\omega t)] \tag{3.24}$$

where $A_0(0)$ is the initial displacement of the oscillator. $A_n \cos(n\omega t)$ and $B_n \sin(n\omega t)$ are two orthogonal components of the vibration displacement. In my scenario, the shape of the resonator at rest is pure symmetric without deformation. Therefore, in the following expressions, $A_0(0)$ is set to zero. For the interest of non-zero initial position solutions, Sansa et al. has reported a potential method to enhance the piezoresistive transduction mechanism based on the asymmetry of the beam shape at rest which enables highly sensitive linear detection of the vibration of low-resistivity silicon beams without the need for exceptionally large piezoresistive coefficients [19, 21]. Meanwhile, in this study, the Fourier series form is truncated to the fundamental harmonic expression (n = 1) leading to a pure sine wave solution to approximate the real periodic solution, which is sufficient to further simulation and

fitting.

Hence, I have an approximated solution to the Duffing equation given by,

$$z(t) = A\cos(\omega t) + B\sin(\omega t) = |z|e^{i\omega t + \theta}, \qquad (3.25)$$

$$|z| = \sqrt{A^2 + B^2}, \qquad (3.26)$$

$$|\theta| = \arctan\left|\frac{B}{A}\right| \qquad (3.27)$$

where $|z|$ is the amplitude of the instantaneous vibration displacement, θ is the phase change of the vibration. In this section, the linear response is focused. Therefore, the coefficient of z^3 is manually set to zero and the system function is given as,

$$z'' + \frac{\omega_0}{Q}z' + \left[\omega_0^2 - \frac{\varepsilon_0 LW(V_{DC} + V_{AC})^2}{m_b g_0{}^3}\right]z = \frac{\varepsilon_0 LW(V_{DC} + V_{AC})^2}{2m_b g_0{}^2} \qquad (3.28)$$

Substituting z with Equation (3.25) and I have,

$$-A\omega^2 \cos(\omega t) - B\omega^2 \sin(\omega t) - \frac{\omega_0 \omega}{Q}[A\sin(\omega t) - B\cos(\omega t)] + \omega_0{}^2 A\cos(\omega t)$$

$$+\omega_0{}^2 B\sin(\omega t) - \frac{\varepsilon_0 LW V_{DC}{}^2}{m_b g_0{}^3}[A\cos(\omega t) + B\sin(\omega t)] - \frac{\varepsilon_0 LW V_{DC} V_{AC}\cos(\omega t)^2}{m_b g_0{}^3}A$$

$$-\frac{\varepsilon_0 LW V_{DC} V_{AC}\cos(\omega t)}{m_b g_0{}^3}B\sin(\omega t) - \frac{\varepsilon_0 LW V_{DC}{}^2}{m_b g_0{}^2} - \frac{\varepsilon_0 LW V_{DC} V_{AC}\cos(\omega t)}{2m_b g_0{}^2} = 0$$

$$(3.29)$$

Simplifying the Equation (3.29), extracting the coefficients around $sin(\omega t)$ and $cos(\omega t)$ and balancing them, a set of equations that relates to A, B, and ω are given as,

56

$$-\frac{\varepsilon_0 LWV_{DC}(V_{DC}+V_{AC})}{2m_b g_0{}^2} - \frac{\omega_0\omega}{Q}B + (\omega_0^2-\omega^2)A - \frac{\varepsilon_0 LWV_{DC}(V_{DC}+V_{AC})}{m_b g_0{}^3}A = 0$$

$$(\omega_0^2-\omega^2)B + \frac{\omega_0\omega}{Q}A - \frac{\varepsilon_0 LWV_{dc}(V_{dc}+V_{ac})}{m_b g_0{}^3}B = 0$$

$$(3.30)$$

The dimensional parameters L, W, g_0 are referred from Table 3.1. Effective mass m_b is given by Equation (3.22). The values of ε_0, V_{DC}, V_{AC} are given by the actual experiment condition. The solutions of A and B can be calculated from the equations above as the function of input frequency ω.

Another approach is by using the expression $ze^{i\omega t+\theta}$ and solve Equation (3.28) directly without using the harmonic balance. The advantage of this method is its simplicity by referring the Lorentzian function [82]. The drive mode vibration displacement is given as follow,

$$z(\omega) = \frac{\varepsilon_0 LW(V_{DC}+V_{AC})^2}{2m_b g_0{}^2 \sqrt{(\omega_0^2-\omega^2)^2 + \frac{\omega_0^2\omega^2}{Q^2}}} + z(0) \qquad (3.31)$$

$$|\theta| = arctan\left|\frac{\omega\omega_0}{Q(\omega_0^2-\omega^2)}\right| \qquad (3.32)$$

Regarding the displacement to current conversion, Gouttenoire et al. [29] reported their findings about the signal transduction mechanism in carbon nanotube (CNT) based NEMS resonator. Their result proved that in the frequency modulation (FM) method, for linear oscillator, the current detected by the lock-in amplifier at the frequency ω is linearly proportional the derivative of the real part of the displacement.

Only considering the real domain, the derivative of Equation (3.31) is given as,

$$X(\omega) = S_{iz} \frac{\varepsilon_0 LW (V_{DC} + V_{AC})^2}{2 m_b g_0^2} \frac{2\omega \left(\omega^2 - \omega_0^2 - \frac{\omega_0^2}{Q}\right)\left(\omega^2 - \omega_0^2 + \frac{\omega_0^2}{Q}\right)}{\left[(\omega_0^2 - \omega^2)^2 + \frac{\omega_0^2 \omega^2}{Q^2}\right]^2} + X(0) \ (3.33)$$

where $X(\omega)$ is the current frequency response, S_{iz} is the scaling factor that stands for the expression of 'linearly proportional' relationship based on the result from [29], and $X(0)$ is the offset current level.
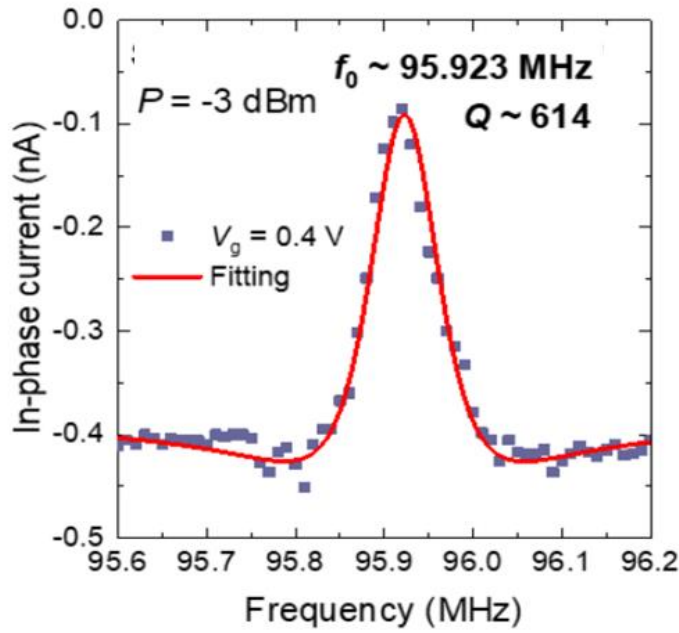
Figure 3.6 Linear curve fitting for a Si-NEMS resonator's frequency response by Tsuchiya et al [27].

Prior to this project, Tsuchiya et al [27] performed linear fitting for a 2 μm-long Si-NEMS resonators (Sample S1 as shown in Table 3.1). The linear model they have used in the publication is in the similar form as Equation (3.33). The improved part is Equation (3.33) that expresses dimensional parameters, effective mass, DC bias and AC amplitude more explicitly, which are directly linked with information provided from actual samples and experimental data.

3.3.2. Steady-State Solutions for Nonlinear Oscillator

Numerical approaches directly address the differential equations in models, relying heavily on computation to determine the standard nonlinear mode. Analytical methods, as seen earlier, have multiple drawbacks. Firstly, they can only be feasibly applied to straightforward systems with a limited number of degrees of freedom (DOF). Furthermore, these methods are heuristic, meaning the approximations derived from their use are solely valid for small DOF displacement magnitudes. All such techniques necessitate some level of computational aid for tasks like calculating power series coefficients or performing integrations, as demonstrated when using the harmonic balance method on various models. Conversely, numerical methods are scalable and highly compatible with large-scale or highly nonlinear systems, offering the potential for precise numerical solutions to the standard nonlinear mode. However, this advantage comes at the cost of demanding significant computational resources with the currently accessible methods.

At the beginning of section 3.3, several typical numerical or analytical methods to solve nonlinear functions have been introduced. In case for NEMS resonators, I have opted for Petrov-Galerkin (P-G) method which not only is capable to be used for both ordinary differential equation (ODE) and partial differential equation (PDE) scenarios, but also can directly transfer the test function into different domain. In this section, the nonlinear NEMS resonator model (Equation (3.23)) will be processed with P-G method and steady-state solutions for frequency response will be obtained as a result of P-G method combined with computational iterations.

Here we use the same test function for the displacement $z(t)$ as shown in Equation (3.25). The P-G method focuses on minimizing weighted residuals, in this case, the residual work. For a steady-state symmetric oscillation, the total residual work in each periodic oscillation cycle is balanced to be zero [83].

To begin with, I define the residual force $R(t)$ of the system as,

$$R(t) = m_b \left[z(t)'' + \frac{\omega_0}{Q} z(t)' + \left(\omega_0^2 - \frac{k_e}{m_b} \right) z(t) + \left(\omega_0^2 \beta_m - \frac{\beta_e}{m_b} \right) z(t)^3 \right] - F_{elec}^0$$

$$(3.34)$$

$R(t)$ is the time-dependent residual force. In my case, the oscillation is only driven by electrostatic force F_{elec}^0. The reason that harmonic balance is not used but P-G method is that $R(t)$ equals zero only if the oscillator reaches a certain equilibrium level of amplitude. So, the approximated solutions obtained via harmonic balance cannot precisely describe the scenario when the energy is released nonlinearly. The P-G method extends the consideration from a single instantaneous point to the whole cycle of oscillation by balancing the work of residual force leading to an acceptable approximation.

The residual work is a product of the residual force and the displacement, which is expressed as,

$$R(t)z(t) = R(t)A(\omega)\cos(\omega t) + R(t)B(\omega)\sin(\omega t) \qquad (3.35)$$

Here, the coefficients will be derived from the orthogonalization of residual force in the interval $(0, 2\pi/\omega)$ leading to a set of 2 algebraic equations that determine the values of amplitude coefficient $A(\omega)$ and $B(\omega)$ as a function of the parameter ω:

$$G_1(A, B, \omega) = \int_0^{\frac{2\pi}{\omega}} R(t)A(\omega)\cos(\omega t)dt = 0 \qquad (3.36)$$

$$G_2(A, B, \omega) = \int_0^{\frac{2\pi}{\omega}} R(t)B(\omega)\sin(\omega t)dt = 0 \qquad (3.37)$$

where $G_1(A, B, \omega)$ and $G_2(A, B, \omega)$ are two orthogonal Galerkin functions of the residual work per cycle, which are equal to zero. Substituting $R(t)$ in Equation (3.36)

and (3.37) by Equation (3.34), I have,

$$
\begin{aligned}
G_1(A, B, \omega) = AQ & \left[A^2 \beta_m \omega_0^2 + \left(B^2 \beta_m + \frac{4}{3} \right) \omega_0^2 - \frac{4\omega^2}{3} \right] m_b g_0^5 - \frac{4SV_{AC}V_{DC}g_0^3 \varepsilon_0 Q}{3} \\
& - \frac{8QASV_{DC}^2 g_0^3 \varepsilon_0}{3} - 4QA\varepsilon_0 SV_{DC}^2(A^2 + B^2) + \frac{4\omega_0 B\omega m_b g_0^5}{3}
\end{aligned}
$$

$$(3.38)$$

$$
\begin{aligned}
G_2(A, B, \omega) = QB^3 (\beta_m g_0^5 m_b \omega_0^2 - 4\varepsilon_0 SV_{DC}^2) & + \left[\left(A^2 \beta_m + \frac{4}{3} \right) \omega_0^2 - \frac{4\omega^2}{3} \right] QBm_b g_0^5 \\
& - \left(\frac{8g_0^2}{3} - 4A^2 \right) SV_{DC}^2 \varepsilon_0 QB - 4\omega_0 A\omega m_b g_0^5
\end{aligned}
$$

$$(3.39)$$

The resulting system is a set of two equations $G_1 = 0$ and $G_2 = 0$ with two dependent variables A and B with an independent variable ω.

Newton-Raphson iteration (NRI) [83] is one of the most commonly used mathematic method to approximate target solution. The advantage of using NRI is that it allows computational iteration with controlled steps where convergence and solutions can be tracked via iteration counts, which is simple to be realized in algorithm. I perform NRI via MATLAB 2020a [84], full code can be found in Appendix A.2. Here, we present details of NRI to solve Equation (3.38) and (3.39).

Given the NRI equations with respect to solutions $A(\omega)$ and $B(\omega)$ as,

$$[A_{N+1}(\omega) \ B_{N+1}(\omega)] = [A_N(\omega) \ B_N(\omega)] - \frac{\boldsymbol{G}}{\boldsymbol{J}} \qquad (3.40)$$

where $\boldsymbol{G}$ and $\boldsymbol{J}$ are the Galerkin matrix (G_1, G_2) and the Jacobian matrix of $\boldsymbol{G}$, respectively, given as,

$$J = \begin{pmatrix} \dfrac{\partial G_1}{\partial A}(A, B, \omega) & \dfrac{\partial G_1}{\partial B}(A, B, \omega) \\ \dfrac{\partial G_2}{\partial A}(A, B, \omega) & \dfrac{\partial G_2}{\partial B}(A, B, \omega) \end{pmatrix} \tag{3.41}$$

The derivatives in the Jacobian matrix are given as,

$$\frac{\partial G_1}{\partial A}(A, B, \omega) = \left[A^2 \beta_m \omega_0^2 + \left(B^2 \beta_m + \frac{4}{3} \right) \omega_0^2 - \frac{4\omega^2}{3} \right] m_b g_0^5 + 2\, A_2 \beta_m g_0^5 m_b \omega_0^2$$
$$- \frac{8 S g_0^2 V_{DC}^2 \varepsilon_0}{3} - 4\varepsilon_0 S V_{DC}^2 (A^2 + B^2) - 8 A^2 S V_{DC}^2 \varepsilon_0 \tag{3.42}$$

$$\frac{\partial G_1}{\partial B}(A, B, \omega) = (2AB\beta_m \omega_0^2 m_b g_0^5 - 8ABSV_{DC}^2 \varepsilon_0) Q + \frac{4 m_b g_0^5 \omega \omega_0}{3} \tag{3.43}$$

$$\frac{\partial G_2}{\partial A}(A, B, \omega) = (2AB\beta_m \omega_0^2 m_b g_0^5 - 8ABSV_{DC}^2 \varepsilon_0) Q - \frac{4 m_b g_0^5 \omega \omega_0}{3} \tag{3.44}$$

$$\frac{\partial G_2}{\partial B}(A, B, \omega) = 3(\beta_m g_0^5 m_b \omega_0^2 - 4\varepsilon_0 S V_{DC}^2) B^2 + \left[\left(A^2 \beta_m + \frac{4}{3} \right) \omega_0^2 - \frac{4\omega^2}{3} \right] m_b g_0^5$$
$$- 8 S g_0^2 V_{DC}^2 \varepsilon_0 \tag{3.45}$$

The result of trail simulation shows that iteration counts $N = 500$ is able to present enough precision for the steady-state solutions. A set of initial values are expected in NRI to converge to the steady-state approximation solutions. Here, we use $(5 \times 10^{-12}, 5 \times 10^{-12})$ as the initial values of (A_0, B_0).

3.3.3. Simulation

The section will demonstrate the simulations based on the previously derived model. Some parameters used during simulation are based on the actual samples as

aforementioned, such as dimensional parameters L, W, t, g_0 and silicon material properties ρ.

3.3.3.1. An Example in Linear Simulation

To begin with, we start from the simulation with linear model. Set the nonlinear part z^3 to zero, the model is then presenting pure linear response, which is equivalent to Eq. (3.33). Figure 3.7 shows the amplitude and phase change of simulated frequency response changing with respect to the actuation DC voltage.

From Equation (3.32), for a damped linear system, the value of Q and the frequency of the drive signal will affect the phase of the oscillation. Figure 3.7(b) shows the overall phase change at resonance is around 180°, where the phase shift of resonator is $\pi/2$ behind the phase of the drive signal. In Equation (3.30), the coefficient of z stands for the overall electro-mechanical stiffness, which is inversely proportional to V_{DC}^2. Table 3.2 summarises the simulation result for resonance frequency and simulated displacement and their changes with respect to the increase of DC bias.

Table 3.2 Simulation result of the steady-state linear oscillator

V_{DC} (V)	Resonance Frequency (MHz)	Displacement (nm)
1.0	97.95	13.56
1.2	97.93	16.45
1.4	97.91	19.19
1.6	97.88	21.89
1.8	97.84	24.69
2.0	97.81	27.48
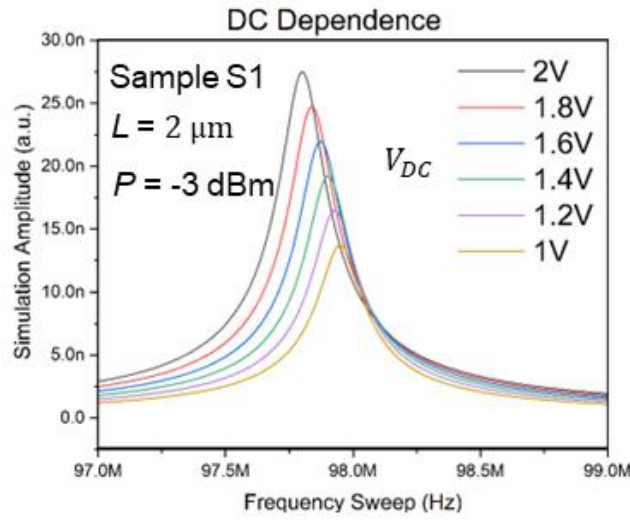
(a)
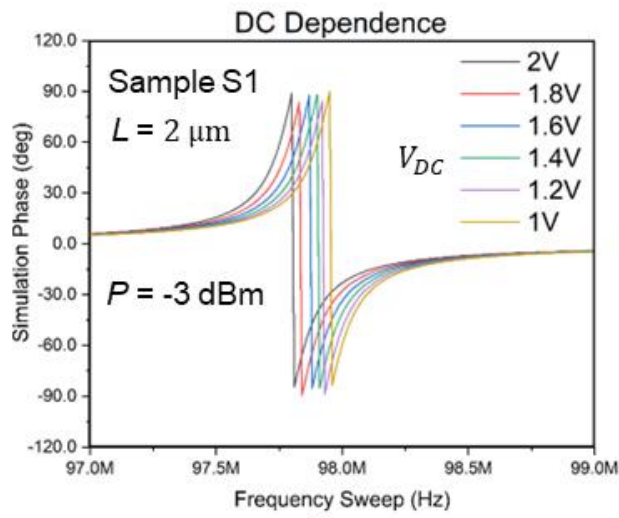
(b)

Figure 3.7 Steady-state linear oscillation simulation with respect to DC back-gate voltage dependence. (a)The simulated amplitude. (b)The simulated phase change

The result of simulation in Figure 3.7 demonstrated the details of how voltage changes not only displacement due to electrostatic force, but also the resonance frequency, or in other words, the stiffness of the oscillator via $\omega = \sqrt{k_{overall}/m_b}$ [46]. The symbol of $k_{overall}$ here is to distinguish it with the natural mechanical stiffness

64

which defines its natural pulsation. Due to the mechanism of resonance, the operation of heavily-doped beam needs to work under DC bias which means the resonance frequency showing in Table 3.2 will never be its intrinsic position. One possible way we have mentioned to identify its natural resonance position is by using Thermo-Mechanical Noise (TMN) measurement. Chapter 6 will go through our measurement and observation of TMN in detail.

3.3.3.2. Nonlinear Simulation: β_m

The method to obtain steady-state numerical solutions was in section 3.3.2. To present the effect by mechanical nonlinear coefficient β_m, numerical simulation result under Equation (3.40) will be carried out in this section. Table 3.3 summarises the resonance frequencies extracted from simulation.

Table 3.3 Simulation result of the steady-state nonlinear oscillator

$\beta_m(m^{-2})$	Resonance Frequency (MHz)
1×10^{-4}	98.05
5×10^{-4}	97.97
1×10^{-5}	97.96
5×10^{-5}	97.95
0	97.95
-1×10^{-5}	97.95
-5×10^{-5}	97.94
-1×10^{-4}	97.93
-5×10^{-4}	97.83
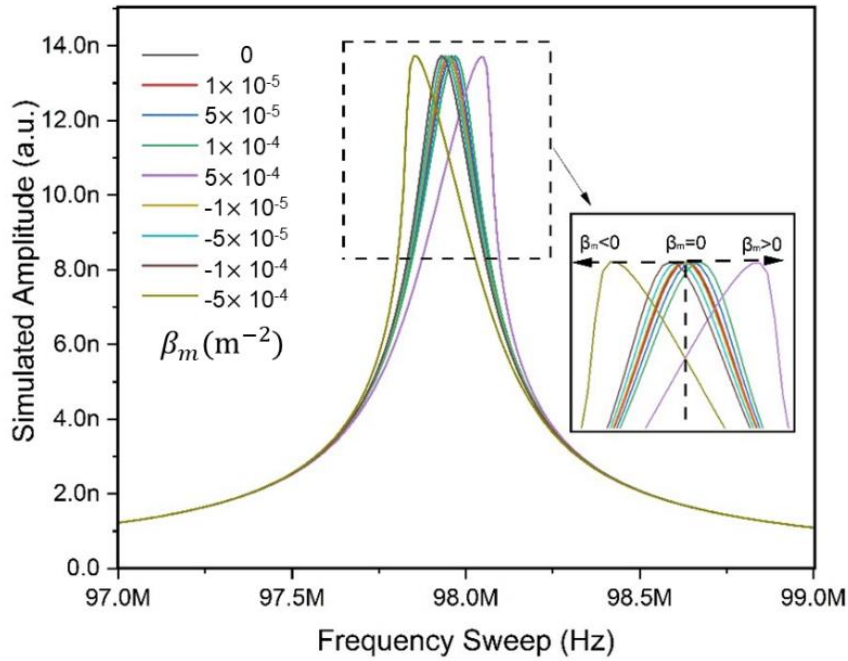
Figure 3.8 Steady-state linear oscillation simulation with respect to DC back-gate voltage dependence. (a)The simulated amplitude. (b)The simulated phase change

Figure 3.8 and Table 3.3 together present the effect by the mechanical nonlinear stiffness coefficient β_m with respect to the resonance frequency. Differ from the linear simulation, the impact of nonlinear coefficient on the resonance frequency response is primarily concentrated on the shape of the curve, or specifically, its peak, rather than causing a parallel shift of the entire curve. The simulation result in Figure 3.8 is obtained under V_{DC} at 1 V and the power level at -3 dBm. It clearly demonstrates the impact by β_m. With the increase of value of $|\beta_m|$, the bending of curve becomes more pronounced.

Moreover, as can be seen from Figure 3.8, although the value of β_m from 0 to 5×10^{-4} m^{-2} keeps the same increment during the simulation, the impact on curve's bending degree is different where from 1×10^{-4} to 5×10^{-4} m^{-2} the degree of curve bending, or in other words, the nonlinearity, is significantly pronounced than before. This tendency is the same as in negative values. This proves the increase of mechanical

nonlinearity β_m can lead to an exponential growth in the system's nonlinear characteristics and it may dominate when its intrinsic properties, such as of a novel material MoS₂, is highly sensitive to nonlinear response. Conversely, with less mechanical nonlinearity, the system would be much easier to maintain its function in the linear regime.

3.3.3.3. Nonlinear Simulation: Voltage Dependence

One important novelty in this research is to explain the nonlinear voltage dependence. With the equivalent nonlinear electrical stiffness β_e, the change of voltage can lead to the impact on overall amount of nonlinearity $\beta_{overall}$, defined as,

$$\beta_{overall} = \beta_m \omega_0^2 - \beta_e \tag{3.46}$$

For a positive $\beta_{overall}$, the overall peak bends to the right side while in the case of negative $\beta_{overall}$, the peak bends to the left side. This is known as hardening nonlinearity and softening nonlinearity.
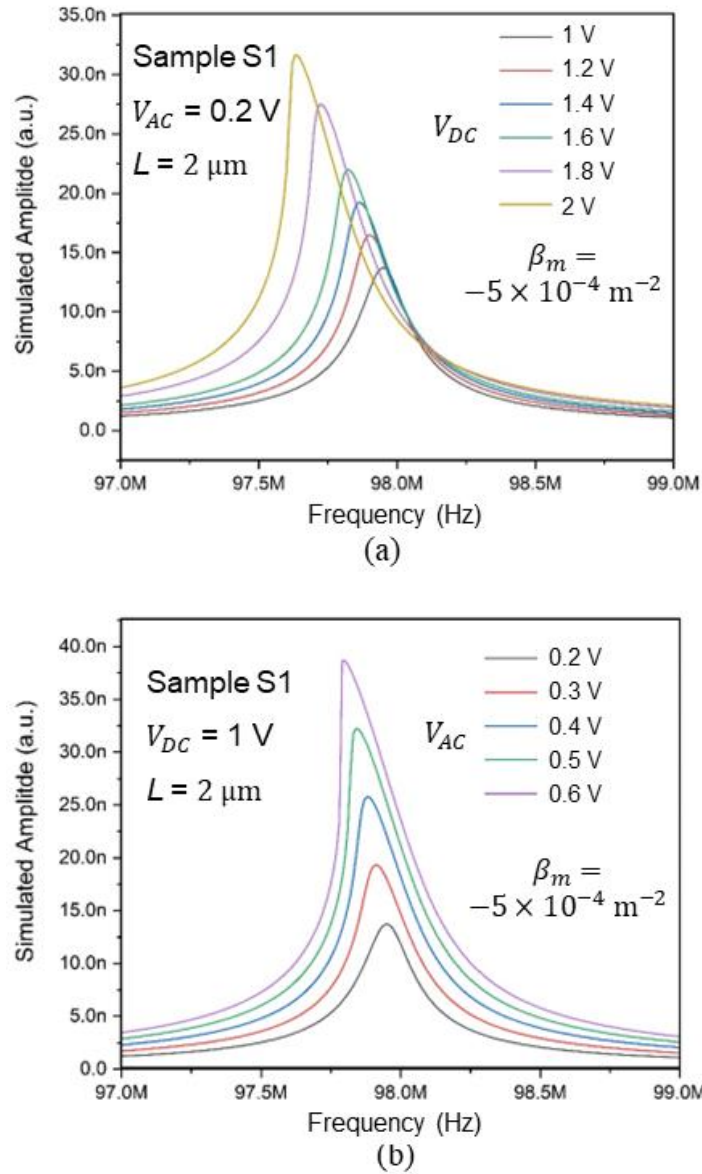
Figure 3.9 The steady-state solution of nonlinear oscillator simulation result. (a)Frequency response with respect to V_{DC} dependence. (b)Frequency response with respect to V_{AC} dependence

Figure 3.9 systematically shows how nonlinear behaviour changes with respect to the dependence of V_{DC} and V_{AC}. It can be observed that V_{DC} and V_{AC} are both capable to change the overall nonlinearity. The differences are that V_{DC} has better tunability regarding the position of the resonance peak, while V_{AC} affects more on the nonlinearity in the vicinity of a specific peak point. In terms of the V_{DC} effects, it is quadratically proportional to the linear and nonlinear electrical stiffness, k_e and β_e,

simultaneously. However, k_e is more sensitive to the change of V_{DC} than that with β_e.

Chapter 2 introduces the findings from Samanta el ta., group [39, 53] regarding the voltage tunability in MoS$_2$ 2D-NEMS devices. First, they demonstrated results that DC bias influences nonlinearity. The potential mechanism about how the nonlinear behavior of MoS$_2$ 2D-NEMS can be tuned from hardening to linear and softening under DC bias has been explained in Chapter 2 accordingly. Within the electrostatic-dominant nonlinearity regime, DC bias typically induces softening nonlinear effect and can also effectuate a shift in mechanical resonance, as depicted in Figure 3.9(a). Additionally, regarding the impact of AC dependences, Samanta et al. showed the classic Duffing nonlinear oscillation characteristics. More specifically, the peak point of the nonlinear curve shifts upward and to the left with the increase of AC, due to nonlinear softening as AC amplitude increases, resulting in a decrease in frequency and an increase in amplitude. Conversely, for nonlinear hardening, the shift would occur upward and to the right. Furthermore, with increasing AC amplitude, the curve's bandwidth expands while the mechanical resonance remains nearly stationary. This leads to the situation where the enlarged nonlinear curve envelopes the original curve, a phenomenon depicted in figure 3.9(b).

Displacement z is less comparable to gap g_0 in my case, as shown in Table 3.2, the g_0^5 in the denominator of β_e is significantly small and therefore, have less effect on the calculation compared to the g_0^3 in the denominator of k_e. Hence, mathematically, when increasing V_{DC}, the change of linear electrical stiffness k_e will be significantly larger than the change in β_e, leading to a more distinct effect on shifting the curve. Meanwhile, in the simulation, the value and interval of V_{DC} are also larger than those of V_{AC}, making the resonance peak more sensitive to V_{DC} rather than V_{AC}. This conclusion is significant that it offers insightful idea regarding the difference of the effect by parameters, which would be very helpful in the fitting.

3.3.3.4. Nonlinear Simulation: Hysteresis

For a nonlinear dynamic system, another significant characteristic needed to be discussed is the bifurcation, which has been aforementioned. In perturbation theory [79], it mentioned that a small perturbation on the system, while the motion is at an extreme state (e.g., state at maximum or minimum amplitude) would bring the system back to the same state of motion. However, a small perturbation from the regime of intermediate state would force the system out of that state only to converge to one of the two stable solutions. For any other driving frequency out of that interval, the steady-state solution is unique and stable, leading to a final phenomenon shown in Figure 3.9.

For a system shown in Equation (3.21) with a cubic nonlinear term that follows the form as $\beta x^3 - kx$, besides two stead-state stable solutions obtained by Equation (3.40), up to three solutions will be presenting, depending on the value of nonlinear coefficient β. A mathematic explanation can be seen in Figure 3.10. Consider that solutions for $\beta x^3 - kx = 0$ are x_1, x_2, x_3, as aforementioned, the maximum and minimum solutions x_1 and x_3 (or vice versa) are two stable solutions. When β changes, those solutions will change correspondingly. The multi-solution phenomena are natural in mathematics and in physical definition, it calls bifurcation and hysteresis from the perspective of behaviour.
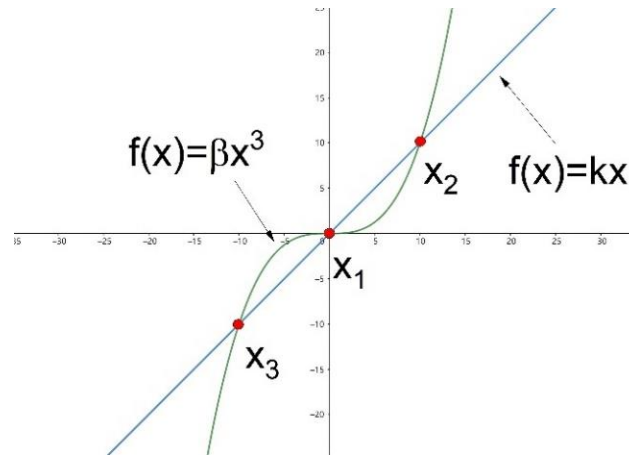
Figure 3.10 A mathematic explanation of multi-solutions in cubic nonlinear system $\beta x^3 - kx$.

Noted that in extreme scenario, due to the domination of instability, it will eventually lead to chaotic behaviour, such as three-body problem in astronomy field. The reason to discuss the hysteresis behaviour is its potential in the use of neuromorphic computing which requires the resonator to work in strong nonlinear regime in order to utilise its bi-stability. Hence, a thorough understanding about the onset point of the hysteresis and its model for characterization are significant.

Surprisingly, the model that derived previously can effectively simulate the bistable hysteresis effect, as shown in Figure 3.11. Model can demonstrate both the hysteresis behaviour based on softening nonlinear effect shown in Figure 3.11(a) and the hysteresis behaviour based on hardening nonlinear effect shown in Figure 3.11(b). This is due in part to my use of perturbation expansion and discussion of high-order electrostatic force responses at the microscale, which allows me to control the nonlinearity through different parameters, as well as employing numerical analysis, which is more accurate than analytic solutions under the scenario of given conditions. On the other hand, the NRI possesses the ability to give multiple solutions. Therefore, the combination of these two factors enables me to easily obtain the hysteresis behaviour and to control its mechanical nonlinearity or electrical nonlinearity in the same way as before.

(a)

(b)
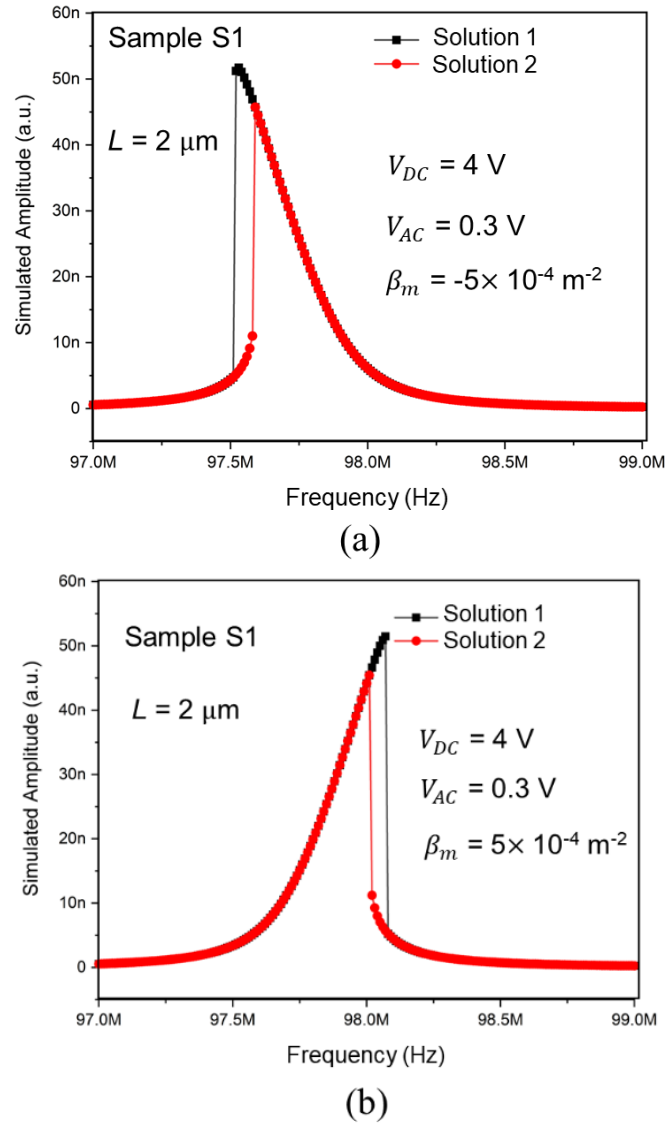
Figure 3.11 Simulation Result showing hysteresis phenomena. Input conditions are set as V_{DC}=4 V, V_{AC}=0.3 V (a) A softening hysteresis with β_m at -5×10^{-4}. (b) A hardening hysteresis with β_m at 5×10^{-4}

Hereby, a brief discussion about the prediction of the onset point of the hysteresis is addressed. For the nature of nonlinearity, the multiple solutions are always existing in a nonlinear system which is intrinsic property. However, in many cases, the multi-resonance under the same experimental condition cannot be seen. This was once explained by Andres et al. that in frequency response, only if the resonance bends due to the nonlinearity exceed the bandwidth, hysteresis, or in other words, multiple

solutions can be observed. This means, to identify the onset point of hysteresis, the shift of the resonance due to nonlinearity shall be defined first, and then the bandwidth can be used to find the threshold of the bending range of resonance because of nonlinearity.

For the convenience, I temporarily re-marked the stiffness as k_l and k_{nl} for the linear and nonlinear part of stiffness, respectively. I have,

$$k_{overall}z = k_l z + k_{nl}z^3 \tag{3.47}$$

Then, the shift of resonance due to nonlinearity can be derived by,

$$(k_{overall} - k_l)z = k_{nl}z^3 \tag{3.48}$$

Normalizing Equation (3.48) by the mass and displacement z, I have,

$$(\omega_{ova}^2 - \omega_l^2) = k_{nl}z^2 \implies (\omega_{ova} + \omega_l)(\omega_{ova} - \omega_l) = k_{nl}z^2 \tag{3.49}$$

where ω_{ova} and ω_l are the angular resonance frequency in overall form and its linear portion. The term $\Delta\omega = \omega_{ova} - \omega_l$ is the shift of resonance due to the presence of nonlinearity. As $\omega_l \gg \Delta\omega$, Equation (3.49) can be approximated as,

$$|\Delta\omega| = \frac{k_{nl}z^2}{2\omega_l} \tag{3.50}$$

Considering the case that the shift of resonance $\Delta\omega$ surpasses the bandwidth, I have,

$$\left|\frac{k_{nl}z^2}{2\omega_l}\right| > \frac{\omega_l}{Q} \tag{3.51}$$

For a system that has softening nonlinear effect ($k_{nl} < 0$), by substituting the parameters,

$$k_{nl} = (\beta_m \omega_0^2 - \beta_e) < -\frac{2\omega_0^2}{Qz^2} \tag{3.52}$$

$$\beta_e > \beta_m \omega_0^2 + \frac{2\omega_0^2}{Qz^2} \tag{3.53}$$

Using the mathematic definition (in Equation (3.20)) of β_e, I have,

$$(V_{DC} + V_{AC})^2 \geq (\beta_m \omega_0^2 + \frac{2\omega_0^2}{Qz^2}) \frac{m_b g_0{}^5}{2\varepsilon_0 LW} \tag{3.54}$$

The right-hand side of Equation (3.54) can be used to calculate the threshold point of the onset of hysteresis. When the input value on the left-hand side surpasses the threshold point, multiple solutions given by the model will be used to fulfil the hysteresis fitting in the later chapter.

3.4. Model Fitting

Based on the actual device dimensions and experimental conditions, the model we have derived can simulate the displacement frequency response under certain given conditions. However, some parameters cannot be directly obtained without experimental data, such as resonance frequency ω_0, quality factor Q, and β_m (pre-set values were used in previous sections).

A similar situation occurs extensively in the semiconductor manufacturing industry. Before being officially delivered to fabless companies, many tape-out test wafers and devices are sent directly to the prober station for electrical and noise tests. Then,

modelling software (such as the previously mentioned BSIM) is used to model various characteristics, and by continuously adjusting some characteristic parameters (e.g., $swing_{sat}$, $swing_{lin}$, DIBL, C_{ox}, I_{dlin}, etc.) and fitting the test data, the parameters in the fitted model are extracted to present the corresponding sample.

Therefore, since Si-NEMS resonator samples have been already fabricated, we can obtain parameters that cannot be directly obtained from the tests, especially β_m, through model fitting. Although, model fitting and parameters extraction are not directly related to any novelty, they have been the major works which have taken most of time in this research project and the values extracted from the fitting are significant to the characterization to quantitatively understand nonlinear frequency response. A brief introduction regarding model fitting strategy will be given in this subsection.

For better understanding, a flowchart to show the process of model fitting is presented in Figure 3.12. In general, the target of model fitting is to extract a set of parameters including resonance frequency ω_0, quality factor Q and β_m. Because ω_0 and β_m are derived from the mechanical stiffness K as described in 3.2.2, theoretically, they are intrinsic parameters where they should not change under any experimental input. Meanwhile, room temperatures and vacuum condition are set for all the experiment, hence, the quality factor Q is also considered as a constant regardless of input. Therefore, ideally a set of ω_0, Q, β_m together with given parameters (L, W, t, g_0, m_b) should be able to fit any experimental data with respect to the DC and AC dependence.

In this case, once I found a success of model fitting under the above criteria, we can assume that the parameters, especially the mechanical nonlinear coefficient β_m, are the correct value to describe the physics for the corresponding sample. And they can be utilized for simulations and data analysis.
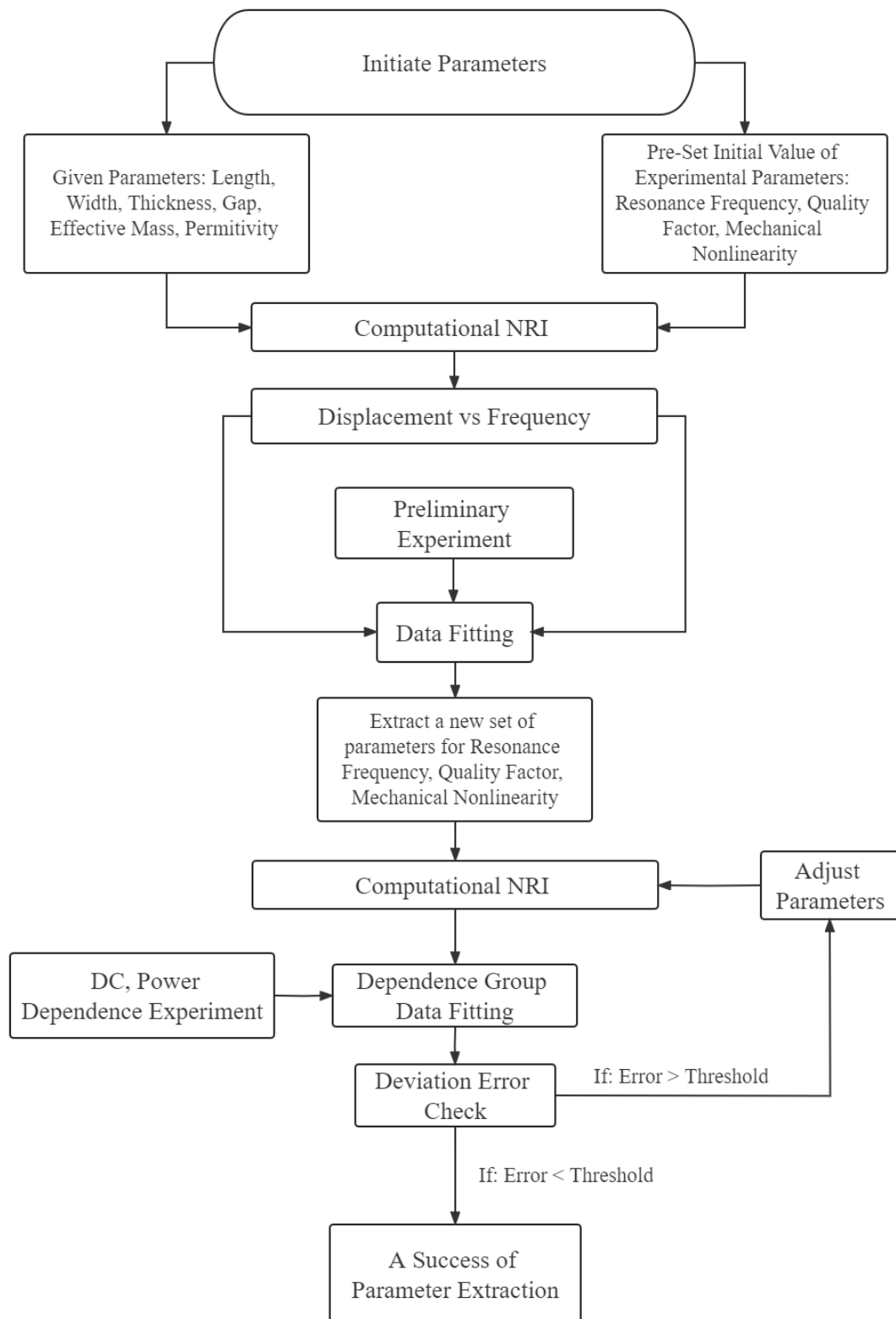
Figure 3.12 A flowchart to show the process of model fitting. NRI stands for Newton-Raphson Iteration computed by MATLAB 2020a.

A key to ensure the accuracy is by introducing error check, which is the deviation error check step before the last parameter extraction. The error check function used in the fitting algorithm is call the Relative Root Mean Square Error (RRMSE), which is capable to evaluate the difference of each simulated numerical data to the corresponding experimental data, presenting as the fitting error. RRMSE is defined as,

$$RRMSE = \frac{\sqrt{\frac{1}{n}\sum_{i=1}^{n}\left(\bar{H}_{exp}^{i} - \bar{H}_{model}^{i}\right)^2}}{\sum_{i=1}^{n}\bar{H}_{exp}^{i}} \times 100\% \qquad (3.55)$$

where $\bar{H}_{exp}^{i}$ and $\bar{H}_{model}^{i}$ are the i-th point of experimental data and model simulation data, respectively. Compared with a common error parameter such as the root mean square error (RMSE), RRMSE is more versatile to apply for comparison between different discrete set of data as the value of error is further normalized by the $\bar{H}_{exp}^{i}$, making it comparable to different set of data regardless of experimental techniques. So, the fitting result by justifying with respect to RRMSE can be used to cross-compare with data obtained by different measurement and input conditions.

The use of deviation error check is essential as it not only stands the criteria to the fitting quality, but also tells how far the simulation result is from the experimental data, which helps the parameter adjustment. Figure 3.13 is an example of screenshot from MATLAB to show how RRMSE is used to find the best fitting point with respect to β_m.

The change of β_m will result in the change in RRMSE. Hence, a set of β_m can be employed to generate multiple simulation results, and the best fitting point can be easily identified once it is in the minimum point.
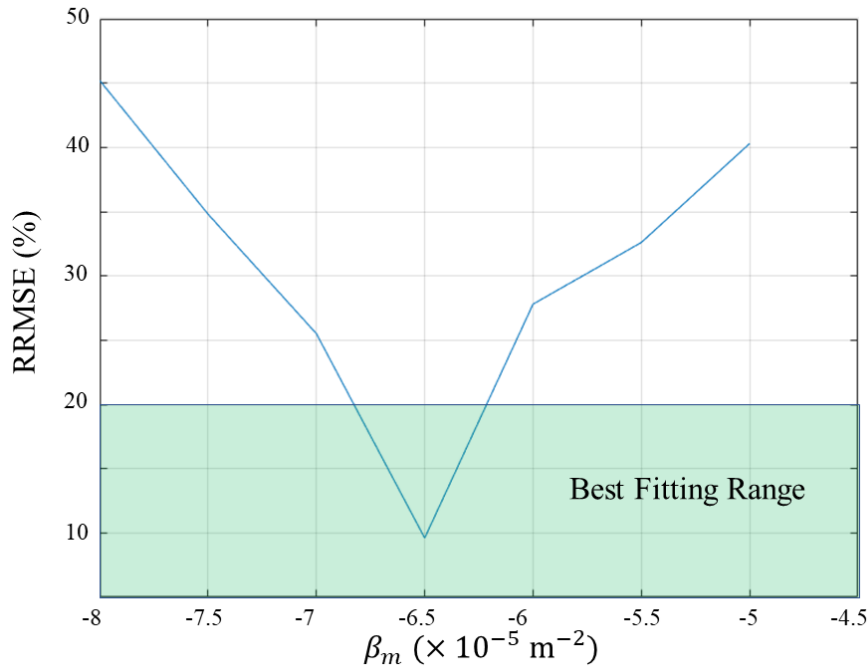
Figure 3.13 RRMSE result with respect to the β_m

We employ the RRMSE criterion proposed by Milan et al., [85]. When RRMSE less than 10%, fitting is considered as excellent, when RRMSE is between 10% to 20%, fitting is good, when it in the range from 20% to 30% fitting is fair, and when RRMSE is larger than 30%, fitting is poor, or failed. The reason to introduce the criterion is that, although in linear fitting, the error could be very small with less than 1%, however, in many cases of nonlinear fitting, due to the inaccuracy from the approximation of simulation and the rapid change in the resonance peak, a perfect fitting cannot be guaranteed. The above illustrated criterion is applied in my model to justify the quality of fitting.

3.5. Summary

In summary, this Chapter presents a detailed methodology for modelling and analysing Si-NEMS resonators. At the beginning of the chapter, a brief introduction to

the fabrication process of Si-NEMS resonators is provided. This part not only explores the materials and processes of Si-NEMS resonator, but also allows for an understanding of its structural characteristics. Next, starting from the Duffing model, I introduce the modelling and description process with respect to different origins of nonlinearity, with a primary focus on mechanical and electrical nonlinearity. For mechanical nonlinearity, its origin is discussed based on the perturbation expansion of mechanical stiffness, and the higher-order terms are extracted to obtain the nonlinear part of the system β_m. For electrical nonlinearity, based on the working principle of Si-NEMS resonators, a higher-order Maclaurin series expansion of the electrostatic force is performed. Then, the third-order term from its series is extracted to obtain the complete expression of the voltage-dependent nonlinear coefficient β_e. The superposition of β_m and β_e defines the overall nonlinearity of the system. Following that, I employed the Petrov-Galerkin (P-G) method for numerical analysis for the time-domain nonlinear equations and utilized the Newton-Raphson iteration to solve for the steady-state solution in the frequency domain. This process primarily involved symbolic computation using Maple 2020 and iteration with MATLAB 2020a. Based on this, I applied a pre-defined model for simulation and successfully demonstrated the influence of β_m, DC, and AC on linear and nonlinear frequency responses. Lastly, I introduced the detailed process of model fitting and illustrated it with flowcharts for ease of understanding. This process occupied a significant proportion of the entire project, not only because Nonlinear Regression Iteration (NRI) and parameter tuning were time-consuming but also because reasonable model fitting could yield more accurate parameter extraction and feature analysis, facilitating the continuation of this research topic and future applications based on nonlinear Si-NEMS resonators.

CHAPTER 4

Experimental Result with FM Measurement

In previous chapters, a comprehensive introduction to the theoretical and application background of nanoelectromechanical systems (NEMS) has been provided. Chapter 3 primarily focused on modelling results characterized by displacement frequency responses. However, due to the limitations in detecting displacement at ultra-small scales and within the very-high-frequency (VHF) range, experimental approaches primarily involve the detection of electrical or optical signals. This chapter will discuss the nonlinear DC, power dependence, and hysteretic behaviour of Si-NEMS resonators using frequency modulation (FM) testing methods. Firstly, the scheme of the FM setup based on Lock-in detection will be described, followed by an explanation of the conversion mechanism from displacement to current, founded on the operational principles of Si-NEMS. Subsequently, three different sizes of Si-NEMS devices (with lengths $L = 2$, 1.5, and 1 μm) will be employed for FM measurements and analysed using previously developed models to compare their nonlinear characteristics.

4.1. Introduction to FM and Lock-in Amplifier

4.1.1. Lock-in Amplifier

Lock-in amplifier is a widely used equipment to detect and measure ultrasmall AC signals even if the signal is obscured by the noise. It uses a phase-sensitive detection technique to separate the input signal at a specific reference frequency and phase from the noise signals at frequencies other than the reference frequency. Figure 4.1 schematically shows a lock-in amplifier, including an AC signal amplifier, a voltage-controlled oscillator (VCO) that synchronizes with an external reference signal, a multiplier called the phase-sensitive detector (PSD), a low-pass filter and a DC amplifier [86].
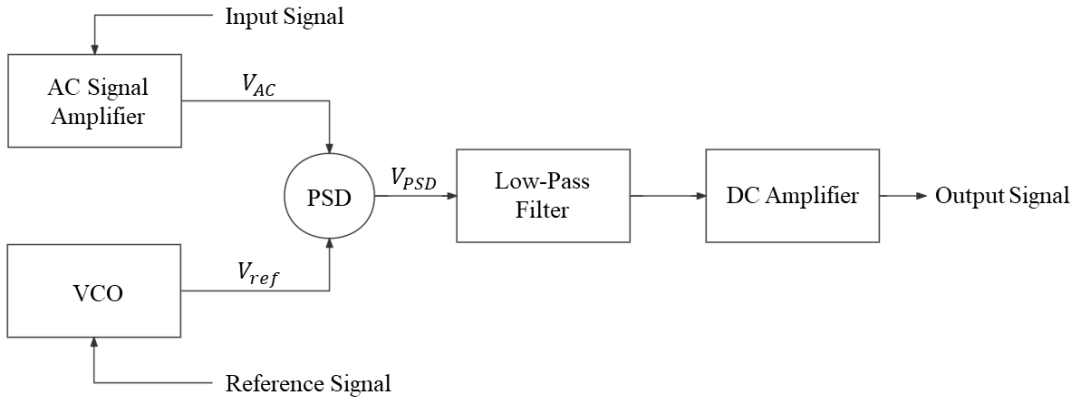
Figure 4.1 A diagram shows the details of a lock-in amplifier [86].

Consider the AC signal possesses the form as $V_{ac}(t) = G_{ac}V_i \sin(\omega t + \phi)$, where V_i is the input signal amplitude, G_{ac} is the gain of AC signal amplifier, and the internal reference signal locked to the external reference signal is $V_{ref}(t) = V_L \sin(\omega_l t + \phi_L)$, where V_L is the reference signal amplitude, ω_L and ϕ_L are the frequency and phase of the signal, the PSD output is given by,

$$
\begin{aligned}
V_{PSD} = {} & \frac{1}{2} G_{ac} V_i V_L \cos[(\omega - \omega_L)t + (\phi - \phi_L)] \\
& - \frac{1}{2} G_{ac} V_i V_L \cos[(\omega + \omega_L)t + (\phi + \phi_L)]
\end{aligned} \tag{4.1}
$$

At the point of $\omega = \omega_L$, the DC output voltage that is proportional to the amplitude of the input signal is therefore given by,

$$V_{output} = \frac{1}{2} G_{dc} G_{ac} V_i V_L \cos(\phi - \phi_L) \qquad (4.2)$$

where G_{dc} is the gain of the DC amplifier [25, 26, 86]. During the testing process, the phase of the reference signal is pre-defined. The SR830 lock-in amplifier detects the phase difference by comparing the original AC signal to an internal reference signal through mixing (PSD), low-pass filter. Thus, according to Equation (4.2), the phase of the original signal can be determined by extracting the phase of the output signal from the reference signal. Practically, it is a common practice to set the phase of the reference signal as the default value of 0. Therefore, the output signal is in phase with the input signal. Alternatively, the original phase can be obtained by adjusting the reference phase until the amplitude of output signal is maximised.

4.1.2. FM detection and Signal Conversion

Figure 4.2 shows the setup of FM detection to obtain out-of-plane resonance of NEMS beams via lock-in. The RF driving signal is generated by Rohde & Schwartz SMJ100A signal generator and modulated by reference frequency at 2 kHz from SRS SR830 lock-in amplifier. DC bias is applied via Agilent B1500 onto back gate to activate mechanical oscillation. Then the enhanced current at the resonance frequency is detected by the lock-in amplifier.
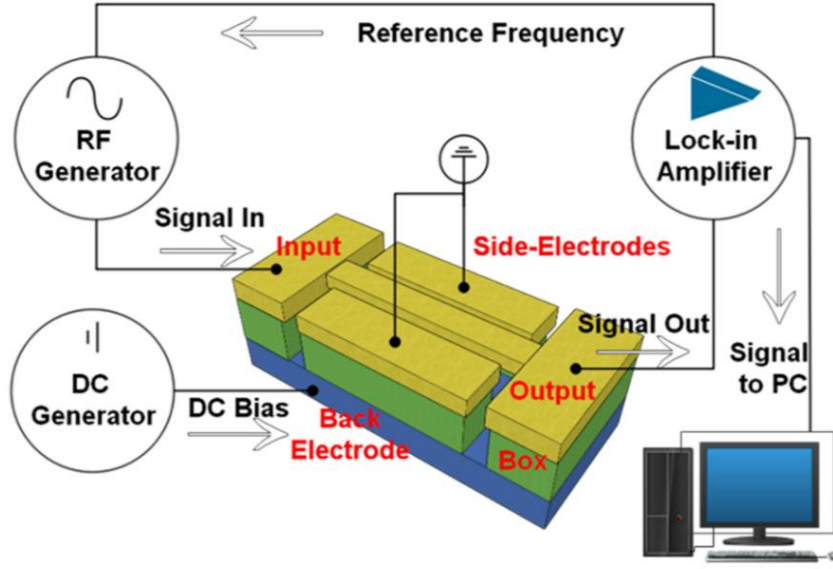
Figure 4.2 Diagram that schematically shows the resonance measurement set up by using FM detection method. Notably, this report only studied the back-gate voltage-dependence so side-gates are temporarily grounded.

The output current I, is determined by three parameters, including the signal applied to nanobeam $V_{AC,FM}$, the actuation voltage V_{DC}, the displacement of the beam perpendicular to the substrate $z_0 + \delta z(t)$. The voltage applied to the nanobeam by the frequency modulation (FM) method can be written as,

$$V_{AC,FM}(t) = V_{AC} \cos\left[\omega_c t + \frac{\omega_\Delta}{\omega_L} \cos(\omega_L t)\right] \qquad (4.3)$$

where ω_c is the high-frequency carrier component, which acts as the excitation frequency of the nanowire; ω_L is the low readout frequency, which is the reference frequency as previously mentioned, and ω_Δ is the frequency deviation.

Here, further analysis is undertaken by employing Taylor expansion on current I around boundary point $V_{AC}(0) = 0$, $z = z_0$. This approach enables the derivation of partial derivatives of I with respect to each parameter. This is demonstrated in the following equation as [29],

$$I(V_{DC}, z_0 + \delta z(t), V_{AC}) = I(V_{DC}, z_0, 0) + \frac{\partial I}{\partial V_{AC}}(V_{DC}, z_0, 0)V_{AC}$$

$$+ \frac{\partial I}{\partial z}(V_{DC}, z_0, 0)\delta z + I_2 \qquad (4.4)$$

where I_2 is the high-order terms in the Taylor expansion responsible for the low frequency signals that can be detected by the lock-in. The first and third terms on the right-hand side represent the components at $V_{AC} = 0$. In this scenario, because no signal passes through the beam, these terms are negligible in subsequent analysis. Regarding the second term, Gouttenoire et al. stated that it only arises with high-frequency signals and not in proximity to the reference signal frequency [29]. This also shapes the reason that the experiment selects a reference signal frequency significantly lower than the test frequency. Additionally, $\partial I/\partial V_{AC}$ represents the nanobeam transconductance, and for a fixed input state, the amplitude of V_{AC} remains constant. Therefore, when focusing on current variation, the second term in Equation (4.4) is disregarded. Hence, I proceed to further approximate the remaining component I_2, I have,

$$I_2 \approx \frac{1}{2}\frac{\partial^2 I}{\partial V_{AC}^2}V_{AC}^2(t) + \frac{\partial^2 I}{\partial z \partial V_{AC}}V_{AC}\delta z(t) + \frac{1}{2}\frac{\partial^2 I}{\partial z^2}\delta z^2(t) \qquad (4.5)$$

where $\delta z^2(t)$ can be ignored due to small magnitude. Daxwanger et al., [87] proved that the square of the applied signal $V_{AC}(t)$ in Equation (4.4) has no signal at the modulation frequency ω_L by giving a Jacobi-Anger expansion of the applied signal $V_{AC}(t)$ giving by Equation (4.3). Their findings further have been double checked by Gouttenoire et al., [29] who demonstrated the fact that it cannot demodulate the FM signal. Therefore, the only left term, $V_{AC}\delta z(t)\partial^2 I/\partial z \partial V_{AC}$ is a function of $\delta z(t)$, which can be deduced to express the relationship between current and displacement. The instantaneous displacement of the beam is,

$$\delta z(t) = Re[\delta z(\omega)]\cos[\omega t + \phi(t)] - Im[\delta z(\omega)][\omega t + \phi(t)] \qquad (4.6)$$

Substitute this to equation (23), I have,

$$I_{Lock-in}^{FM} = \frac{1}{2} \frac{\partial^2 I}{\partial z \partial V_{ac}} V_{AC} Re[\delta z(\omega)] \tag{4.7}$$

Where $Re[\delta z(\omega)]$ is the real part of $\delta z(\omega)$, which can be written in Taylor expansion when $\omega_\Delta \ll \omega_c$,

$$\omega = \omega_c + \omega_\Delta \cos(\omega_L t) \tag{4.8}$$

$$Re[\delta z(\omega)] = Re[\delta z(\omega_c)] + \frac{\partial Re[\delta z(\omega)]}{\partial \omega} \omega_\Delta \cos(\omega_L t)$$
$$+ \frac{1}{2} \left\{ \frac{\partial Re[\delta z(\omega)]}{\partial \omega} \omega_\Delta \cos(\omega_L t) \right\}^2 + z_h \tag{4.9}$$

where z_h is the sum of high order terms. The lock-in amplitude detects the signal at frequency ω_L. Therefore, lock-in current can be re-written by combining Equations (4.7) to (4.9), showing as,

$$I_{Lock-in}^{FM} = \frac{1}{2} \frac{\partial^2 I}{\partial z \partial V_{AC}} V_{AC} \frac{\partial Re[\delta z(\omega)]}{\partial \omega} \omega_\Delta \cos(\omega_L t) \tag{4.10}$$

Equation (4.10) has been the basis of the lock-in FM conversion in research [29]. As mentioned in chapter 3, the derivative of the real-part of displacement with respect to the frequency is proportional to the lock-in FM current. However, this theory was once only considered to be valid within linear regime due to the presence of $\partial^2 I / \partial z \partial V_{AC}$. To apply FM detection onto the nonlinear analysis, hereby, we performed further derivation onto equation (4.10) and expand its usage in nonlinear regime. To derive the details of Equation (4.10), here, we re-write the term $\partial^2 I / \partial z \partial V_{AC}$ as the space derivative of conductance G,

$$\frac{\partial^2 I}{\partial z \partial V_{AC}} = \frac{\partial}{\partial z} \frac{\partial I}{\partial V_{AC}} = \frac{\partial G}{\partial z} \tag{4.11}$$

To begin with, we consider the expression of capacitance C and perform the Maclaurin series for capacitance C near $z = 0$,

85

$$C = \frac{\varepsilon_0 LW}{g_0 - z} = \frac{\varepsilon_0 LW}{g_0}\left(1 + \frac{z}{g_0} + \frac{z^2}{g_0^2} + \cdots\right) \tag{4.12}$$

Consider the displacement z to the derivative of C in Equation (4.11),

$$\frac{\partial C}{\partial z} = \frac{\varepsilon_0 LW}{g_0^2}\left(1 + 2\frac{z}{g_0} + 3\frac{z^2}{g_0^2} \cdots\right) \tag{4.13}$$

Regarding the ∂G, I have,

$$J_e = \frac{I}{Wt} \tag{4.14}$$

where J_e is the current density (electron), Wt is the cross-sectional area. J_e can also be expressed by the electron mobility μ_e,

$$J_e = en_e\mu_e E \tag{4.15}$$

where e is single electron charge, n_e is electron concentration, E is the magnitude of electrical field V_{AC}/L .

$$J_e = \frac{I}{Wt} = en_e\mu_e \frac{V_{AC}}{L} \tag{4.16}$$

$$n_e = \frac{n_e(total)}{LWt} \tag{4.17}$$

$$en_e = \frac{Q}{LWt} \tag{4.18}$$

where Q is total charge, LWt is the volume of beam. Because the conductance G is I/V_{AC}, Equation (4.16) shows the expression that,

$$I = Wt\frac{en_e\mu_e V_{AC}}{L} \tag{4.19}$$

$$G = en_e\mu_e \frac{Wt}{L} \tag{4.20}$$

Substituting en_e by Equation (4.18), conductance G can be re-written as,

$$G = \frac{Q\mu_e}{L^2} \tag{4.21}$$

$$\partial G = \frac{\mu_e}{L^2}\partial Q = \frac{\mu_e}{L^2}\partial(CV_{DC}) = \frac{\mu_e}{L^2}(\partial CV_{DC} + C\partial V_{DC}) \tag{4.22}$$

In FM detection, the DC bias remains constants, $\partial V_{DC} = 0$, therefore,

$$\frac{\partial G}{\partial C} = \frac{\mu_e}{L^2}V_{DC} \tag{4.23}$$

Hence, Equation (4.11) is written as,

$$\frac{\partial^2 I}{\partial z \partial V_{AC}} = \frac{\partial G}{\partial z} = \frac{\partial G}{\partial C}\frac{\partial C}{\partial z} = \frac{\varepsilon_0 S\mu_e}{L^2 g_0^2}V_{DC} \tag{4.24}$$

The lock-in current for FM detection $I_{Lock-in}^{FM}$ in Equation (4.7) can be rewritten as,

$$I_{Lock-in}^{FM} = \frac{1}{2}\frac{\varepsilon_0 S\mu_e}{L^2 g_0^2}V_{DC}V_{AC}\frac{\partial Re[\delta z(\omega)]}{\partial \omega}\omega_\Delta cos(\omega_L t) \tag{4.25}$$

with the steady-state solutions of displacement in frequency-domain calculated by the aforementioned model, the FM lock-in current can be derived by using Equation (4.25) and fitted to experimental data.

It is worth noting that, in the early stage of this project, the conversion mechanism (from Equation (4.11) to (4.25)) were not clarified where a conversion factor S_{iz} to convert FM detected current into displacement was used for model fitting. The results were published on the IEEE MEMS international conferences where successful fitting with the use of S_{iz} has been achieved. The crucial finding regarding S_{iz} is that the value of S_{iz} is proportional with respect to V_{DC} and V_{AC}, as shown in Figure 4.3.
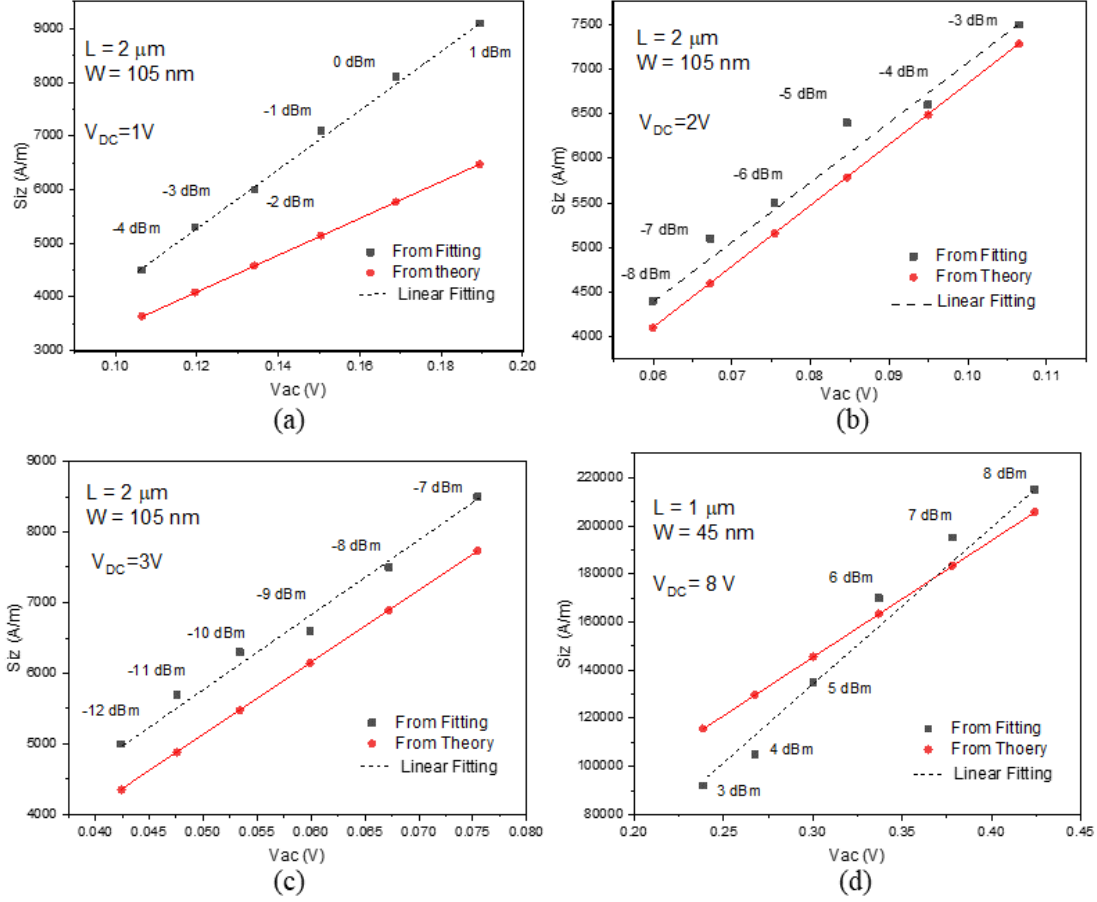
Figure 4.3 A investigation of displacement to current conversion factor S_{iz} regarding the V_{AC} dependence for sample S1 with V_{DC} at (a) 1 V, (b) 2V, (c) 3V and (d) for sample S5 with V_{DC} at 8 V

The black dots stand for the actual value of S_{iz} used for model fitting. As shown in all the figures, the general trend presents clear linearity regarding its V_{AC} dependence. Even for a shorter sample (Figure 4.3(d)), the linear trend remains the same. However, engaging in this approach for precise model fitting, in actuality, poses a certain degree of risk because the physical meaning regarding the S_{iz} were unclear at that moment. Consequently, the theoretical derivation presented in this section addresses this uncertainty, allowing the model to align with experimental data more closely. As a result, Equation (4.26) gives the explicit physical explanation regarding S_{iz}, having,

$$|S_{iz}| = \left| \frac{1}{2} \frac{\varepsilon_0 S \mu_e}{L^2 g_0^2} V_{DC} V_{AC} \omega_\Delta \right| \tag{4.26}$$

88

It shows clear linear relationship between S_{iz} and V_{AC}. As a validation, the actual value for the relevant parameters in the equation are used to calculate the theoretic value of each S_{iz}, as the red dots shown in Figure 4.3. It not only demonstrates a linear relationship between S_{iz} and V_{AC}, but also the magnitudes and orders of S_{iz} values are nearly indistinguishable from those of used in the actual model fitting. Remarkably, the trends of S_{iz} derived from theoretical calculations (red), in Figures 4.3(b) and (c), are nearly parallel to those of S_{iz} employed in the actual fitting process (black), proving a success of the validation of S_{iz}.

4.2. Experiment Result and Data Fitting

In this section, the results present a systematic analysis of the nonlinear characteristics with the explicit consideration of the voltage-dependent coefficient β_e in the model. The experimental data is successfully fitted with model including an analysis of hysteresis behaviour.

As aforementioned in modelling section, the amount of nonlinearity of the system is determined by the value of $(\beta_m \omega_0^2 - \beta_e)z^3$ where β_e is explicitly the function of actuation voltage V_{DC} and driven signal V_{AC}. β_m is the mechanical stiffness that is only related to the intrinsic characteristics of the device itself such as material, design, doping concentration.

Hence, the β_m is considered as an unknown constant that can be extracted from the experimental data fitting regardless of input voltage. Figure 4.4 shows the model (red line) is well aligned with the experimental data (dots) from linear region (Figure 4.4(a)) to nonlinear region (Figure 4.4(b)) by only increasing the RF power from -9 dBm to -4 dBm with the length, width, temperature, chamber pressure and V_{DC} at 2 μm, 105 nm, 297 K, vacuum, and 2 V, respectively.
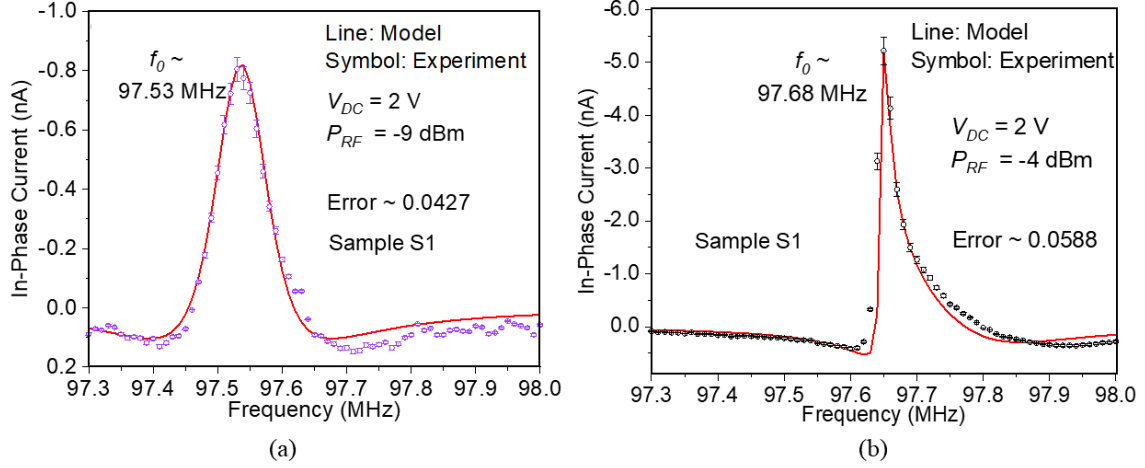
Figure 4.4 Single Curve data fitting for sample S1 ($L = 2\,\mu m$). (a)A linear resonance response fitting with resonance frequency at 97.53 MHz with driven power at -9 dBm. (b) A nonlinear resonance response fitting with resonance frequency at 97.68MHz with driven power at -4dBm.

Resonance frequency are 97.53 MHz for -9 dBm and 97.65 MHz for -4 dBm, which showed a slight increase of resonance frequency with respect to the increase of RF power indicating a presence of RF hardening. Next, model is implemented onto group fitting for DC dependence and RF power dependence separately. Figure 4.5(a) and (b) show the result of V_{DC} dependence with respect to different length of the beam. The resonance frequency is shifted to lower, and the asymmetry of the line shape becomes prominent with increasing V_{DC}. This trend well-fitted to the previous assumption about the definition of k_e. Higher V_{DC} value quadratically increase the value of k_e, which equivalently decreases the overall value of the coefficient of $z(t)$ leading to lower resonance frequency. In terms of nonlinearity, the values of mechanical nonlinear coefficient β_m are extracted by model fitting, which are -1.54×10^{-4} m^{-2} and -2.82×10^{-5} m^{-2} for sample S1 ($L = 2\,\mu m$ $W = 105\,nm$) and sample S5 ($L = 1\,\mu m$ $W = 105\,nm$), respectively. It can be seen that shorter beam has smaller absolute value of β_m indicating the distribution of coefficients in the perturbation expansion of stiffness K is dominated by its first-order stiffness. Jensen et al., has reported the evidence showing the nonlinearity has a direct link to the displacement [13]. Therefore, larger voltage was applied to the shorter beam in order to drive the vibration with a larger displacement.
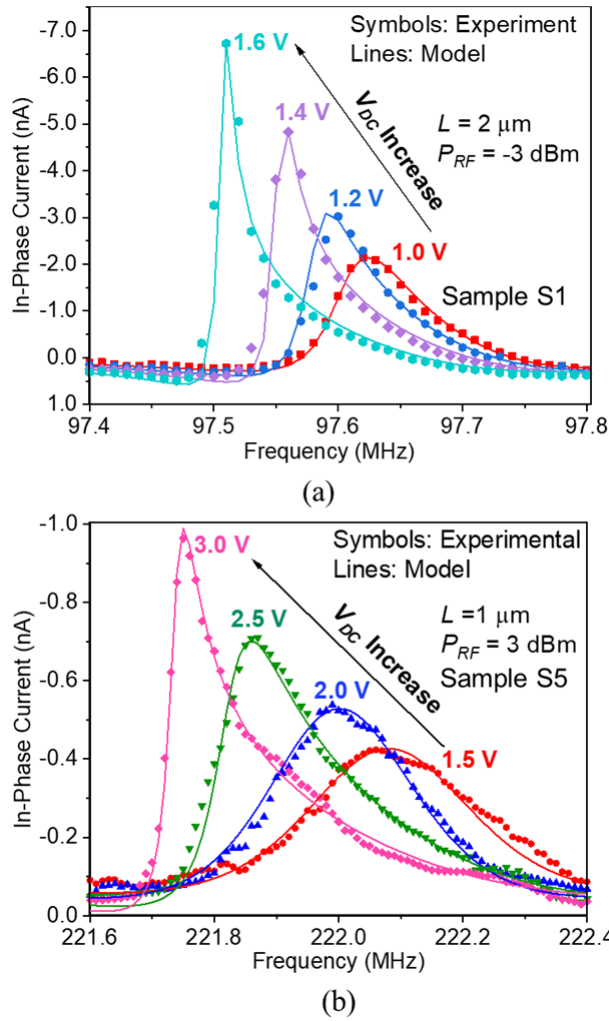
Figure 4.5 Experimental results and model fitting of DC dependence of the resonance for (a) 2-μm-long, (b) 1-μm-long beam sample are plotted.

The simulation result shown in section 3.3.3.3 Figure 3.9 shows DC and AC impact differently on the resonance response and nonlinear characteristics even though they both contribute simultaneously to the electrostatic force where DC impacts more on the change to the stiffness k_e and AC has more effect on the amplitude. According to conclusion by Jensen et al., [55] as amplitude of current is linked to the displacement, AC dependence are expected to present even more clear on the change of nonlinearity. Figure 4.6(a) shows the power dependence for a 2-μm-long beam under V_{DC} at 2 V. The results show that the resonance frequency increases with increasing the input RF power. On the other hand, the increase of power also leads to the nonlinear

characteristics which represents asymmetric line shape of the resonance. We have fitted the set of data taken under different DC voltages and extracted the cubic nonlinear mechanical coefficient β_m of -1.54×10^{-4} m^{-2}. This keeps the same as the one extracted in V_{DC} dependence, which shows great consistency of the fitting. Same methods are used to investigate nonlinear characteristics of shorter beams. Figure 4.6(b) shows the power dependence of the resonance line shapes for the sample with $L = 1.5$ μm. The similar resonance behaviour has been observed but at higher frequencies around 126 to 127 MHz which is consistent for the shorter beam. The overall behaviour is quite similar to what is observed in the 2-μm-long beam. Figure 4.6(c) shows the results for the beam with the $L = 1$ μm and the resonance frequency of around 221 MHz.
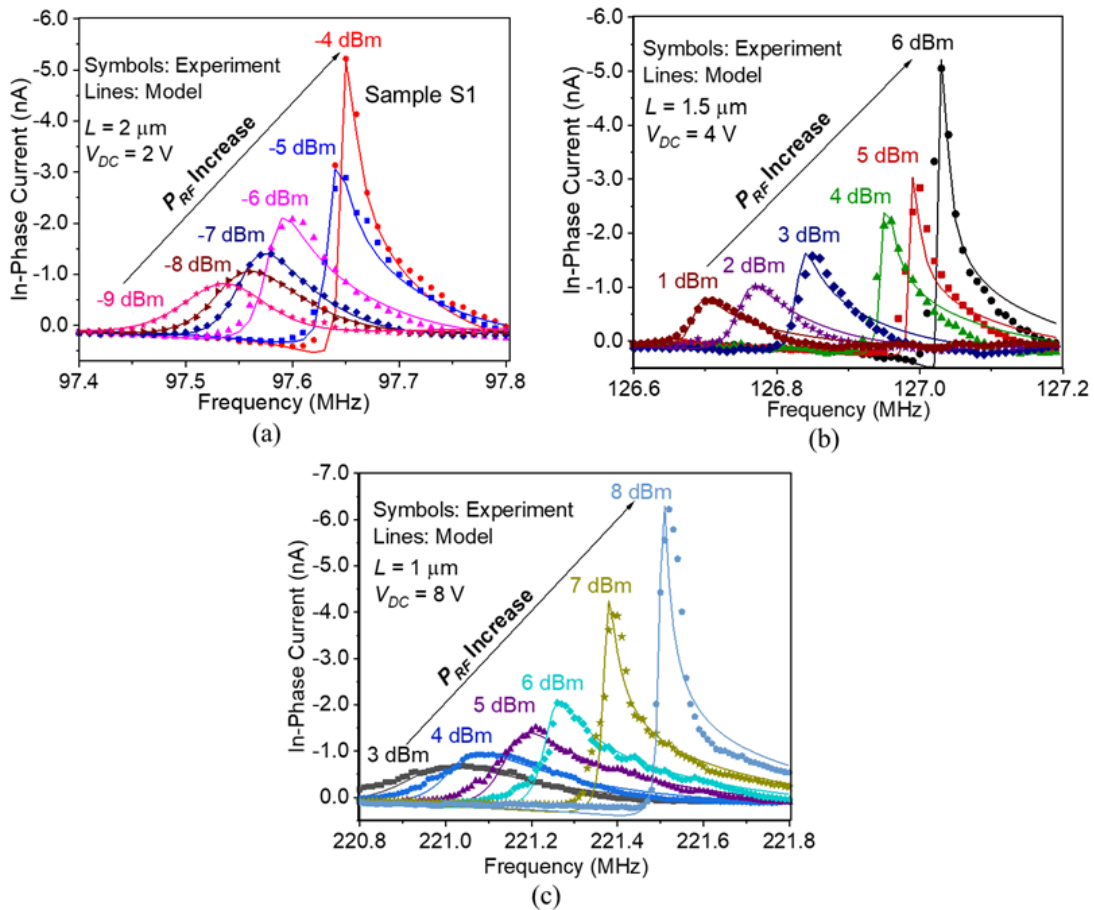
Figure 4.6 Experimental result and model fitting of RF power dependence. Results for beams with length at (a) 2-μm-long sample S1 (b) 1.5-μm-long sample S3, and (c) 1-μm-long sample S5.

CHAPTER 4 Experimental Result with FM Measurement

To find out the RF dependence characteristics for the same sample but with difference DC bias, further to Figure 4.6(a) (V_{DC} = 2 V), a lower V_{DC} at 1 V and higher V_{DC} at 3 V are respectively applied to sample S1, shown as Figure 4.7.

(a)

(b)
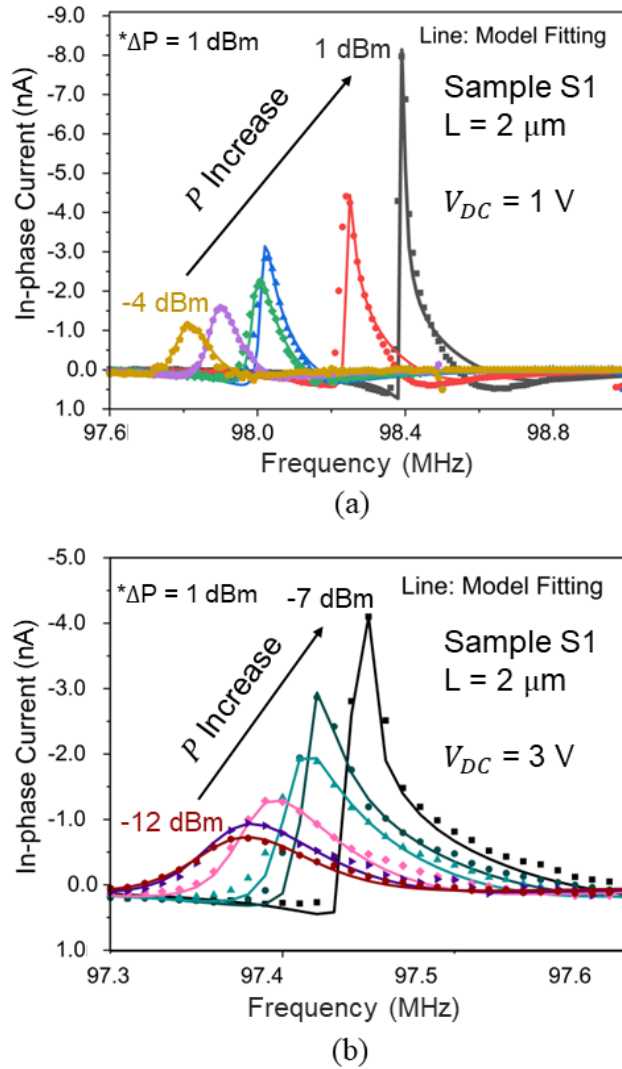
Figure 4.7 RF power dependence for sample S1 with DC at (a)1 V and (b) 3V.

Regardless of the DC bias, all experiment results show that the resonance frequency increases with increasing the input RF power. On the other hand, the increase of power also leads to the nonlinear characteristics which represent the asymmetric line shape of the resonance. The extracted value of β_m keeps the same as the one extracted in V_{dc} dependence, which shows great consistency of the fitting. The negative β_m

indicates the weak softening nonlinearity for the measured NEMS resonator. The extracted β_m for 1-μm-long beam based on RF power dependence results is extracted to the value at -2.8×10^{-5} m^{-2}, which is also very close to the one from V_{DC} model fitting. Meanwhile, the value β_m for the 1.5-μm-long beam is around -5.3×10^{-5} m^{-2}. While the clear nonlinear behaviour at this frequency was not observed in [27], this time very clear nonlinear behaviour similar to the one with the longer beam has been identified by applying higher V_{DC} and driving power than before. To the best of our knowledge, this is the first systematic observation of nonlinear resonance on the fundamental mode of the Si doubly-clamped beam at a higher frequency up to 221 MHz.

In Chapter 3, theory part has discussed the effect about damping and Q. Considering the simulations in section 3.3.3.3, Q values is expected to maintain constant for same device and same testing conditions. After conducting fitting analyses for DC and AC dependencies here, it can be discerned that the same Q value can effectively fit all experimental data. Hassani et al. [26] provide an in-depth discussion on NEMS damping, attributing it to ambient, thermoelastic, and anchor loss. Finite element analysis reveals ambient and anchor loss as the dominant factors among the three. I perfomed long-time testing under identical input conditions for the same device, result shows that the resonance curve's bandwidth and resonance frequency remain stable. This stability allows us to understand that, in the context of this voltage dependence testing, the dissipation of the same device is consistent under uniform testing environments. Consequently, the Q value remains unchanged and independent of DC and AC. For different devices, the Q values for S1 and S5 are 580 and 330, respectively. Stassi et al. [88] have previously discussed the variation of MEMS/NEMS Q values with device dimensions, and their findings align with the conclusions of this section, indicating a gradual decrease in Q values as device size diminishes.
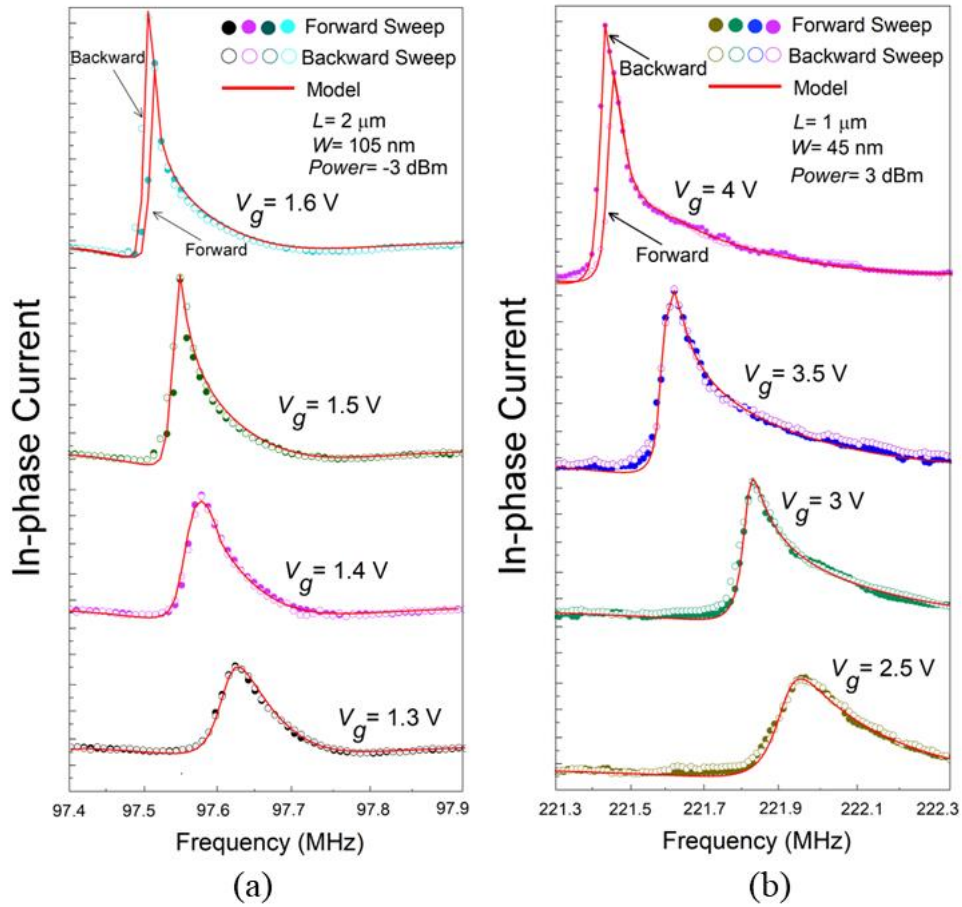
Figure 4.8 Hysteresis phenomenon observation and model fitting. (a)Hysteresis at $V_{DC} = 1.6$ V for sample S1 with $L = 2$ μm, (b) Hysteresis at $V_{DC} = 4$ V for sample S5 with $L = 1$ μm.

One challenge remained is the hysteresis behaviour, which is also the most known characteristics in a nonlinear dynamic system presenting bifurcation phenomenon. Under the proposed theory regarding the hysteresis threshold equation is implemented into the model. With the β_m extracted after the model fitting in previous DC and AC dependence, the hysteresis simulation successfully fitted with the experimental data as shown in Figure 4.8.

(a)

(b)
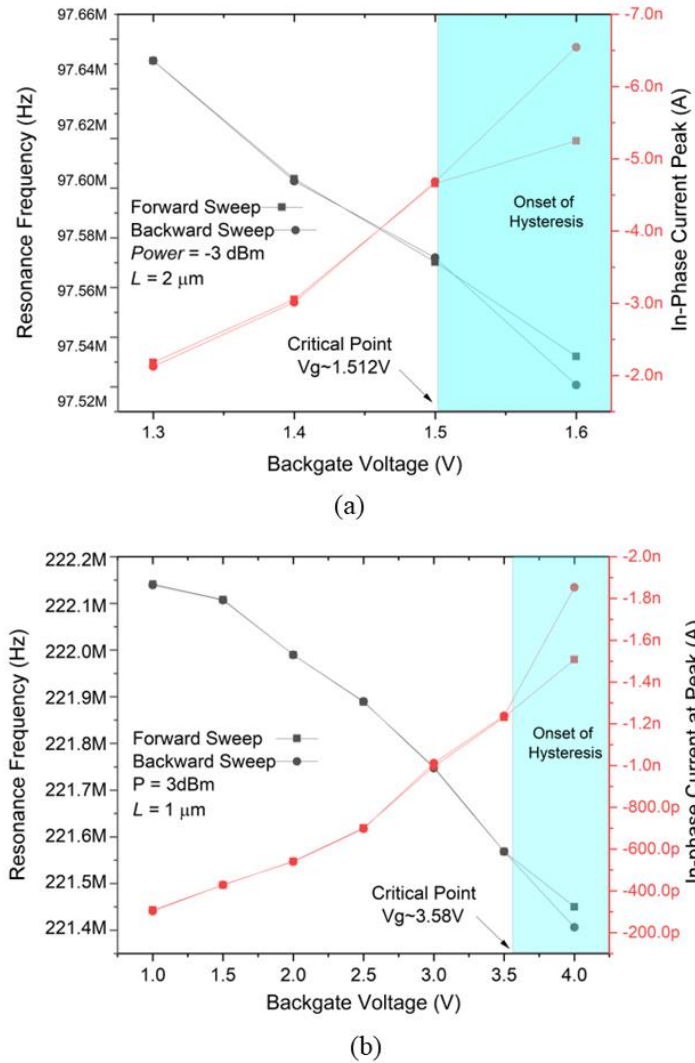
Figure 4.9 A summary of resonance frequency and peak amplitude change with respect to the V_{DC} dependence for sample (a) S1 ($L = 2$ μm), (b) S5 ($L = 1$ μm).

Figure 4.9 proves the point that when increase V_{DC} from 1.5 to 1.6 V, for 2-μm-long beam (Figure 4.9(a)), and 3.5 to 4 V (Figure 4.9(b)) for 1-μm-long beam, both present the clear hysteresis behaviour when comparing the forward frequency sweep to backward frequency sweep. The critical V_{DC} pointed on each of figure represents the theoretical threshold based on the calculation by Equation (3.59). The onset of hysteresis via experimental observation perfectly follows the theoretical prediction. Noted that this is not only the first observation about the hysteresis behaviour for a Si-NEMS resonator in very-high-frequency (VHF), but also the very first trail with systematic fitting to present the before and after the onset of hysteresis. Hysteresis

96

behaviour occurs when nonlinearity grows into relatively stronger region. In our model, the increase of V_{DC} pushes the system into more intensive nonlinear oscillation.

4.3. Summary

In this chapter, we introduce a testing method for FM lock-in and, for the first time, provide a detailed explanation of the displacement-to-current conversion mechanism for Si-NEMS based on this testing approach. Utilising the previously published conversion factor S_{iz}, we fit its relationship with V_{AC}. Thereby, validating the rationality of the derived conversion mechanism formula. Subsequently, the displacement obtained from the model developed in the previous chapter are calculated and, through conversion, transformed it into FM current. This is then compared and fitted with experimental results under equivalent conditions. Following the methodology in Section 3.4 of the previous chapter, we obtain a group fitting of the DC and RF power dependence for Si-NEMS. The model accurately fits the experimental results for various DC and RF power dependences under different DC conditions, different RF power dependence under various AC conditions, and different sample size. Moreover, a set of parameters can fit the results obtained under all experimental conditions. This observation is in complete accordance with the definition of β_m provided in the previous chapter. Lastly, with the corresponding parameter values extracted from fitting, this chapter demonstrated the hysteresis onset points calculation based on these parameters. By conducting model fitting for the experimentally observed hysteresis phenomena up to 220 MHz, the validity of this theory is confirmed.

In the recent surge of interest in neuromorphic computing schemes based on nonlinear MEMS, the presence of instability with hysteresis is regarded as a better model to describe human neuron system [24]. Specifically, MEMS operating within the hysteresis region exhibit bi-stability, characterised by analog dual states. These states can instantaneously shift in response to external stimuli while maintaining ultralow leakage current. This behavior is utilized to describe switch-like ON and OFF states

and memory capabilities. Moreover, coupling two nonlinear MEMS devices enables one to drive the other through state changes, leading to a model termed dynamic field theory coupled neurons. This model lays the foundation for future nonlinear MEMS/NEMS neuron networks. Consequently, delving deeper into the study of hysteresis holds substantial significance.

CHAPTER 5

Experimental Result with 1-$\boldsymbol{\omega}$ Mixing Measurement

1-ω mixing measurement is an alternative method to detect the resonance behaviour of NEM resonators by using the NEM resonator as a mixer of radio frequency (RF) signals, where the data analysis is found to be much simpler than that in the FM method. In this chapter, the analysis of nonlinear resonance based on the model proposed in this thesis is applied for the experimental datasets taken via the 1-ω mixing measurements. The correspondence between the dimensional or material parameters of physical Si-NEMS resonators and the physical parameters appearing in the model will be discussed systematically. This chapter will also include an analysis of characteristic hysteresis behaviours and a conversion coefficient between the detected current and the displacement of the beam for 1-ω mixing measurement.

5.1. 1-ω Mixing Measurement Setup

Figure 5.1 shows a schematic diagram of a 1-ω mixing measurement system to detect

the resonance of NEM resonators. An RF signal with the frequency ω generated by Agilent N5181A MXG Signal Generator is split into two by the power splitter. One is fed to a bias tee where the RF signal is combined with DC bias generated by Agilent B1500 Device Analyser, and then applied to the back electrode of a NEM resonator. Another is connected to a mixer where a reference signal with the frequency of ω_L generated by Lock-in Amplifier SRS850 is mixed and then led to the input electrode for the suspended nanobeam. The output electrode of the beam is connected to the lock-in amplifier to detect the current modulation of the beam for the frequency ω_L.
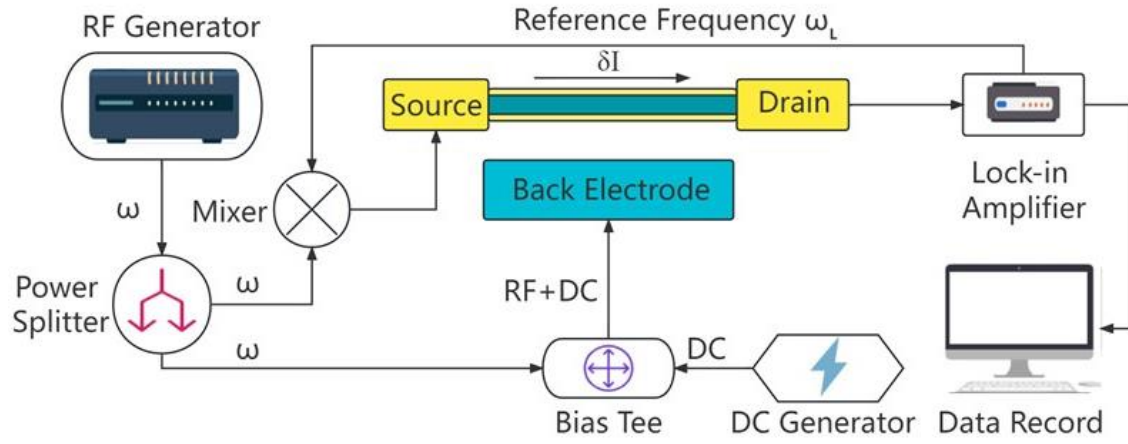
Figure 5.1 A 1-ω mixing measurement diagram. V_{DC}, V_{AC}, and V_L are the actuation voltage, RF, and modulation signal amplitudes, respectively. ω_L is the modulation frequency.

The current modulation amplitude δI for ω_L is expressed as [48],

$$\delta I = \frac{1}{2\sqrt{2}} \frac{\delta G}{\delta V_{DC}} \left(V_{AC} + V_{DC} \frac{\delta C_g}{C_g} \right) V_{AC} V_{\omega_L} \tag{5.1}$$

with the transconductance $\delta G / \delta V_{DC}$ and the gate-beam capacitance modulation $\delta C_g / C_g$. V_{ω_L} is the amplitude of the reference frequency signal. At the resonance, the capacitance modulation is enhanced due to the increase of the beam displacement, resulting in appearance of peak of the current modulation signal at the resonance with respect to the frequency sweep. Equation (5.1) is used to as a conversion to link

between the current modulation data obtained experimentally and theoretically-deduced displacement value in the following comparative study.

5.2. 1-ω Mixing Measurement Result and Model Fitting

The conversion shown as the above equation explain the strengths of using 1-ω mixing measurement that its mechanism is more straightforward and easier for understanding. Nevertheless, the value of transconductance $\delta G/\delta V_{DC}$ needs to be given prior to the model fitting. This results in another benefit of using 1-ω mixing technique is that it can directly give the value of $\delta G/\delta V_{DC}$ from the experiment, simply by setting the V_{DC} to zero and the current response, accordingly, is written as a function of $\delta G/\delta V_{DC}$.

$$|I_{bg}| = \frac{1}{2\sqrt{2}}\frac{\delta G}{\delta V_{DC}}|V_{\omega_L}|\,V_{AC}{}^2 \qquad (5.2)$$

I_{bg} of a NEM resonator with L = 1.5 μm and W = 105 nm has been measured with increasing applied RF power and plotted in Figure 5.2.
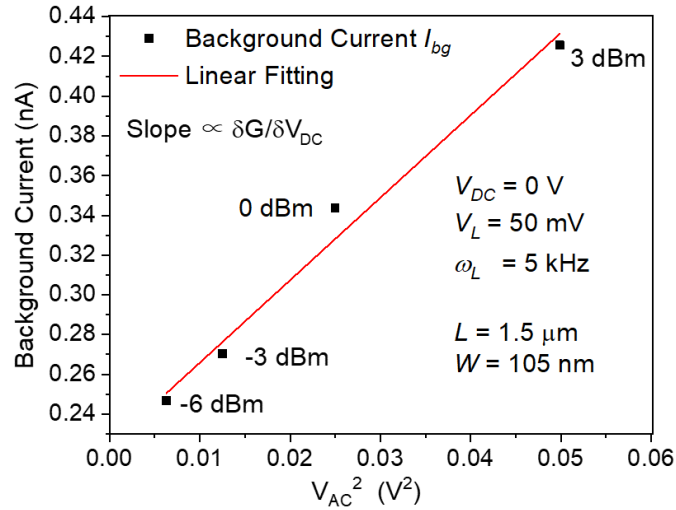
Figure 5.2 Background signal vs V_{ac}. $\delta G/\delta V_{DC}$ is extracted from the linear fitting.

Taking V_{AC}^2 as a horizontal axis, clear linear relationship between I_{bg} and V_{AC}^2 indicates the transconductance $\delta G/\delta V_{DC}$ is constant in this power range. With $V_{\omega_L} = 50$ mV, the transconductance $\delta G/\delta V_{DC}$ is estimated 54.5 nS/V, which will be used for data analysis in the following.
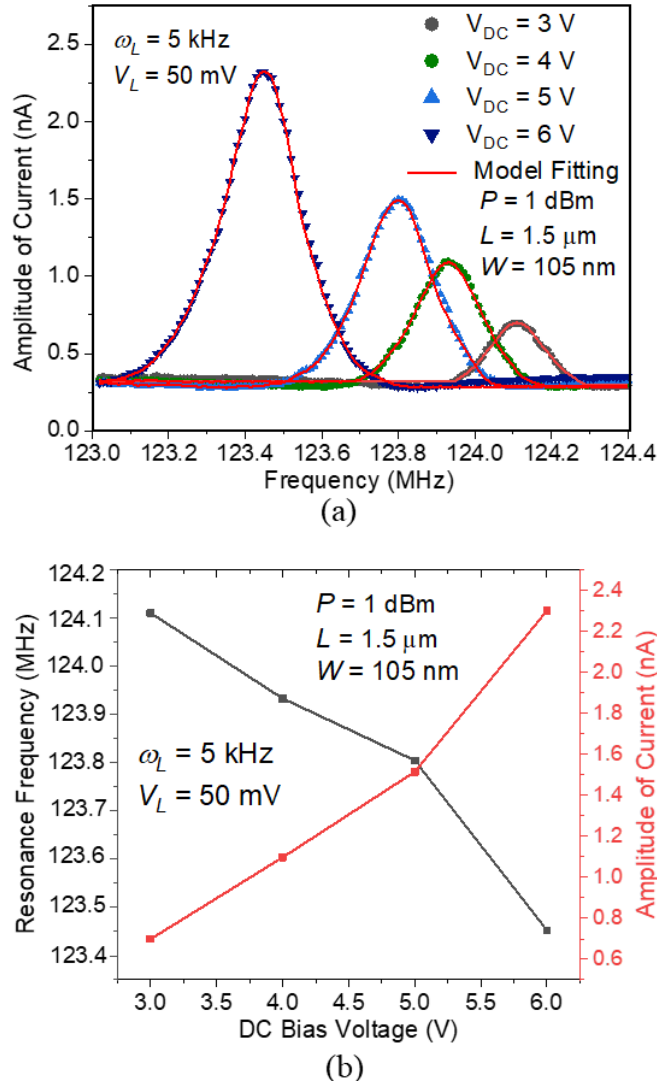
Figure 5.3 (a) DC bias dependence of the resonance line shape. (b) A summary of how the resonance frequency and peak current change with respect to the DC bias.

Figure 5.3(a) presents how the resonance lineshape is developed with changing V_{DC} for the modulation current on the NEM resonator with $L = 1.5$ μm and $W = 105$ nm. Marks plotted in Figure 5.3(a) are experimental data. At $V_{DC} = 3$ V, the resonance appears at around 124.1 MHz and then the resonance frequency is shifted leftwards with increase of V_{DC}.

Note that the current amplitude at the resonance has increased with increaseing V_{DC}, from 830 pA to 2.47 nA when V_{DC} is increased from 3 V to 6 V. Figure 5.3(b)

summerizes the V_{DC} dependence of the resonance frequency and amplitude of the current modulation. The red solid lines in Figure 5.3(a) are model fitting curves. The well-fitted results suggest our approximated solutions can explain well how the resonance is changed with respect to the actuation voltage V_{DC}.

The downshift of the frequency with applying V_{DC} corresponds to effects of equivalent electrical linear stiffness k_e. The total amount of stiffness is characterised as a coefficient of $z(t)$ term in Equation (3.21) which is $\omega_0^2 - k_e$. With increasing V_{DC}, k_e increases according to its definition as shown in Equation (3.19) so that the total amount of linear stiffness is decreased, resulting in the left shift of the resonance. This is also called electrical softening effect. The increase of the current amplitude with increasing V_{DC} is also well consistent with Equation (5.1) where the V_{DC} increase contributes directly as well as the increase of increase of electrostatic force, leading to further displacement of the beam and then modulating the capacitance.

A set of graphs in Figure 5.4 display the result of resonance characteristics of the 1.5-μm-long and 105-nm-wide NEM resonator beam (sample S3) under varied RF power P with a unit of dBm. For each fixed V_{DC} of 3, 4, 5, and 6 V (Figure 5.4 (a) to (d)), the RF power is increased from 2 dBm to 10 dBm with a step of 2 dBm, and each lineshape of resonance curve for the current amplitude is plotted accordingly with respect to the frequency.

Again marks are based on experimental data, whereas the red lines are based on the numerical solution of the model. For all four groups of RF power dependence in Figure 5.4 under differentr V_{DC}, the current amplitude increases with increasing the RF power. Looking into the details, in Figure 5.4(a), the resonance frequency moves to slightly higher with the increase of power, which corresponds to linear hardening effect. This effect is still observed at V_{DC} = 4 V in Figure 5.4(b).
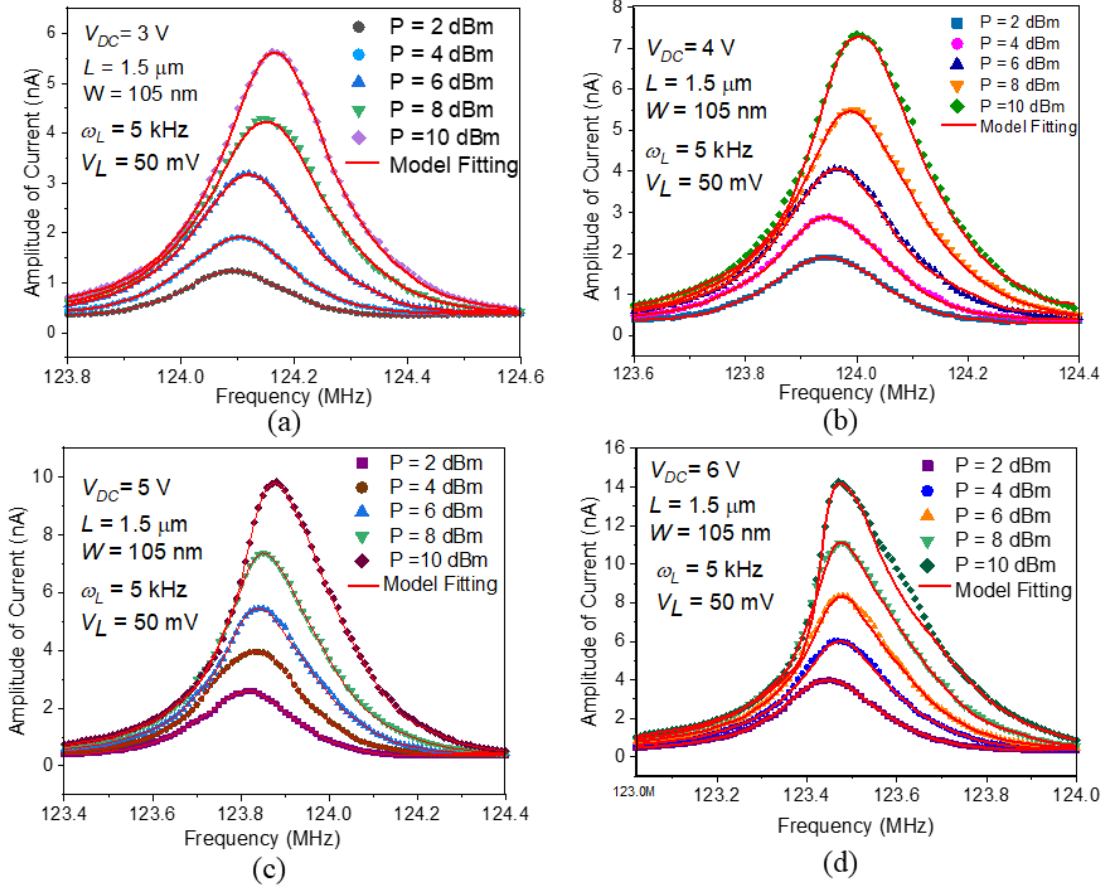
Figure 5.4 Power dependence of the resonance line shape at varying DC bias at (a) 3 V, (b) 4 V, (c) 5 V, and (d) 6 V.

On the other hand at V_{DC} = 5 V in Figure 5.4(c), the resonance curve with higher RF power starts showing assymmetric and the top of the peak tends to bend to lower frequencies. This is commonly known as Duffing nonlinear softening effect, which is observed more explicitly in Figure 5.4(d) with further higher V_{DC} at 6 V. Strength of nonlinearity is directly proportional to the displacment according to Bartsch et al., [89] which is well consistent with our observation where nonlinear behaviour turns to be more prominent with increaseing V_{DC} and RF power.

Note that, our model fitting results are well consistent with the experimental data throughout the varied RF power values in this study. The nonlinear equivelant electrical stiffness β_e defined Equation (3.20) can explain how nonlinearity can be tuned by changing V_{DC} and V_{AC}. Another key parameter representing the nonlinearity is the mechanical nonlinear stiffness β_m, which denotes the intrinsic amount of

nonlinearity from the mechanical structure of the device. Without changing the dimensions, design and material of the device, β_m is considered to remain constant theoretically. Upon this hypothesis, we have successfully obtained β_m as a fitting paraneter in current fitting of the whole four groups of power dependence data with resprct to the fitting variables of V_{DC} and V_{AC}. For the purpose of validation of the method, we use another NEM resonator sample with a slightly wider beam (L = 1.5 μm, W = 135 nm) and apply the identical approach to extract the fitting parameters in our analysis, the resonance frequency ω_0, quality factor Q, and the mechanical nonlinear stiffness β_m. Table 5.1 summerizes the parameters extracted from the fitting results for the two samples with different widths.

Table 5.1 A summary of extracted parameters in fitting for 1.5-μm-long beams with different design widths

Sample ID	S3	S4
Width (nm)	105	135
Resonance (MHz)	125.38	127.62
Quality Factor	~560	~528
β_m (m^{-2})	-5.58$\times 10^{-5}$	-7.72$\times 10^{-5}$
$\delta G/\delta V$ (nS/V)	~54.5	~63.3

The transconductance of the sample with W = 135 nm is also estimated from the baseline noise. The wider beam shows a higher resonance frequency and a slightly lower quality factor, corresponding to the increase of stiffness, and has a higher transconductance that is consistent with the increase of conductive cross-sectional area. As for the mechanical nonlinearity stiffness β_m, a slightly large negative value for a wider beam could be linked with the increase of overall stiffness of the beam as well. Overall throughout the comparison of the fitting results between two different NEM resonator samples, we have confirmed very good consistency between the experimental results and numerical solutions. The onset mechanism of hysteresis has been addressed in chapter 3 where analysis method has been introduced in chapter 4

with FM. For the consistency of study, here, Sample S3 and S4 are selected to the hysteresis behaviour observation under the 1-ω mixing measurment scheme.
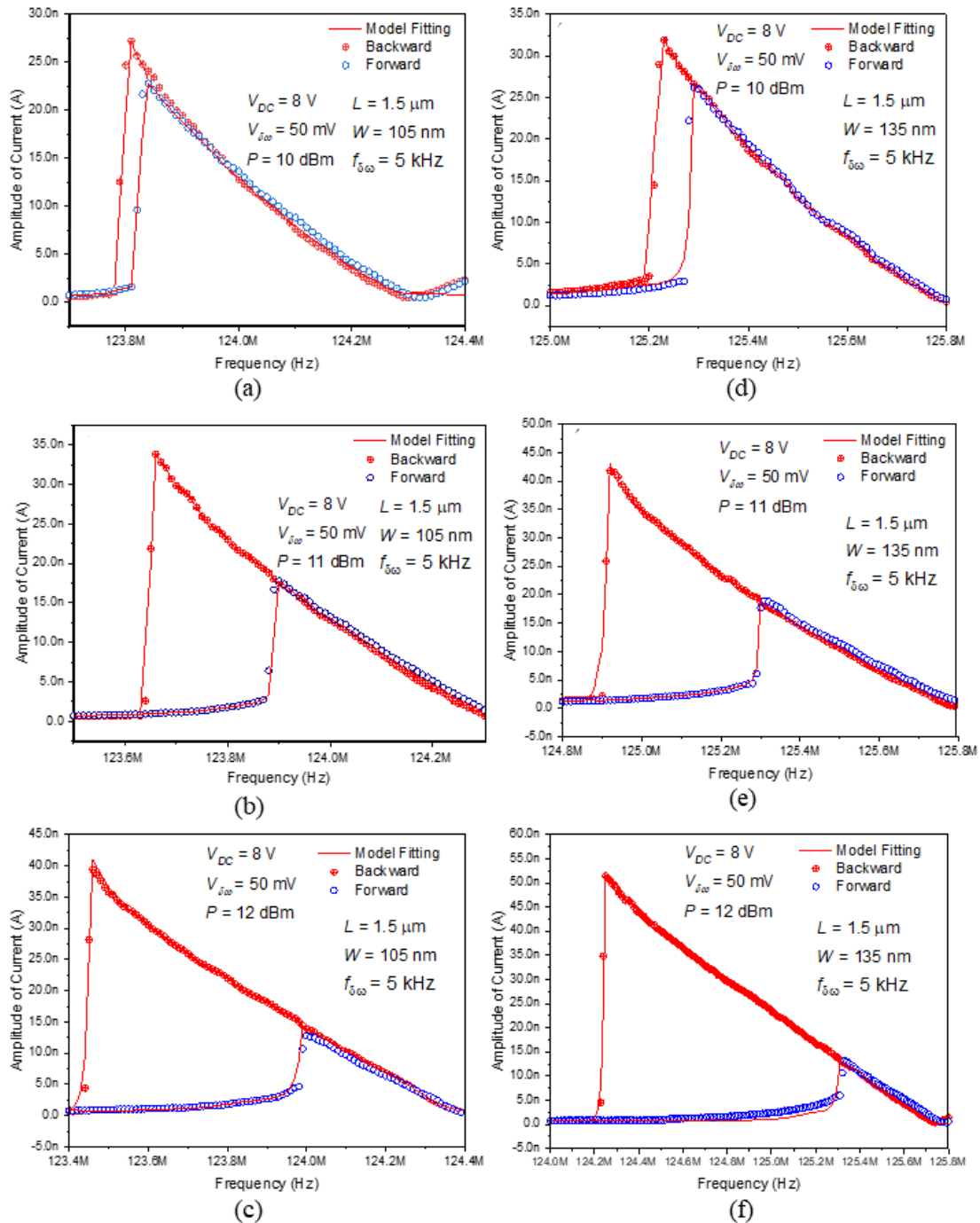
Figure 5.5 Hysteresis behaviour observed for sample S3 and S4 are plotted with the power level at (a) and (d)10 dBm, (b) and (e) 11 dBm, (c) and (f)12 dBm, respectively.

Figure 5.5(a) to (f) systematically shows how hysteresis behaviour is developed with increasing the power at the fixed V_{DC} of 8 V for sample S3 with width at 105 nm where Figure 5.5(d) to (f) are the hyseteric behaviour with identical experimental conditions for sample S4 with width at 135 nm. Blue and red open circules represent experiment data with forward frequency sweep and backward frequency sweep, respectively. By extracting the maximum and minimum solutions of the Duffing equation in Equation. (3.21) the experimental data with hysteresis are successfully fitted as the red lines in Figure 5.5(a) to (f).

(a)

(b)
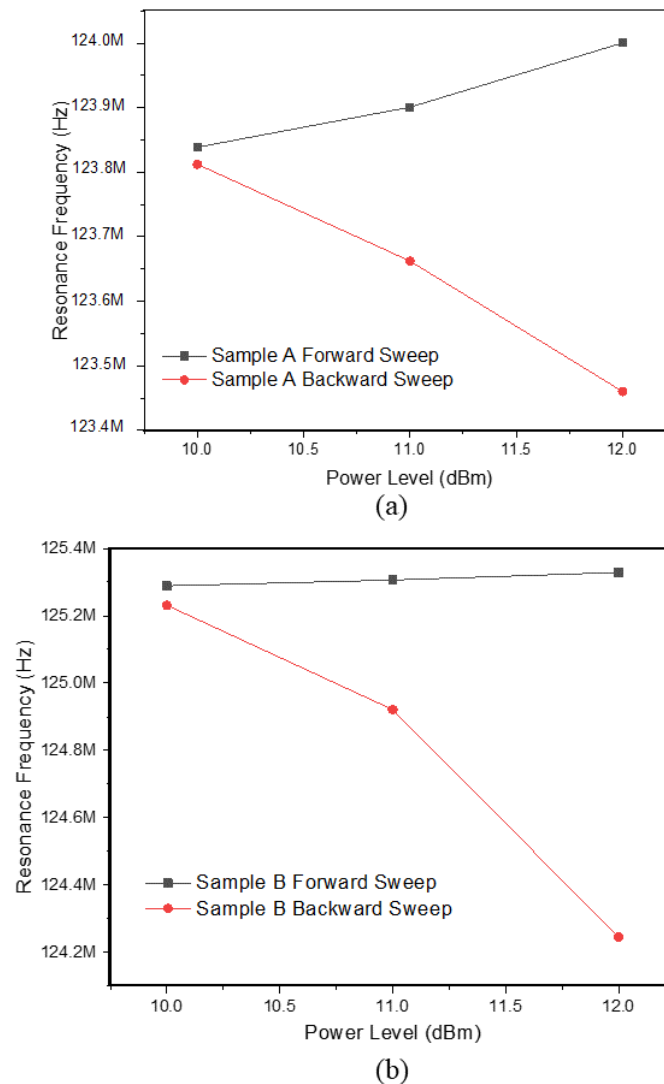
Figure 5.6 A summary of the resonance frequency and peak current are changed with respect to power in hysteresis regime for sample (a) S3 and (b) S4

To clearly demonstrate the 'split' due to bifurcation, Figure 5.6 summerises the resonance frequency change with respect to the increase of power level within hysteresis regime. It shows how the resonance frequencies are shifted in the hysteresis regime with respect to the RF power. The seperation of two resonance frequencies becomes larger with increasing the RF power, leading to the frequency difference Δf of 0.5 MHz at $P = 12$ dBm.

In traditional memory devices like static random access memory (SRAM), the signal margin for switching between 'ON' and 'OFF' states is a crucial metric, where a larger signal margin generally stands for an improved robustness during the 'Hold' state. Similarly, in future neuron network schemes employing nonlinear NEMS hysteresis, the frequency difference of hysteresis serves as a comparable indicator of system robustness. Although specific criterion has not yet been proposed for this metric, our research yields a Δf of 0.5 MHz, significantly surpassing the Δf ~100 Hz obtained by the Zega group, which is one of the leading research group in this field. This not only underscores NEMS' enhanced ability to manifest distinct hysteresis characteristics but also highlights the efficacy of our model in accurately describing this phenomenon.

5.3. Summary

For advancing of silcon-based integrated systems for various applications such as neuromorphic information processing or IoT devices, simple and accurate modelling of individual devices becomes more important. The FM based measurement brings certain complexity in the analysis, which is not only that it is less straightforward to understand, but also this complexity brings inaccuracy. Hence, this chapter demonstrate the attempt to explain the experimenal data for an actual silicon based NEM resonator with the resonance frequency in the VHF range by using 1-ω mixing measurement where its conversion mechanism is simple and clearly presented at the beginning of this chapter. Also, thanks to that, the uncertain factor transconductance has been proved to be able to measured directly from the experiment, which further

benefits the precise in analysis. Later, with using similar stratagy as FM, the DC dependence, RF power dependence, and hysteresis are successfully observed via 1-ω mixing techniques and the experimental data are systematically well-fitted by the model . We believe this attempt is to be a key first step of model development for NEM resonator/oscillator devices including their behavour in nonlinear regime.

CHAPTER 6

Thermo-mechanical Noise

Chapter 2 introduces the basis and significance of thermo-mechanical noise (TMN) with respect to the performance of a ultrasmall scale device. Not only it can reveal the device characteristics for the non-forced states, but also it is essential to pave the way to explore even smaller scale of design. As the importance of miniaturised devices and their nonlinearity has been well addressed in the previous chapters, this chapter will focus on the thermo-mechanical noise measurement for the NEMS resonators used in this study. Note that, this part is done with my colleague, PhD student, James Fernando who has developed measurement procedure and mainly conducted data acquisition and analysis of the voltage dependence. In this chapter, I will demonstrate the measurement and modelling efforts which are related to my contribution to the study about TMN measurements.

6.1. Experimental Setup

Differ from the aforementioned TMN measurement with optical scheme, my contribution regarding TMN is primarily focused on electrical method test with spectrum analyser Advantest R3477 and a semiconductor analyser Agilent B1500A.

The NEMS resonator with the designed beam dimension of length $L = 2$ μm with width $W = 135$ nm (Sample S2) was used in this study under the condition of room temperature and vacuum. Detection scheme is shown in Figure 6.1, with the output connected to a spectrum analyser. DC bias voltage was applied at the back gate from the semiconductor device analyser Agilent B1500A
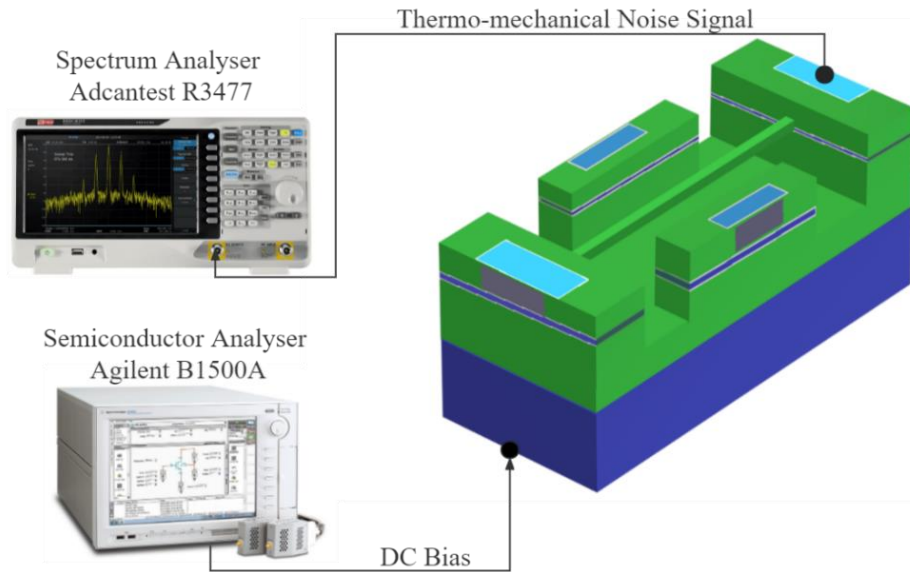
Figure 6.1 Connections between NEMS device terminals and test apparatus in the spectral analysis process. Bottom left inset shows schematic diagram of the NEMS beam, showing critical dimensions.

The detected power signal was converted into a root mean square voltage, which was divided by the square root of the product of resolution bandwidth (RBW) and the resolution-to-noise bandwidth conversion factor for a digital FFT-based spectrum analyzer ($K_N = 1.056$), yielding a voltage spectral density, $S_{v,th}^{1/2}$.

6.2. Measurement Results and Discussion

In Figure 6.2, a typical graph presenting spectrum density data, theoretical curve fitting, and conversion from the voltage spectrum density to the displacement

spectrum density is shown. An original contribution has been published in the International Conferences of Micro and Nano Engineering 2021 (Fernando et al., MNE2021, See the list of Publication). Note that for this plot in Fig. A.2, I use data taken by myself. The resonance frequency detected with this method, $f_0 = 97.84$ MHz is close to its mechanical resonance measured by using frequency modulation, as aforementioned, at $f_0^{FM} = 97.75$ MHz, which corresponds to thermomechanical noise that originated from the thermomechanical motion, $S_{v,th}^{1/2}(\omega_0)$ at its eigenfrequency.
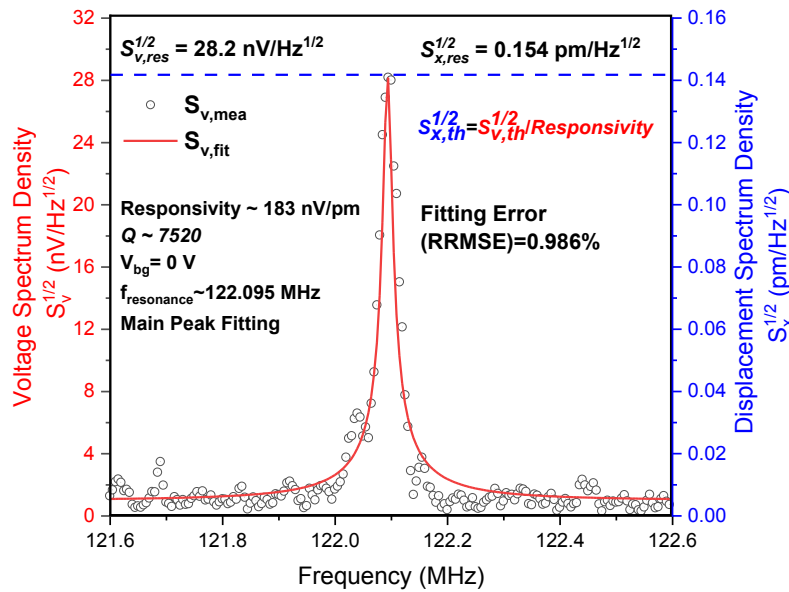
Figure 6.2 The peak of the voltage spectrum density corresponds to the theoretical maximum of displacement spectrum density, allowing a responsivity factor to be obtained.

After converting into $S_v^{1/2}$, the data in frequency domain, is then fitted by modelling the Equation (2.5). Figure 6.2 is an example of model fitting result with MATLAB simulation. The non-forced displacement is calculated via a variant of the nonlinear model described in chapter 3 where the electrostatic force is set to zero but the β_m value still exists to remain the participation of nonlinearity. The spectrum density to TMN motion model shown in Equation (2.4) is employed to obtain the calculated spectrum density. Then, the calculated spectrum density can be used to fit the experimental data, which is exactly the same fitting strategy as aforementioned in

Chapter 4 and 5. The aim of the model fitting is to acquire the value of responsivity $\mathcal{R}$, which is the key as a conversion to understand the $\sqrt{S_v/S_x}$ as a significant part of TMN characterization. With Q of 7520, $S_{x,th}^{1/2}(\omega_0)$ at resonance point is calculated at 0.154 pm/Hz$^{1/2}$, resulting a responsivity $\mathcal{R}$ at 183 nV/pm. The integral of $S_{x,th}^{1/2}(\omega)$ at frequency domain results in the displacement value showing the thermomechanical resonance displacement at 22.44 pm for this specific motion. Fernando et al. has further demonstrated the voltage-tunability regarding the pico-meter level TMN displacement, details can be found in his publication [90].

6.3. Summary

In summary, building upon the description of the mechanism and significance of thermo-mechanical noise (TMN) in chapter 2, this chapter investigates the TMN of NEMS resonator devices with the aid of a spectrum analyser. Initially, the chapter elucidates the methods for testing TMN, followed by a slight modification to the model established in Chapter 3. By setting the electrostatic force to zero, a non-forced model was obtained and subsequently fitted to the experimentally measured spectrum density. The fitting results demonstrate that the non-forced model can accurately describe the TMN characteristics of NEMS resonators under corresponding experimental conditions. Moreover, the responsivity values were obtained through parameter extraction. This finding is particularly beneficial for future research on smaller-scale devices, as miniaturization is accompanied by smaller-scale responses, necessitating highly sensitive testing methods, TMN serves as an ideal choice in this regard. Furthermore, the primary focus of this study, nonlinearity, has a significant portion of its origins in intrinsic properties. Although electrical nonlinearity has predominantly occupied the forefront in previous electrical tests, intrinsic nonlinearity could potentially be amplified at smaller response scales, thereby affecting device performance. Consequently, from this perspective, TMN research also plays an indispensable role in the investigation of intrinsic nonlinear properties for ultrasmall scale device.

CHAPTER 7

Conclusion and Future Plan

7.1. Conclusion

In summary, because the arise of nonlinearity in micro- and nano-electromechanical system (MEMS/NEMS) can be attributed to the miniaturization of dimensions and the increase in operating frequency, to conduct a comprehensive analysis of nonlinear characteristics and explore potential future applications that exploit this feature, this thesis presents systematic observations and analysis of the nonlinear properties of nano-electromechanical resonators (Si-NEMSs). This thesis began with an introduction about the indispensable role of MEMS as a horizontal architecture in very-large-scale integration (VLSI) for modern smart devices. The development transition from MEMS to NEMS is marked by various advantages derived from the scaling down, such as greater integration, higher operating frequencies, and reduced power consumption. However, the miniaturization process concurrently introduces more pronounced nonlinearity, a pressing issue that requires attention and resolution. Despite the initial perception of nonlinearity as undesirable due to its intrinsic instability, chapter 2 presented the unrelenting efforts and contributions of investigators regarding nonlinearity research in micro- and nano-scale systems over the past five decades. A detailed review of observations and analyses of the nonlinear

characteristics of MEMS/NEMS with varying dimensions, materials, and designs was provided in this chapter. Furthermore, in the latter part of chapter 2, recent explorations and attempts by researchers to exploit the potential applications of nonlinearity in MEMS/NEMS were introduced. These included employing nonlinearities to enhance the sensitivity of mass detection under high-amplitude conditions and utilizing the unique bistable hysteresis effect of nonlinearity to treat coupled devices as virtual nodes for non-digital neuromorphic computing. These attempts into applications based on nonlinearity, along with the inevitable nature of nonlinearity at the nano-scale, leads to the observation and in-depth investigation of nonlinear NEMS characteristics an urgent necessity.

From chapter 3, the details of a silicon doubly-clamped Si-NEMS employed in this project were introduced. These devices were designed by Faezeh Arab Hassani and fabricated by Commissariat à l'Energie Atomique et aux Energies Alternatives Laboratoire d'électronique des technologies de l'information (CEA-LETI) using silicon-on-insulator (SOI) platform. Initially, an overview of the device fabrication process was introduced to illustrate the Si-NEMS device structure, material composition, and corresponding dimensions. Later in chapter 3, the Duffing equation was explained, and based on it, a nonlinear model for the Si-NEMS was explicitly described. In this process, two major origins of nonlinearities were discussed, named as intrinsic mechanical nonlinearity and electrical nonlinearity. A perturbation series was implemented to the system overall restoring force and guided by the device's symmetry and displacement scale, the third-order response was selected and marked as β_m. Thereafter, the system's operation with beam and back gate was treated as parallel plates, and then a Maclaurin expansion regarding the periodic electrostatic force between the plates were performed which enabled to extract the electrical nonlinear stiffness as a function of DC and AC, denoted as β_e. Owing to the novel use of β_m and β_e, the model was able to possess a detailed characterization of the intrinsic nonlinearity magnitude as well as the voltage-dependent nonlinearity. Subsequently, the Petrov-Galerkin (P-G) method was employed to approximate the conversion of the time-domain nonlinear model to a frequency-domain model. The Newton-Raphson iteration (NRI) was then applied to iteratively solve the frequency-domain

model, yielding the steady-state solution for the corresponding frequency.

Among the fabricated devices, six perfectly functioning Si-NEMS devices with different dimensions (lengths vary from 2 to 1 μm, widths vary from 135 to 45 nm) were selected and placed in a Lakeshore cryogenic prober station for resonance testing. In later chapters, because of the simplicity of platform setup, FM was employed to test the resonance characteristics of the Si-NEMS. Using this approach, the nonlinear resonance of Si-NEMSs under different dimensions were successfully observed. The observation regarding asymmetry resonance has been reported in the literature review chapter and was attributed by the growing proportion of nonlinearity in the system, which gradually dominates the resonance response. The asymmetric energy release leads to nonlinear displacement during the vibration process. Subsequently, after discussing and analyzing the signal conversion of the FM testing platform, an explicit FM displacement-to-current conversion mechanism was proposed where the lock-in current is proportional to the derivative of frequency response of displacement. Simultaneously, the nonlinear DC and RF power dependence was clearly observed up to 221 MHz. This phenomenon also demonstrated that the characterization of nonlinearity is directly related to the magnitude of electrostatic force or, in other words, the displacement level. Based on the Si-NEMS nonlinear model derived in chapter 3, by adjusting the magnitude of β_m, we successfully fitted the experimental nonlinear data with respect to the whole DC and RF dependence groups for the first time in the nano-scale and very-high-frequency (VHF) range.

Although FM offers a certain level of simplicity in experimental setup, the discussion of its signal conversion mechanism employs mathematical approximation methods, such as Taylor expansion, leading to unnecessary inaccuracies in the process of converting the model-simulated displacement into the current signal. To address this issue, I constructed a 1-ω mixing measurement platform. This testing method was later proven to be entirely effective and reliable for testing Si-NEMS resonance. Moreover, as the resonator was served as an RF mixer, it directly provides an expression for the capacitively induced current, clearly and directly linking displacement and current, thereby significantly enhancing the model's fitting accuracy.

This measurement also included an analysis regarding the beam transconductance $\delta G/\delta V_{DC}$. For a 1.5-μm-long beam, the transconductance for wider beam (W = 135 nm) and narrower beam (W = 105 nm) were measured to be 63.3 and 54.5 nS/V where their mechanical nonlinear stiffness β_m are -5.58× 10^{-5} and -7.72× 10^{-5} m^{-2}. The electrical nonlinearity β_e, combined with the value of β_m, obtained through data fitting, the entire device's nonlinear characteristics can be quantitatively expressed, and its nonlinearity dependence with respect to DC and RF power level can be accurately described, which is significant for future nonlinear applications based on Si-NEMS.

In the bistable study of Si-NEMS, we tested four devices with different dimensions by increasing the voltage. In the FM tests, we used devices with lengths of 2 um and 1 um and raised their DC to 1.6 V and 4 V, respectively. We successfully observed hysteresis and, by extracting multiple solutions from the model, successfully fitted the hysteresis behaviour. Simultaneously, a comprehensive theory was established to predict the onset of hysteresis. It provided the threshold values for the onset of hysteresis for 2 um and 1 um devices as 1.58 V and 3.5 V, respectively, which successfully corresponded with the experimental results. Subsequently, using the same method, we observed the hysteresis effect for the same beam length but different beam widths in the 1-ω mixing tests and similarly fitted them successfully using the model.

As a novel definition, the mechanical nonlinearity β_m, even in the absence of input, it theoretically still exists. In Chapter 3, I have presented a detailed derivation process of mechanical nonlinearity, thereby illustrating its physical meaning rather than a simple nonlinear factor. This diverges significantly from conventional definitions of nonlinearity, assigning it with physical meaning and designating β_m as an intrinsic characteristic. Therefore, characterising nonlinearity becomes an essential pursuit for future research. The methods for characterisation have been demonstrated in this thesis. I employed two distinct testing approaches (FM in Chapter 4 and 1-ω mixing in Chapter 5) to characterise the nonlinearity of NEMS devices with varying dimensions, resulting in quantified values for mechanical nonlinearity. Thus,

following the explicit modeling of electrostatic nonlinearity, comprehensive quantification of the overall nonlinearity in NEMS is attainable, thereby facilitating the feasibility of nonlinear control and prediction. Regarding damping, given NEMS' relatively large surface-to-volume ratio, nonlinear damping may exist despite not being observed in this study's nonlinear vibration. As early as 2012, Zaitsev et al. conducted an in-depth exploration of damping in the context of the Duffing equation, asserting that nonlinear damping is related to displacement. They proposed an equation for damping involving terms $x^2 x'$ and $(x')^3$ [91]. Such an approach may offer insights for further decomposition of β_m in future research.

Therefore, conducting experimental exploration under non-forced conditions is highly significant for nonlinear analysis. At the same time, as the dimensions are further reduced in the future, the demand for ultrasmall displacement measurements in the picometer range will be extremely high where a measurement with ultra-sensitivity is mandatory. More importantly, thermo-mechanical noise (TMN) testing based on a spectrum analyser is crucial for nano-opto-electromechanical systems (NOEMS), which will be an important expansion based on Si-NEMS. Thus, TMN testing for existing Si-NEMS devices is of great importance. Chapter 6 gives the details that by using a spectrum analyser and without inputting an RF signal to the Si-NEMS, the thermo-mechanical noise of the beam within the resonance range was investigated. Furthermore, the non-forced model was applied to the fitting process, with Q of 7520, the displacement spectrum density at resonance point was calculated at 0.154 pm/Hz$^{1/2}$. The model fitting extracted the value for system spectrum density, resulting a responsivity at 183 nV/pm. The integral of the displacement spectrum density at frequency domain results in the displacement value showing the thermomechanical resonance displacement at 22.44 pm for this specific motion.

The limitation of this work is vital. Due to the impact of COVID-19, certain limitations persisted throughout this research, providing essential guidance for future work based on this study. Even in early 2020, my colleagues have completed the mask design for new NEMS devices. Nevertheless, the outbreak of COVID-19, along with prolonged queueing for cleanroom access after campus reopening, resulted in an incompletion to acquire a sufficient variety of new NEMS devices with differing

dimensions for studying NEMS nonlinearity within the timeframe of this research. Additionally, within the study, though device consistency was maintained to the best extent possible for the same measurement, devices used in different experiments, such as those in Chapter 4, relying on FM-based testing, and those in Chapter 5, employing 1-ω mixing, were not consistent. This was not a deliberate choice but was due to fatigue and contamination of experimental samples following extended testing periods, with no replacement samples available, eventually leading to a lack of cross-comparison in this research. Furthermore, the model proposed in this study can be widely applied to similarly designed micro- and nano-beams. However, it has not been verified for other designs of MEMS/NEMS devices, specifically, any non-doubly-clamped beam designed NEMS, such as dual-fork plate MEMS. Hence, the applicability of the model to devices substantially different from the NEMS used in this study remains uncertain. In the future, adjustments to the model based on device designs will be necessary, while the definition of mechanical nonlinearity can continue to be extended.

7.2. Future Plan

As the continuous study for the part of European FP7 NEMSIC project, upon the availability of Si-NEMS samples, after thesis submission, I will compile all the previously completed measurement data related to Si-NEMS and organize the detailed information about the nonlinear model I have established (including the code, see Appendix A.1 and A.2) as well as the usage of the 1-ω mixing test platform. This information will be consolidated into a manual and preserved within Yoshishige Tsuchiya's group for the benefit of future project development. The future plan for the nonlinear Si-NEMS resonators will be:

- Coupled nonlinear oscillators will be essential for further neuromorphic computing. The coupler could be either mechanical or electrical. A preliminary numerical model for a mechanical coupled oscillator is proposed in Appendix section A.3 based on the similar modelling strategy as per

illustrated in this project while the new coupled Si-NEMS will need to be fabricated. Based on the availability of existing Si-NEMS samples, the electrical coupling could be also worth an investigation. One of the foundational research projects reported by Alsaleem et al., [24] about nonlinear MEMS neural computing utilized the electrical coupling between two nonlinear MEMS where one MEMS served as the detection neuron and its nonlinear bi-stability status can be transferred as an input to the other nonlinear MEMS, served as the memory neuron. The similar scheme of electrical coupling can be easily achieved by wire bonding or using shared electrode in design.

- An attractive direction for the future of this project is in nano-opto-electro-mechanical integrated oscillator arrays for Energy-Efficient Cognitive Computing (NOEMIA) as a continuous of Chist-Era NOEMIA project. The new project is led by my supervisor Dr. Yoshishige Tsuchiya and Dr. Jun-Yu Ou where the nonlinear dynamics will be implemented onto the NOEMIA coupled oscillator and optical detection will be employed to obtain the output signal. This design is based on the doubly-clamped Si-NEMS where a thorough understanding is essential prior to the operation of the coupled Si-NEMS for NEOMIA.

- Sensing enhancement on ultrasmall mass detection will also be an interesting direction. As the result from this project, the scaling down will be accompanied with even severer nonlinear effect. Meanwhile, Sansa et al., has proved that when oscillator is operated at the sub-threshold of hysteresis, the sensitivity can be enhanced. Therefore, nonlinearity not only is inevitable but also can be benefit to the further use of mass sensing.

As for my personal plans, at the time of submitting this article, Micro and Nano Engineering journal returned my journal manuscript. I will complete the revision work and submit it back to the editorial office in April 2023. In addition, another paper in related to FM data has been completed and is awaiting submission to the

CHAPTER 7 Conclusion and Future Plan

Nanotechnology journal. Meanwhile, I will continue to assist Dr. Yoshishige Tsuchiya in completing experimental teaching work on Si-NEMS in the short term. I have also applied for several positions, including postdoctoral research positions related to silicon characterisation and MEMS/NEMS devices at universities in the UK, as well as positions at MEMS-related companies.

Appendix

A.1 Algebraic Derivation with Maple 2020

This section presents the details regarding algebraic derivation. Due to the limit by the export file types of Maple 2020. The following derivation steps and codes are presented as a copy of PDF.

Give first order approximated solution of displacement y(t):

$$A_1 \cdot \cos(\omega \cdot t) + A_2 \cdot \sin(\omega \cdot t) = y(t)$$

$$A_1 \cos(\omega\ t) + A_2 \sin(\omega\ t) = y(t) \tag{1}$$

$$\frac{d}{dt}\left(A_1 \cdot \cos(\omega \cdot t) + A_2 \cdot \sin(\omega \cdot t)\right) = y'(t), \quad y'(0) = 0$$

$$-A_1\ \omega\ \sin(\omega\ t) + A_2\ \omega\ \cos(\omega\ t) = D(y)(t), \quad D(y)(0) = 0 \tag{2}$$

$$\frac{d^2}{dt^2}\left(A_1 \cdot \cos(\omega \cdot t) + A_2 \cdot \sin(\omega \cdot t)\right) = y''(t), y''(0) = 0$$

$$-A_1\ \omega^2\ \cos(\omega\ t) - A_2\ \omega^2\ \sin(\omega\ t) = D^{(2)}(y)(t), \quad D^{(2)}(y)(0) = 0 \tag{3}$$

Write cubic duffing equation and derive the residual force R(t)

$$\left(-A_1 \cdot \omega^2 \cdot \cos(\omega \cdot t) - A_2 \cdot \omega^2 \cdot \sin(\omega \cdot t)\right) + \frac{f_0}{Q} \cdot \left(-A_1 \cdot \omega \cdot \sin(\omega \cdot t) + A_2 \cdot \omega \cdot \cos(\omega \cdot t)\right) + \left((f_0)^2\right.$$

$$\left. -\frac{2 \cdot \varepsilon_0 \cdot S}{m_b \cdot (g_0)^3} \cdot \left(\left(V_{dc} + V_{ac} \cdot \cos(\omega \cdot t)\right)\right)^2\right) \cdot \left(A_1 \cdot \cos(\omega \cdot t) + A_2 \cdot \sin(\omega \cdot t)\right) + \beta_m \cdot \left(A_1 \cdot \cos(\omega\right.$$

$$\left. \cdot t) + A_2 \cdot \sin(\omega \cdot t)\right)^3 - \frac{\varepsilon_0 \cdot S}{m_b \cdot (g_0)^2} \cdot \left(\left(V_{dc} + V_{ac} \cdot \cos(\omega \cdot t)\right)\right)^2 = R(t)$$

$$-A_1\ \omega^2\ \cos(\omega\ t) - A_2\ \omega^2\ \sin(\omega\ t) + \frac{f_0\left(-A_1\ \omega\ \sin(\omega\ t) + A_2\ \omega\ \cos(\omega\ t)\right)}{Q} \tag{4}$$

$$+ \left(f_0^2 - \frac{2\ \varepsilon_0\ S\ \left(V_{dc} + V_{ac}\ \cos(\omega\ t)\right)^2}{m_b\ g_0^3}\right)\left(A_1\ \cos(\omega\ t) + A_2\ \sin(\omega\ t)\right)$$

$$+ \beta_m\left(A_1\ \cos(\omega\ t) + A_2\ \sin(\omega\ t)\right)^3 - \frac{\varepsilon_0\ S\ \left(V_{dc} + V_{ac}\ \cos(\omega\ t)\right)^2}{m_b\ g_0^2} = R(t)$$

expand -A__1*omega^2*cos(omega*t)-A__2*omega^2*sin(omega*t)C f__0/Q*(-A__1*omega*sin(omega*t)C A__2*omega*cos

$$-A_1\ \omega^2\ \cos(\omega\ t) - A_2\ \omega^2\ \sin(\omega\ t) - \frac{f_0\ A_1\ \omega\ \sin(\omega\ t)}{Q} + \frac{f_0\ A_2\ \omega\ \cos(\omega\ t)}{Q} \tag{5}$$

$$+ f_0^2\ A_1\ \cos(\omega\ t) + f_0^2\ A_2\ \sin(\omega\ t) - \frac{2\ A_1\ \cos(\omega\ t)\ \varepsilon_0\ S\ V_{dc}^2}{m_b\ g_0^3}$$

124

Appendix

$$- \frac{2\,\varepsilon_0\,S\,V_{dc}^2\,A_2\,\sin(\omega\,t)}{m_b\,g_0^3} - \frac{4\,A_1\,\cos(\omega\,t)^2\,\varepsilon_0\,S\,V_{dc}\,V_{ac}}{m_b\,g_0^3}$$

$$- \frac{4\,\varepsilon_0\,S\,V_{dc}\,V_{ac}\,\cos(\omega\,t)\,A_2\,\sin(\omega\,t)}{m_b\,g_0^3} - \frac{2\,A_1\,\cos(\omega\,t)^3\,\varepsilon_0\,S\,V_{ac}^2}{m_b\,g_0^3}$$

$$- \frac{2\,\varepsilon_0\,S\,V_{ac}^2\,\cos(\omega\,t)^2\,A_2\,\sin(\omega\,t)}{m_b\,g_0^3} + \beta_m\,A_1^3\,\cos(\omega\,t)^3$$

$$+ 3\,\beta_m\,A_1^2\,\cos(\omega\,t)^2\,A_2\,\sin(\omega\,t) + 3\,\beta_m\,A_1\,\cos(\omega\,t)\,A_2^2\,\sin(\omega\,t)^2$$

$$+ \beta_m\,A_2^3\,\sin(\omega\,t)^3 - \frac{\varepsilon_0\,S\,V_{dc}^2}{m_b\,g_0^2} - \frac{2\,\varepsilon_0\,S\,V_{dc}\,V_{ac}\,\cos(\omega\,t)}{m_b\,g_0^2}$$

$$- \frac{\varepsilon_0\,S\,V_{ac}^2\,\cos(\omega\,t)^2}{m_b\,g_0^2} = R(t)$$

```
************************************
```
Here:
f_0 is resonance frequency,
Q is quality factor,
m_b is the effective mass of beam,
g_0 is gap from beam to gate,
ε_0 is premitivity of vacuum,
ω is angular frequency,
t is time,
S is cross-section area
```
************************************
```

Re-arrange the equation,

$$R(t) = -A_1\,\omega^2\,\cos(\omega\,t) - A_2\,\omega^2\,\sin(\omega\,t) - \frac{f_0\,A_1\,\omega\,\sin(\omega\,t)}{Q} + \frac{f_0\,A_2\,\omega\,\cos(\omega\,t)}{Q}$$

$$+ f_0^2\,A_1\,\cos(\omega\,t) + f_0^2\,A_2\,\sin(\omega\,t) - \frac{2\,A_1\,\cos(\omega\,t)\,\varepsilon_0\,S\,V_{dc}^2}{m_b\,g_0^3}$$

$$- \frac{2\,\varepsilon_0\,S\,V_{dc}^2\,A_2\,\sin(\omega\,t)}{m_b\,g_0^3} - \frac{4\,A_1\,\cos(\omega\,t)^2\,\varepsilon_0\,S\,V_{dc}\,V_{ac}}{m_b\,g_0^3}$$

$$- \frac{4\,\varepsilon_0\,S\,V_{dc}\,V_{ac}\,\cos(\omega\,t)\,A_2\,\sin(\omega\,t)}{m_b\,g_0^3} - \frac{2\,A_1\,\cos(\omega\,t)^3\,\varepsilon_0\,S\,V_{ac}^2}{m_b\,g_0^3}$$

$$- \frac{2\,\varepsilon_0\,S\,V_{ac}^2\,\cos(\omega\,t)^2\,A_2\,\sin(\omega\,t)}{m_b\,g_0^3} + \beta_m\,A_1^3\,\cos(\omega\,t)^3$$

$$+ 3\,\beta_m\,A_1^2\,\cos(\omega\,t)^2\,A_2\,\sin(\omega\,t) + 3\,\beta_m\,A_1\,\cos(\omega\,t)\,A_2^2\,\sin(\omega\,t)^2$$

$$+ \beta_m\,A_2^3\,\sin(\omega\,t)^3 - \frac{\varepsilon_0\,S\,V_{dc}^2}{m_b\,g_0^2} - \frac{2\,\varepsilon_0\,S\,V_{dc}\,V_{ac}\,\cos(\omega\,t)}{m_b\,g_0^2} - \frac{\varepsilon_0\,S\,V_{ac}^2\,\cos(\omega\,t)^2}{m_b\,g_0^2}$$

125

Appendix

$$R(t) = -A_1 \, \omega^2 \, \cos(\omega \, t) - A_2 \, \omega^2 \, \sin(\omega \, t) - \frac{f_0 \, A_1 \, \omega \, \sin(\omega \, t)}{Q} \tag{6}$$

$$+ \frac{f_0 \, A_2 \, \omega \, \cos(\omega \, t)}{Q} + f_0^2 \, A_1 \, \cos(\omega \, t) + f_0^2 \, A_2 \, \sin(\omega \, t)$$

$$- \frac{2 \, A_1 \, \cos(\omega \, t) \, \varepsilon_0 \, S \, V_{dc}^2}{m_b \, g_0^3} - \frac{2 \, \varepsilon_0 \, S \, V_{dc}^2 \, A_2 \, \sin(\omega \, t)}{m_b \, g_0^3}$$

$$- \frac{4 \, A_1 \, \cos(\omega \, t)^2 \, \varepsilon_0 \, S \, V_{dc} \, V_{ac}}{m_b \, g_0^3} - \frac{4 \, \varepsilon_0 \, S \, V_{dc} \, V_{ac} \, \cos(\omega \, t) \, A_2 \, \sin(\omega \, t)}{m_b \, g_0^3}$$

$$- \frac{2 \, A_1 \, \cos(\omega \, t)^3 \, \varepsilon_0 \, S \, V_{ac}^2}{m_b \, g_0^3} - \frac{2 \, \varepsilon_0 \, S \, V_{ac}^2 \, \cos(\omega \, t)^2 \, A_2 \, \sin(\omega \, t)}{m_b \, g_0^3}$$

$$+ \beta_m \, A_1^3 \, \cos(\omega \, t)^3 + 3 \, \beta_m \, A_1^2 \, \cos(\omega \, t)^2 \, A_2 \, \sin(\omega \, t)$$

$$+ 3 \, \beta_m \, A_1 \, \cos(\omega \, t) \, A_2^2 \, \sin(\omega \, t)^2 + \beta_m \, A_2^3 \, \sin(\omega \, t)^3 - \frac{\varepsilon_0 \, S \, V_{dc}^2}{m_b \, g_0^2}$$

$$- \frac{2 \, \varepsilon_0 \, S \, V_{dc} \, V_{ac} \, \cos(\omega \, t)}{m_b \, g_0^2} - \frac{\varepsilon_0 \, S \, V_{ac}^2 \, \cos(\omega \, t)^2}{m_b \, g_0^2}$$

We set up the initial condition: $y'(t)\big|_{t=0} = 0, \ y''(t)\big|_{t=0} = 0$

Then we have,

$$\frac{1}{T} \int_0^T y(t) R(\dot{y}, \ddot{y}, y, t) \, dt = 0$$

Combine with initial condition, we have,

$$\int_0^{\frac{2 \cdot \pi}{\omega}} \left(A_1 \cdot \cos(\omega \cdot t) + A_2 \cdot \sin(\omega \cdot t) \right) \cdot \left(-A_1 \, \omega^2 \, \cos(\omega \, t) - A_2 \, \omega^2 \, \sin(\omega \, t) \right.$$

$$- \frac{f_0 \, A_1 \, \omega \, \sin(\omega \, t)}{Q} + \frac{f_0 \, A_2 \, \omega \, \cos(\omega \, t)}{Q} + f_0^2 \, A_1 \, \cos(\omega \, t) + f_0^2 \, A_2 \, \sin(\omega \, t)$$

$$- \frac{2 \, A_1 \, \cos(\omega \, t) \, \varepsilon_0 \, S \, V_{dc}^2}{m_b \, g_0^3} - \frac{2 \, \varepsilon_0 \, S \, V_{dc}^2 \, A_2 \, \sin(\omega \, t)}{m_b \, g_0^3}$$

$$- \frac{4 \, A_1 \, \cos(\omega \, t)^2 \, \varepsilon_0 \, S \, V_{dc} \, V_{ac}}{m_b \, g_0^3} - \frac{4 \, \varepsilon_0 \, S \, V_{dc} \, V_{ac} \, \cos(\omega \, t) \, A_2 \, \sin(\omega \, t)}{m_b \, g_0^3}$$

$$- \frac{2 \, A_1 \, \cos(\omega \, t)^3 \, \varepsilon_0 \, S \, V_{ac}^2}{m_b \, g_0^3} - \frac{2 \, \varepsilon_0 \, S \, V_{ac}^2 \, \cos(\omega \, t)^2 \, A_2 \, \sin(\omega \, t)}{m_b \, g_0^3}$$

$$+ \beta_m \, A_1^3 \, \cos(\omega \, t)^3 + 3 \, \beta_m \, A_1^2 \, \cos(\omega \, t)^2 \, A_2 \, \sin(\omega \, t)$$

$$+ 3 \, \beta_m \, A_1 \, \cos(\omega \, t) \, A_2^2 \, \sin(\omega \, t)^2 + \beta_m \, A_2^3 \, \sin(\omega \, t)^3 - \frac{\varepsilon_0 \, S \, V_{dc}^2}{m_b \, g_0^2}$$

$$\left. - \frac{2 \, \varepsilon_0 \, S \, V_{dc} \, V_{ac} \, \cos(\omega \, t)}{m_b \, g_0^2} - \frac{\varepsilon_0 \, S \, V_{ac}^2 \, \cos(\omega \, t)^2}{m_b \, g_0^2} \right) \, dt = 0$$

Appendix

$$\frac{1}{4\,\omega\,m_b\,g_0^{\,3}}\Big(\pi\,\Big(3\,A_1^{\,4}\,\beta_m\,g_0^{\,3}\,m_b + 6\,A_1^{\,2}\,A_2^{\,2}\,\beta_m\,g_0^{\,3}\,m_b + 3\,A_2^{\,4}\,\beta_m\,g_0^{\,3}\,m_b \qquad (7)$$

$$+\,4\,A_1^{\,2}\,f_0^{\,2}\,g_0^{\,3}\,m_b - 4\,A_1^{\,2}\,g_0^{\,3}\,m_b\,\omega^2 + 4\,A_2^{\,2}\,f_0^{\,2}\,g_0^{\,3}\,m_b - 4\,A_2^{\,2}\,g_0^{\,3}\,m_b\,\omega^2$$

$$-\,6\,A_1^{\,2}\,S\,V_{ac}^{\,2}\,\varepsilon_0 - 8\,A_1^{\,2}\,S\,V_{dc}^{\,2}\,\varepsilon_0 - 8\,\varepsilon_0\,S\,A_1\,g_0\,V_{ac}\,V_{dc} - 2\,A_2^{\,2}\,S\,V_{ac}^{\,2}\,\varepsilon_0$$

$$-\,8\,A_2^{\,2}\,S\,V_{dc}^{\,2}\,\varepsilon_0\Big)\Big) = 0$$

$$\rightarrow$$

$$\frac{1}{\omega}\Bigg(-A_1^{\,2}\,\omega^2\,\left(\frac{\sin(\omega\,t)\,\cos(\omega\,t)}{2} + \frac{\omega\,t}{2}\right) + A_2^{\,2}\,f_0^{\,2}\,\left(-\frac{\sin(\omega\,t)\,\cos(\omega\,t)}{2}\right. \qquad (8)$$

$$\left.+\,\frac{\omega\,t}{2}\right) + A_1^{\,2}\,f_0^{\,2}\,\left(\frac{\sin(\omega\,t)\,\cos(\omega\,t)}{2} + \frac{\omega\,t}{2}\right) + A_2^{\,4}\,\beta_m\,\Bigg($$

$$-\frac{\left(\sin(\omega\,t)^3 + \frac{3\,\sin(\omega\,t)}{2}\right)\cos(\omega\,t)}{4} + \frac{3\,\omega\,t}{8}\Bigg)$$

$$+\,\beta_m\,A_1^{\,4}\,\left(\frac{\left(\cos(\omega\,t)^3 + \frac{3\,\cos(\omega\,t)}{2}\right)\sin(\omega\,t)}{4} + \frac{3\,\omega\,t}{8}\right) - A_2^{\,2}\,\omega^2\,\Bigg($$

$$-\frac{\sin(\omega\,t)\,\cos(\omega\,t)}{2} + \frac{\omega\,t}{2}\Bigg) + \frac{A_1\,f_0\,A_2\,\omega\,\left(\frac{\sin(\omega\,t)\,\cos(\omega\,t)}{2} + \frac{\omega\,t}{2}\right)}{Q}$$

$$+\,\frac{8\,A_1\,A_2\,S\,V_{ac}\,V_{dc}\,\varepsilon_0\,\cos(\omega\,t)^3}{3\,m_b\,g_0^{\,3}}$$

$$-\,\frac{A_1\,f_0\,A_2\,\omega\,\left(-\frac{\sin(\omega\,t)\,\cos(\omega\,t)}{2} + \frac{\omega\,t}{2}\right)}{Q} - \frac{A_2^{\,2}\,f_0\,\omega\,\cos(\omega\,t)^2}{2\,Q}$$

$$+\,\frac{A_1^{\,2}\,f_0\,\omega\,\cos(\omega\,t)^2}{2\,Q} - \frac{4\,A_1^{\,2}\,S\,V_{ac}\,V_{dc}\,\varepsilon_0\,\left(2 + \cos(\omega\,t)^2\right)\sin(\omega\,t)}{3\,m_b\,g_0^{\,3}}$$

$$-\,\frac{2\,A_1\,S\,V_{ac}\,V_{dc}\,\varepsilon_0\,\left(\frac{\sin(\omega\,t)\,\cos(\omega\,t)}{2} + \frac{\omega\,t}{2}\right)}{m_b\,g_0^{\,2}}$$

$$-\,\frac{A_1\,S\,V_{ac}^{\,2}\,\varepsilon_0\,\left(2 + \cos(\omega\,t)^2\right)\sin(\omega\,t)}{3\,m_b\,g_0^{\,2}} - \frac{4\,A_2^{\,2}\,S\,V_{ac}\,V_{dc}\,\varepsilon_0\,\sin(\omega\,t)^3}{3\,m_b\,g_0^{\,3}}$$

$$+ \frac{2\,A_1\,A_2\,S\,V_{dc}^{\;2}\,\varepsilon_0\,\cos(\omega\,t)^2}{m_b\,g_0^{\;3}} + \frac{A_2\,S\,V_{ac}\,V_{dc}\,\varepsilon_0\,\cos(\omega\,t)^2}{m_b\,g_0^{\;2}}$$

$$+ \frac{A_1\,A_2\,S\,V_{ac}^{\;2}\,\varepsilon_0\,\cos(\omega\,t)^4}{m_b\,g_0^{\;3}} - A_1^{\;3}\,A_2\,\beta_m\,\cos(\omega\,t)^4 + 6\,A_1^{\;2}\,A_2^{\;2}\,\beta_m\,\Bigg($$

$$- \frac{\sin(\omega\,t)\,\cos(\omega\,t)^3}{4} + \frac{\sin(\omega\,t)\,\cos(\omega\,t)}{8} + \frac{\omega\,t}{8}\Bigg) + A_1\,A_2^{\;3}\,\beta_m\,\sin(\omega\,t)^4$$

$$+ A_1\,A_2\,\omega^2\,\cos(\omega\,t)^2 - A_1\,f_0^{\;2}\,A_2\,\cos(\omega\,t)^2 + \frac{A_2\,S\,V_{dc}^{\;2}\,\varepsilon_0\,\cos(\omega\,t)}{m_b\,g_0^{\;2}}$$

$$+ \frac{A_2\,S\,V_{ac}^{\;2}\,\varepsilon_0\,\cos(\omega\,t)^3}{3\,m_b\,g_0^{\;2}} - \frac{A_1\,S\,V_{dc}^{\;2}\,\varepsilon_0\,\sin(\omega\,t)}{m_b\,g_0^{\;2}}$$

$$- \frac{2\,A_2^{\;2}\,S\,V_{ac}^{\;2}\,\varepsilon_0\,\left(- \dfrac{\sin(\omega\,t)\,\cos(\omega\,t)^3}{4} + \dfrac{\sin(\omega\,t)\,\cos(\omega\,t)}{8} + \dfrac{\omega\,t}{8}\right)}{m_b\,g_0^{\;3}}$$

$$- \frac{2\,A_1^{\;2}\,S\,V_{ac}^{\;2}\,\varepsilon_0\,\left(\dfrac{\left(\cos(\omega\,t)^3 + \dfrac{3\,\cos(\omega\,t)}{2}\right)\,\sin(\omega\,t)}{4} + \dfrac{3\,\omega\,t}{8}\right)}{m_b\,g_0^{\;3}}$$

$$- \frac{2\,A_1^{\;2}\,S\,V_{dc}^{\;2}\,\varepsilon_0\,\left(\dfrac{\sin(\omega\,t)\,\cos(\omega\,t)}{2} + \dfrac{\omega\,t}{2}\right)}{m_b\,g_0^{\;3}}$$

$$- \frac{2\,A_2^{\;2}\,S\,V_{dc}^{\;2}\,\varepsilon_0\,\left(- \dfrac{\sin(\omega\,t)\,\cos(\omega\,t)}{2} + \dfrac{\omega\,t}{2}\right)}{m_b\,g_0^{\;3}}\Bigg) = 0$$

$$\lim_{t \to \frac{2\cdot\pi}{\omega}} \Bigg(\frac{1}{\omega}\Bigg(- A_1^{\;2}\,\omega^2\,\left(\frac{\sin(\omega\,t)\,\cos(\omega\,t)}{2} + \frac{\omega\,t}{2}\right) + A_2^{\;2}\,f_0^{\;2}\,\left(- \frac{\sin(\omega\,t)\,\cos(\omega\,t)}{2}\right.$$

$$\left. + \frac{\omega\,t}{2}\right) + A_1^{\;2}\,f_0^{\;2}\,\left(\frac{\sin(\omega\,t)\,\cos(\omega\,t)}{2} + \frac{\omega\,t}{2}\right) + A_2^{\;4}\,\beta_m\,\Bigg($$

$$- \frac{\left(\sin(\omega\,t)^3 + \dfrac{3\,\sin(\omega\,t)}{2}\right)\,\cos(\omega\,t)}{4} + \frac{3\,\omega\,t}{8}\Bigg)$$

$$+ \beta_m A_1^4 \left(\frac{\left(\cos(\omega\ t)^3 + \frac{3\ \cos(\omega\ t)}{2} \right)\ \sin(\omega\ t)}{4} + \frac{3\ \omega\ t}{8} \right) - A_2^2\ \omega^2 \left(\vphantom{\frac{a}{b}} \right.$$

$$\left. - \frac{\sin(\omega\ t)\ \cos(\omega\ t)}{2} + \frac{\omega\ t}{2} \right) + \frac{A_1\ f_0\ A_2\ \omega \left(\frac{\sin(\omega\ t)\ \cos(\omega\ t)}{2} + \frac{\omega\ t}{2} \right)}{Q}$$

$$+ \frac{8\ A_1\ A_2\ S\ V_{ac}\ V_{dc}\ \varepsilon_0\ \cos(\omega\ t)^3}{3\ m_b\ g_0^3} - \frac{A_1\ f_0\ A_2\ \omega \left(- \frac{\sin(\omega\ t)\ \cos(\omega\ t)}{2} + \frac{\omega\ t}{2} \right)}{Q}$$

$$- \frac{A_2^2\ f_0\ \omega\ \cos(\omega\ t)^2}{2\ Q} + \frac{A_1^2\ f_0\ \omega\ \cos(\omega\ t)^2}{2\ Q}$$

$$- \frac{4\ A_1^2\ S\ V_{ac}\ V_{dc}\ \varepsilon_0\ \left(2 + \cos(\omega\ t)^2 \right)\ \sin(\omega\ t)}{3\ m_b\ g_0^3}$$

$$- \frac{2\ A_1\ S\ V_{ac}\ V_{dc}\ \varepsilon_0 \left(\frac{\sin(\omega\ t)\ \cos(\omega\ t)}{2} + \frac{\omega\ t}{2} \right)}{m_b\ g_0^2}$$

$$+ A_1\ A_2\ \omega^2\ \cos(\omega\ t)^2 - A_1\ f_0^2\ A_2\ \cos(\omega\ t)^2 + \frac{A_2\ S\ V_{dc}^2\ \varepsilon_0\ \cos(\omega\ t)}{m_b\ g_0^2}$$

$$+ \frac{A_2\ S\ V_{ac}^2\ \varepsilon_0\ \cos(\omega\ t)^3}{3\ m_b\ g_0^2} - \frac{A_1\ S\ V_{dc}^2\ \varepsilon_0\ \sin(\omega\ t)}{m_b\ g_0^2}$$

$$- \frac{2\ A_2^2\ S\ V_{ac}^2\ \varepsilon_0 \left(- \frac{\sin(\omega\ t)\ \cos(\omega\ t)^3}{4} + \frac{\sin(\omega\ t)\ \cos(\omega\ t)}{8} + \frac{\omega\ t}{8} \right)}{m_b\ g_0^3}$$

$$- \frac{2\ A_1^2\ S\ V_{ac}^2\ \varepsilon_0 \left(\frac{\left(\cos(\omega\ t)^3 + \frac{3\ \cos(\omega\ t)}{2} \right)\ \sin(\omega\ t)}{4} + \frac{3\ \omega\ t}{8} \right)}{m_b\ g_0^3}$$

$$- \frac{2\ A_1^2\ S\ V_{dc}^2\ \varepsilon_0 \left(\frac{\sin(\omega\ t)\ \cos(\omega\ t)}{2} + \frac{\omega\ t}{2} \right)}{m_b\ g_0^3}$$

Appendix

$$+ \frac{A_2\ S\ V_{ac}^{\ 2}\ \varepsilon_0\ \cos(\omega\ t)^3}{3\ m_b\ g_0^{\ 2}} - \frac{A_1\ S\ V_{dc}^{\ 2}\ \varepsilon_0\ \sin(\omega\ t)}{m_b\ g_0^{\ 2}}$$

$$- \frac{2\ A_2^{\ 2}\ S\ V_{ac}^{\ 2}\ \varepsilon_0\ \left(-\dfrac{\sin(\omega\ t)\ \cos(\omega\ t)^3}{4} + \dfrac{\sin(\omega\ t)\ \cos(\omega\ t)}{8} + \dfrac{\omega\ t}{8} \right)}{m_b\ g_0^{\ 3}}$$

$$- \frac{2\ A_1^{\ 2}\ S\ V_{ac}^{\ 2}\ \varepsilon_0\ \left(\dfrac{\left(\cos(\omega\ t)^3 + \dfrac{3\ \cos(\omega\ t)}{2} \right)\ \sin(\omega\ t)}{4} + \dfrac{3\ \omega\ t}{8} \right)}{m_b\ g_0^{\ 3}}$$

$$- \frac{2\ A_1^{\ 2}\ S\ V_{dc}^{\ 2}\ \varepsilon_0\ \left(\dfrac{\sin(\omega\ t)\ \cos(\omega\ t)}{2} + \dfrac{\omega\ t}{2} \right)}{m_b\ g_0^{\ 3}}$$

$$\left. \left. - \frac{2\ A_2^{\ 2}\ S\ V_{dc}^{\ 2}\ \varepsilon_0\ \left(-\dfrac{\sin(\omega\ t)\ \cos(\omega\ t)}{2} + \dfrac{\omega\ t}{2} \right)}{m_b\ g_0^{\ 3}} \right) \right) = 0$$

$$\frac{1}{12\ m_b\ g_0^{\ 3}\ \omega\ Q} \left(9\ A_1^{\ 4}\ \pi\ Q\ \beta_m\ g_0^{\ 3}\ m_b + 18\ A_1^{\ 2}\ A_2^{\ 2}\ \pi\ Q\ \beta_m\ g_0^{\ 3}\ m_b \right. \qquad (9)$$

$$+ 9\ A_2^{\ 4}\ \pi\ Q\ \beta_m\ g_0^{\ 3}\ m_b - 12\ A_1^{\ 3}\ A_2\ Q\ \beta_m\ g_0^{\ 3}\ m_b + 12\ A_1^{\ 2}\ \pi\ Q\ f_0^{\ 2}\ g_0^{\ 3}\ m_b$$

$$- 12\ A_1^{\ 2}\ \pi\ Q\ g_0^{\ 3}\ m_b\ \omega^2 + 12\ A_2^{\ 2}\ \pi\ Q\ f_0^{\ 2}\ g_0^{\ 3}\ m_b - 12\ A_2^{\ 2}\ \pi\ Q\ g_0^{\ 3}\ m_b\ \omega^2$$

$$- 12\ A_1\ A_2\ Q\ f_0^{\ 2}\ g_0^{\ 3}\ m_b + 12\ A_1\ A_2\ Q\ g_0^{\ 3}\ m_b\ \omega^2 - 18\ A_1^{\ 2}\ \pi\ Q\ S\ V_{ac}^{\ 2}\ \varepsilon_0$$

$$- 24\ A_1^{\ 2}\ \pi\ Q\ S\ V_{dc}^{\ 2}\ \varepsilon_0 + 6\ A_1^{\ 2}\ f_0\ g_0^{\ 3}\ m_b\ \omega - 24\ A_1\ \pi\ Q\ S\ V_{ac}\ V_{dc}\ g_0\ \varepsilon_0$$

$$- 6\ A_2^{\ 2}\ \pi\ Q\ S\ V_{ac}^{\ 2}\ \varepsilon_0 - 24\ A_2^{\ 2}\ \pi\ Q\ S\ V_{dc}^{\ 2}\ \varepsilon_0 - 6\ A_2^{\ 2}\ f_0\ g_0^{\ 3}\ m_b\ \omega$$

$$+ 12\ A_1\ A_2\ Q\ S\ V_{ac}^{\ 2}\ \varepsilon_0 + 32\ A_1\ A_2\ S\ V_{ac}\ V_{dc}\ \varepsilon_0\ Q + 24\ A_1\ A_2\ Q\ S\ V_{dc}^{\ 2}\ \varepsilon_0$$

$$\left. + 4\ A_2\ S\ V_{ac}^{\ 2}\ \varepsilon_0\ g_0\ Q + 12\ A_2\ Q\ S\ V_{ac}\ V_{dc}\ g_0\ \varepsilon_0 + 12\ A_2\ Q\ S\ V_{dc}^{\ 2}\ g_0\ \varepsilon_0 \right) = 0$$

Re-arrange the equation (9):

$$\frac{1}{12\ m_b\ g_0^{\ 3}\ \omega\ Q} \left(9\ A_1^{\ 4}\ \pi\ Q\ \beta_m\ g_0^{\ 3}\ m_b + 18\ A_1^{\ 2}\ A_2^{\ 2}\ \pi\ Q\ \beta_m\ g_0^{\ 3}\ m_b + 9\ A_2^{\ 4}\ \pi\ Q\ \beta_m\ g_0^{\ 3}\ m_b \right.$$

$$- 12\ A_1^{\ 3}\ A_2\ Q\ \beta_m\ g_0^{\ 3}\ m_b + 12\ A_1^{\ 2}\ \pi\ Q\ f_0^{\ 2}\ g_0^{\ 3}\ m_b - 12\ A_1^{\ 2}\ \pi\ Q\ g_0^{\ 3}\ m_b\ \omega^2$$

$$+ 12\ A_2^{\ 2}\ \pi\ Q\ f_0^{\ 2}\ g_0^{\ 3}\ m_b - 12\ A_2^{\ 2}\ \pi\ Q\ g_0^{\ 3}\ m_b\ \omega^2 - 12\ A_1\ A_2\ Q\ f_0^{\ 2}\ g_0^{\ 3}\ m_b$$

$$+ 12\ A_1\ A_2\ Q\ g_0^{\ 3}\ m_b\ \omega^2 - 18\ A_1^{\ 2}\ \pi\ Q\ S\ V_{ac}^{\ 2}\ \varepsilon_0 - 24\ A_1^{\ 2}\ \pi\ Q\ S\ V_{dc}^{\ 2}\ \varepsilon_0$$

$$+ 6\ A_1^{\ 2}\ f_0\ g_0^{\ 3}\ m_b\ \omega - 24\ A_1\ \pi\ Q\ S\ V_{ac}\ V_{dc}\ g_0\ \varepsilon_0 - 6\ A_2^{\ 2}\ \pi\ Q\ S\ V_{ac}^{\ 2}\ \varepsilon_0$$

$$- 24\ A_2^{\ 2}\ \pi\ Q\ S\ V_{dc}^{\ 2}\ \varepsilon_0 - 6\ A_2^{\ 2}\ f_0\ g_0^{\ 3}\ m_b\ \omega + 12\ A_1\ A_2\ Q\ S\ V_{ac}^{\ 2}\ \varepsilon_0$$

$$+ 32\ A_1\ A_2\ S\ V_{ac}\ V_{dc}\ \varepsilon_0\ Q + 24\ A_1\ A_2\ Q\ S\ V_{dc}^{\ 2}\ \varepsilon_0 + 4\ A_2\ S\ V_{ac}^{\ 2}\ \varepsilon_0\ g_0\ Q$$

$$\left. + 12\ A_2\ Q\ S\ V_{ac}\ V_{dc}\ g_0\ \varepsilon_0 + 12\ A_2\ Q\ S\ V_{dc}^{\ 2}\ g_0\ \varepsilon_0 \right) = 0$$

$$\frac{1}{12\,m_b\,g_0^{\,3}\,\omega\,Q}\Big(9\,A_1^{\,4}\,\pi\,Q\,\beta_m\,g_0^{\,3}\,m_b + 18\,A_1^{\,2}\,A_2^{\,2}\,\pi\,Q\,\beta_m\,g_0^{\,3}\,m_b \tag{10}$$

$$+\,9\,A_2^{\,4}\,\pi\,Q\,\beta_m\,g_0^{\,3}\,m_b - 12\,A_1^{\,3}\,A_2\,Q\,\beta_m\,g_0^{\,3}\,m_b + 12\,A_1^{\,2}\,\pi\,Q\,f_0^{\,2}\,g_0^{\,3}\,m_b$$

$$-\,12\,A_1^{\,2}\,\pi\,Q\,g_0^{\,3}\,m_b\,\omega^2 + 12\,A_2^{\,2}\,\pi\,Q\,f_0^{\,2}\,g_0^{\,3}\,m_b - 12\,A_2^{\,2}\,\pi\,Q\,g_0^{\,3}\,m_b\,\omega^2$$

$$-\,12\,A_1\,A_2\,Q\,f_0^{\,2}\,g_0^{\,3}\,m_b + 12\,A_1\,A_2\,Q\,g_0^{\,3}\,m_b\,\omega^2 - 18\,A_1^{\,2}\,\pi\,Q\,S\,V_{ac}^{\,2}\,\varepsilon_0$$

$$-\,24\,A_1^{\,2}\,\pi\,Q\,S\,V_{dc}^{\,2}\,\varepsilon_0 + 6\,A_1^{\,2}\,f_0\,g_0^{\,3}\,m_b\,\omega - 24\,A_1\,\pi\,Q\,S\,V_{ac}\,V_{dc}\,g_0\,\varepsilon_0$$

$$-\,6\,A_2^{\,2}\,\pi\,Q\,S\,V_{ac}^{\,2}\,\varepsilon_0 - 24\,A_2^{\,2}\,\pi\,Q\,S\,V_{dc}^{\,2}\,\varepsilon_0 - 6\,A_2^{\,2}\,f_0\,g_0^{\,3}\,m_b\,\omega$$

$$+\,12\,A_1\,A_2\,Q\,S\,V_{ac}^{\,2}\,\varepsilon_0 + 32\,A_1\,A_2\,S\,V_{ac}\,V_{dc}\,\varepsilon_0\,Q + 24\,A_1\,A_2\,Q\,S\,V_{dc}^{\,2}\,\varepsilon_0$$

$$+\,4\,A_2\,S\,V_{ac}^{\,2}\,\varepsilon_0\,g_0\,Q + 12\,A_2\,Q\,S\,V_{ac}\,V_{dc}\,g_0\,\varepsilon_0 + 12\,A_2\,Q\,S\,V_{dc}^{\,2}\,g_0\,\varepsilon_0\Big)=0$$

$$\rightarrow$$

$$9\,A_1^{\,4}\,\pi\,Q\,\beta_m\,g_0^{\,3}\,m_b + 18\,A_1^{\,2}\,A_2^{\,2}\,\pi\,Q\,\beta_m\,g_0^{\,3}\,m_b + 9\,A_2^{\,4}\,\pi\,Q\,\beta_m\,g_0^{\,3}\,m_b$$

$$-\,12\,A_1^{\,3}\,A_2\,Q\,\beta_m\,g_0^{\,3}\,m_b + 12\,A_1^{\,2}\,\pi\,Q\,f_0^{\,2}\,g_0^{\,3}\,m_b - 12\,A_1^{\,2}\,\pi\,Q\,g_0^{\,3}\,m_b\,\omega^2$$

$$+\,12\,A_2^{\,2}\,\pi\,Q\,f_0^{\,2}\,g_0^{\,3}\,m_b - 12\,A_2^{\,2}\,\pi\,Q\,g_0^{\,3}\,m_b\,\omega^2 - 12\,A_1\,A_2\,Q\,f_0^{\,2}\,g_0^{\,3}\,m_b$$

$$+\,12\,A_1\,A_2\,Q\,g_0^{\,3}\,m_b\,\omega^2 - 18\,A_1^{\,2}\,\pi\,Q\,S\,V_{ac}^{\,2}\,\varepsilon_0 - 24\,A_1^{\,2}\,\pi\,Q\,S\,V_{dc}^{\,2}\,\varepsilon_0$$

$$+\,6\,A_1^{\,2}\,f_0\,g_0^{\,3}\,m_b\,\omega - 24\,A_1\,\pi\,Q\,S\,V_{ac}\,V_{dc}\,g_0\,\varepsilon_0 - 6\,A_2^{\,2}\,\pi\,Q\,S\,V_{ac}^{\,2}\,\varepsilon_0$$

$$-\,24\,A_2^{\,2}\,\pi\,Q\,S\,V_{dc}^{\,2}\,\varepsilon_0 - 6\,A_2^{\,2}\,f_0\,g_0^{\,3}\,m_b\,\omega + 12\,A_1\,A_2\,Q\,S\,V_{ac}^{\,2}\,\varepsilon_0$$

$$+\,32\,A_1\,A_2\,S\,V_{ac}\,V_{dc}\,\varepsilon_0\,Q + 24\,A_1\,A_2\,Q\,S\,V_{dc}^{\,2}\,\varepsilon_0 + 4\,A_2\,S\,V_{ac}^{\,2}\,\varepsilon_0\,g_0\,Q$$

$$+\,12\,A_2\,Q\,S\,V_{ac}\,V_{dc}\,g_0\,\varepsilon_0 + 12\,A_2\,Q\,S\,V_{dc}^{\,2}\,g_0\,\varepsilon_0 = 0$$

$$9\,A_1^{\,4}\,\pi\,Q\,\beta_m\,g_0^{\,3}\,m_b + 18\,A_1^{\,2}\,A_2^{\,2}\,\pi\,Q\,\beta_m\,g_0^{\,3}\,m_b + 9\,A_2^{\,4}\,\pi\,Q\,\beta_m\,g_0^{\,3}\,m_b$$

$$-\,12\,A_1^{\,3}\,A_2\,Q\,\beta_m\,g_0^{\,3}\,m_b + 12\,A_1^{\,2}\,\pi\,Q\,f_0^{\,2}\,g_0^{\,3}\,m_b - 12\,A_1^{\,2}\,\pi\,Q\,g_0^{\,3}\,m_b\,\omega^2$$

$$+\,12\,A_2^{\,2}\,\pi\,Q\,f_0^{\,2}\,g_0^{\,3}\,m_b - 12\,A_2^{\,2}\,\pi\,Q\,g_0^{\,3}\,m_b\,\omega^2 - 12\,A_1\,A_2\,Q\,f_0^{\,2}\,g_0^{\,3}\,m_b$$

$$+\,12\,A_1\,A_2\,Q\,g_0^{\,3}\,m_b\,\omega^2 - 18\,A_1^{\,2}\,\pi\,Q\,S\,V_{ac}^{\,2}\,\varepsilon_0 - 24\,A_1^{\,2}\,\pi\,Q\,S\,V_{dc}^{\,2}\,\varepsilon_0$$

$$+\,6\,A_1^{\,2}\,f_0\,g_0^{\,3}\,m_b\,\omega - 24\,A_1\,\pi\,Q\,S\,V_{ac}\,V_{dc}\,g_0\,\varepsilon_0 - 6\,A_2^{\,2}\,\pi\,Q\,S\,V_{ac}^{\,2}\,\varepsilon_0$$

$$-\,24\,A_2^{\,2}\,\pi\,Q\,S\,V_{dc}^{\,2}\,\varepsilon_0 - 6\,A_2^{\,2}\,f_0\,g_0^{\,3}\,m_b\,\omega + 12\,A_1\,A_2\,Q\,S\,V_{ac}^{\,2}\,\varepsilon_0$$

$$+\,32\,A_1\,A_2\,S\,V_{ac}\,V_{dc}\,\varepsilon_0\,Q + 24\,A_1\,A_2\,Q\,S\,V_{dc}^{\,2}\,\varepsilon_0 + 4\,A_2\,S\,V_{ac}^{\,2}\,\varepsilon_0\,g_0\,Q$$

$$+\,12\,A_2\,Q\,S\,V_{ac}\,V_{dc}\,g_0\,\varepsilon_0 + 12\,A_2\,Q\,S\,V_{dc}^{\,2}\,g_0\,\varepsilon_0 = 0$$

$$9\,A_1^{\,4}\,\pi\,Q\,\beta_m\,g_0^{\,3}\,m_b + 18\,A_1^{\,2}\,A_2^{\,2}\,\pi\,Q\,\beta_m\,g_0^{\,3}\,m_b + 9\,A_2^{\,4}\,\pi\,Q\,\beta_m\,g_0^{\,3}\,m_b \tag{11}$$

$$-\,12\,A_1^{\,3}\,A_2\,Q\,\beta_m\,g_0^{\,3}\,m_b + 12\,A_1^{\,2}\,\pi\,Q\,f_0^{\,2}\,g_0^{\,3}\,m_b - 12\,A_1^{\,2}\,\pi\,Q\,g_0^{\,3}\,m_b\,\omega^2$$

$$+\,12\,A_2^{\,2}\,\pi\,Q\,f_0^{\,2}\,g_0^{\,3}\,m_b - 12\,A_2^{\,2}\,\pi\,Q\,g_0^{\,3}\,m_b\,\omega^2 - 12\,A_1\,A_2\,Q\,f_0^{\,2}\,g_0^{\,3}\,m_b$$

$$+\,12\,A_1\,A_2\,Q\,g_0^{\,3}\,m_b\,\omega^2 - 18\,A_1^{\,2}\,\pi\,Q\,S\,V_{ac}^{\,2}\,\varepsilon_0 - 24\,A_1^{\,2}\,\pi\,Q\,S\,V_{dc}^{\,2}\,\varepsilon_0$$

$$+\,6\,A_1^{\,2}\,f_0\,g_0^{\,3}\,m_b\,\omega - 24\,A_1\,\pi\,Q\,S\,V_{ac}\,V_{dc}\,g_0\,\varepsilon_0 - 6\,A_2^{\,2}\,\pi\,Q\,S\,V_{ac}^{\,2}\,\varepsilon_0$$

$$-\,24\,A_2^{\,2}\,\pi\,Q\,S\,V_{dc}^{\,2}\,\varepsilon_0 - 6\,A_2^{\,2}\,f_0\,g_0^{\,3}\,m_b\,\omega + 12\,A_1\,A_2\,Q\,S\,V_{ac}^{\,2}\,\varepsilon_0$$

$$+\,32\,A_1\,A_2\,S\,V_{ac}\,V_{dc}\,\varepsilon_0\,Q + 24\,A_1\,A_2\,Q\,S\,V_{dc}^{\,2}\,\varepsilon_0 + 4\,A_2\,S\,V_{ac}^{\,2}\,\varepsilon_0\,g_0\,Q$$

$$+\,12\,A_2\,Q\,S\,V_{ac}\,V_{dc}\,g_0\,\varepsilon_0 + 12\,A_2\,Q\,S\,V_{dc}^{\,2}\,g_0\,\varepsilon_0 = 0$$

$$=$$

Appendix

$$\left(9\, A_2^{\,4}\, \pi\, \beta_m\, g_0^{\,3}\, m_b - 24\,\pi \left(\frac{m_b \left(-\dfrac{3\,\beta_m\, A_1^{\,2}}{2} + \omega^2 - f_0^{\,2} \right) g_0^{\,3}}{2} + S\,\varepsilon_0 \left(V_{dc}^{\,2} \right.\right.\right. \tag{12}$$

$$\left.\left.\left. + \frac{V_{ac}^{\,2}}{4} \right) \right) A_2^{\,2} + \left(12\, A_1\, m_b \left(-\beta_m\, A_1^{\,2} - f_0^{\,2} + \omega^2 \right) g_0^{\,3} + 12 \left(V_{dc}^{\,2} + V_{dc}\, V_{ac} \right.\right.\right.$$

$$\left.\left. + \frac{1}{3}\, V_{ac}^{\,2} \right) \varepsilon_0\, S\, g_0 + 24\,\varepsilon_0\, A_1\, S \left(V_{dc}^{\,2} + \frac{4}{3}\, V_{dc}\, V_{ac} + \frac{1}{2}\, V_{ac}^{\,2} \right) \right) A_2$$

$$- 24\,\pi\, A_1 \left(\frac{\left(-\dfrac{3\,\beta_m\, A_1^{\,2}}{4} + \omega^2 - f_0^{\,2} \right) m_b\, A_1\, g_0^{\,3}}{2} + S\, V_{ac}\, V_{dc}\, g_0\, \varepsilon_0 + A_1 \left(V_{dc}^{\,2} \right.\right.$$

$$\left.\left.\left. + \frac{3\, V_{ac}^{\,2}}{4} \right) S\,\varepsilon_0 \right) \right) Q + 6\,\omega\, f_0\, g_0^{\,3}\, m_b \left(A_1 - A_2 \right)\left(A_1 + A_2 \right) = 0$$

Hence the final equation with A_1 and A_2 is,

$$\left(9\, A_2^{\,4}\, \pi\, \beta_m\, g_0^{\,3}\, m_b - 24\,\pi \left(\frac{m_b \left(-\dfrac{3\,\beta_m\, A_1^{\,2}}{2} + 4\,\pi^2\, f^2 - f_0^{\,2} \right) g_0^{\,3}}{2} + S\,\varepsilon_0 \left(V_{dc}^{\,2} \right.\right.\right.$$

$$\left.\left.\left. + \frac{V_{ac}^{\,2}}{4} \right) \right) A_2^{\,2} + \left(12\, A_1\, m_b \left(4\,\pi^2\, f^2 - \beta_m\, A_1^{\,2} - f_0^{\,2} \right) g_0^{\,3} + 12 \left(V_{dc}^{\,2} + V_{dc}\, V_{ac} \right.\right.\right.$$

$$\left.\left. + \frac{1}{3}\, V_{ac}^{\,2} \right) \varepsilon_0\, S\, g_0 + 24\,\varepsilon_0\, A_1\, S \left(V_{dc}^{\,2} + \frac{4}{3}\, V_{dc}\, V_{ac} + \frac{1}{2}\, V_{ac}^{\,2} \right) \right) A_2$$

$$- 24\,\pi\, A_1 \left(\frac{\left(-\dfrac{3\,\beta_m\, A_1^{\,2}}{4} + 4\,\pi^2\, f^2 - f_0^{\,2} \right) m_b\, A_1\, g_0^{\,3}}{2} + S\, V_{ac}\, V_{dc}\, g_0\, \varepsilon_0 + A_1 \left(V_{dc}^{\,2} \right.\right.$$

$$\left.\left.\left. + \frac{3\, V_{ac}^{\,2}}{4} \right) S\,\varepsilon_0 \right) \right) Q + 12\,\pi\, f\, f_0\, g_0^{\,3}\, m_b \left(A_1 - A_2 \right)\left(A_1 + A_2 \right) = 0$$

$$\left(9\, A_2^{\,4}\, \pi\, \beta_m\, g_0^{\,3}\, m_b - 24\,\pi \left(\frac{m_b \left(-\dfrac{3\,\beta_m\, A_1^{\,2}}{2} + 4\,\pi^2\, f^2 - f_0^{\,2} \right) g_0^{\,3}}{2} + S\,\varepsilon_0 \left(V_{dc}^{\,2} \right.\right.\right. \tag{13}$$

$$\left.\left.\left. + \frac{V_{ac}^{\,2}}{4} \right) \right) A_2^{\,2} + \left(12\, A_1\, m_b \left(4\,\pi^2\, f^2 - \beta_m\, A_1^{\,2} - f_0^{\,2} \right) g_0^{\,3} + 12 \left(V_{dc}^{\,2} + V_{dc}\, V_{ac} \right.\right.\right.$$

$$\left.\left. + \frac{1}{3}\, V_{ac}^{\,2} \right) \varepsilon_0\, S\, g_0 + 24\,\varepsilon_0\, A_1\, S \left(V_{dc}^{\,2} + \frac{4}{3}\, V_{dc}\, V_{ac} + \frac{1}{2}\, V_{ac}^{\,2} \right) \right) A_2$$

$$- 24\,\pi\, A_1 \left(\frac{\left(-\dfrac{3\,\beta_m\, A_1^{\,2}}{4} + 4\,\pi^2\, f^2 - f_0^{\,2} \right) m_b\, A_1\, g_0^{\,3}}{2} + S\, V_{ac}\, V_{dc}\, g_0\, \varepsilon_0 \right.$$

$$\left.\left. + A_1 \left(V_{dc}^{\,2} + \frac{3\, V_{ac}^{\,2}}{4} \right) S\,\varepsilon_0 \right) \right) Q + 12\,\pi\, f\, f_0\, g_0^{\,3}\, m_b \left(A_1 - A_2 \right)\left(A_1 + A_2 \right) = 0$$

→ Seperate the equation based on A_1

$$-48 A_1^2 \pi^3 Q f^2 g_0^3 m_b + 9 A_1^4 \pi Q \beta_m g_0^3 m_b + 18 A_1^2 A_2^2 \pi Q \beta_m g_0^3 m_b$$

$$+ 48 A_1 A_2 \pi^2 Q f^2 g_0^3 m_b - 12 A_1^3 A_2 Q \beta_m g_0^3 m_b + 12 A_1^2 \pi Q f_0^2 g_0^3 m_b$$

$$+ 12 A_1^2 \pi f f_0 g_0^3 m_b - 12 A_1 A_2 Q f_0^2 g_0^3 m_b - 18 A_1^2 \pi Q S V_{ac}^2 \varepsilon_0$$

$$- 24 A_1^2 \pi Q S V_{dc}^2 \varepsilon_0 - 24 A_1 \pi Q S V_{ac} V_{dc} g_0 \varepsilon_0 + 12 A_1 A_2 Q S V_{ac}^2 \varepsilon_0$$

$$+ 32 A_1 A_2 Q S V_{ac} V_{dc} \varepsilon_0 + 24 A_1 A_2 Q S V_{dc}^2 \varepsilon_0 = 48 A_2^2 \pi^3 Q f^2 g_0^3 m_b$$

$$- 9 A_2^4 \pi Q \beta_m g_0^3 m_b - 12 A_2^2 \pi Q f_0^2 g_0^3 m_b + 12 A_2^2 \pi f f_0 g_0^3 m_b$$

$$+ 6 A_2^2 \pi Q S V_{ac}^2 \varepsilon_0 + 24 A_2^2 \pi Q S V_{dc}^2 \varepsilon_0 - 4 A_2 Q S V_{ac}^2 g_0 \varepsilon_0$$

$$- 12 A_2 Q S V_{ac} V_{dc} g_0 \varepsilon_0 - 12 A_2 Q S V_{dc}^2 g_0 \varepsilon_0$$

****
****

$$\left(\left(9 A_2^4 \pi \beta_m g_0^3 m_b - 24 \pi \left(\frac{m_b \left(-\frac{3 \beta_m A_1^2}{2} + 4 \pi^2 f^2 - f_0^2 \right) g_0^3}{2} + S \varepsilon_0 \left(V_{dc}^2 \right. \right. \right. \right.$$

$$\left. \left. \left. + \frac{V_{ac}^2}{4} \right) \right) \right) A_2^2 + \left(12 A_1 m_b \left(4 \pi^2 f^2 - \beta_m A_1^2 - f_0^2 \right) g_0^3 + 12 \left(V_{dc}^2 + V_{dc} V_{ac} \right. \right.$$

$$\left. \left. + \frac{1}{3} V_{ac}^2 \right) \varepsilon_0 S g_0 + 24 \varepsilon_0 A_1 S \left(V_{dc}^2 + \frac{4}{3} V_{dc} V_{ac} + \frac{1}{2} V_{ac}^2 \right) \right) A_2$$

$$- 24 \pi A_1 \left(\frac{\left(-\frac{3 \beta_m A_1^2}{4} + 4 \pi^2 f^2 - f_0^2 \right) m_b A_1 g_0^3}{2} + S V_{ac} V_{dc} g_0 \varepsilon_0 + A_1 \left(V_{dc}^2 \right. \right.$$

$$\left. \left. \left. + \frac{3 V_{ac}^2}{4} \right) S \varepsilon_0 \right) \right) Q + 12 \pi f f_0 g_0^3 m_b \left(A_1 - A_2 \right) \left(A_1 + A_2 \right) = 0$$

$$\left(\left(9 A_2^4 \pi \beta_m g_0^3 m_b - 24 \pi \left(\frac{m_b \left(-\frac{3 \beta_m A_1^2}{2} + 4 \pi^2 f^2 - f_0^2 \right) g_0^3}{2} + S \varepsilon_0 \left(V_{dc}^2 \right. \right. \right. \right. \qquad (14)$$

$$\left. \left. \left. + \frac{V_{ac}^2}{4} \right) \right) \right) A_2^2 + \left(12 A_1 m_b \left(4 \pi^2 f^2 - \beta_m A_1^2 - f_0^2 \right) g_0^3 + 12 \left(V_{dc}^2 + V_{dc} V_{ac} \right. \right.$$

$$\left. \left. + \frac{1}{3} V_{ac}^2 \right) \varepsilon_0 S g_0 + 24 \varepsilon_0 A_1 S \left(V_{dc}^2 + \frac{4}{3} V_{dc} V_{ac} + \frac{1}{2} V_{ac}^2 \right) \right) A_2$$

$$- 24 \pi A_1 \left(\frac{\left(-\frac{3 \beta_m A_1^2}{4} + 4 \pi^2 f^2 - f_0^2 \right) m_b A_1 g_0^3}{2} + S V_{ac} V_{dc} g_0 \varepsilon_0 \right.$$

$$\left. + A_1 \left(V_{dc}^2 + \frac{3 V_{ac}^2}{4} \right) S \varepsilon_0 \right) \right) Q + 12 \pi f f_0 g_0^3 m_b \left(A_1 - A_2 \right) \left(A_1 + A_2 \right) = 0$$

133

$\rightarrow$ Seperate the equation based on A_2

$$-48\ A_2^2\ \pi^3\ Q\ f^2\ g_0^3\ m_b + 18\ A_1^2\ A_2^2\ \pi\ Q\ \beta_m\ g_0^3\ m_b + 48\ A_1\ A_2\ \pi^2\ Q\ f^2\ g_0^3\ m_b$$

$$+9\ A_2^4\ \pi\ Q\ \beta_m\ g_0^3\ m_b - 12\ A_1^3\ A_2\ Q\ \beta_m\ g_0^3\ m_b + 12\ A_2^2\ \pi\ Q\ f_0^2\ g_0^3\ m_b$$

$$-12\ A_1\ A_2\ Q\ f_0^2\ g_0^3\ m_b - 12\ A_2^2\ \pi\ f\ f_0\ g_0^3\ m_b - 6\ A_2^2\ \pi\ Q\ S\ V_{ac}^2\ \varepsilon_0$$

$$-24\ A_2^2\ \pi\ Q\ S\ V_{dc}^2\ \varepsilon_0 + 12\ A_1\ A_2\ Q\ S\ V_{ac}^2\ \varepsilon_0 + 32\ A_1\ A_2\ Q\ S\ V_{ac}\ V_{dc}\ \varepsilon_0$$

$$+24\ A_1\ A_2\ Q\ S\ V_{dc}^2\ \varepsilon_0 + 4\ A_2\ Q\ S\ V_{ac}^2\ g_0\ \varepsilon_0 + 12\ A_2\ Q\ S\ V_{ac}\ V_{dc}\ g_0\ \varepsilon_0$$

$$+12\ A_2\ Q\ S\ V_{dc}^2\ g_0\ \varepsilon_0 = 48\ A_1^2\ \pi^3\ Q\ f^2\ g_0^3\ m_b - 9\ A_1^4\ \pi\ Q\ \beta_m\ g_0^3\ m_b$$

$$-12\ A_1^2\ \pi\ Q\ f_0^2\ g_0^3\ m_b - 12\ A_1^2\ \pi\ f\ f_0\ g_0^3\ m_b + 18\ A_1^2\ \pi\ Q\ S\ V_{ac}^2\ \varepsilon_0$$

$$+24\ A_1^2\ \pi\ Q\ S\ V_{dc}^2\ \varepsilon_0 + 24\ A_1\ \pi\ Q\ S\ V_{ac}\ V_{dc}\ g_0\ \varepsilon_0$$

For better understanding, the above derivation code has been processed into symbolic form rather than pure code language. In the content, A_1 and A_2 are two orthogonal displacement and the purpose of this algebraic derivation is to get an expression for them. Later, the expression of A_1 and A_2 are put into MATLAB for NRI iteration.

A.2 Steady-State Solution Code with MATLAB

File 1: Linear Fitting with integrated tools VPAsolver

```
clear
close all
clc
%%
tic
%Parameter value define
m__b=3.6e-17;
varepsilon__0=8.85e-12;
f__0=97.65e+6;
beta__m=0/m__b;
V__dc=2;
Power=-4;
R_scaling=28.5;
V__ac=sqrt(R_scaling*(10^(-3+(Power/10))));
V__ac=0.2;
g__0=2.2e-7;
S=2.1e-13;
Q=700;
fmin=97e+6;
f_step=20e+3;
fmax=97.6e+6;
S_iz=8e+3;
A_1=zeros(1,3);
A_2=zeros(1,3);
%%
f_range=fmin:f_step:fmax;
freq=fmin:f_step:(fmax-f_step);
for i=1:length(f_range)
    i
    syms a_1 a_2
    f=f_range(i);
    assume(a_1,'real')
    assume(a_2,'real')
    [amp_1,amp_2]=vpasolve([(-(3*a_1^3*f__0^2*g__0^3*m__b)/8 + ((((-
(3*a_2^2)/4 - 1)*f__0^2 + f^2)*m__b*g__0^3)/2 +
varepsilon__0*S*(V__dc^2 + (3*V__ac^2)/4))*a_1 +
varepsilon__0*S*V__dc*V__ac*g__0)*Q - a_2*f__0*g__0^3*m__b*f/2==0,-
(3*beta__m*f__0^2*a_2^3*Q*m__b*g__0^3)/8 + (((((-(3*a_1^2*beta__m)/4 -
1)*f__0^2 + f^2)*m__b*g__0^3)/2 + varepsilon__0*S*(V__dc^2 +
V__ac^2/4))*Q*a_2 + a_1*f__0*g__0^3*m__b*f/2==0],[a_1,a_2],[5e-12,5e-
12])


    Amp_1=((amp_1));
    Amp_2=((amp_2));
    S1A_1(i)=max(Amp_1);
    S2A_1(i)=min(Amp_1);
    S3A_1(i)=median(Amp_1);
    S1A_2(i)=max(Amp_2);
    S2A_2(i)=min(Amp_2);
    S3A_2(i)=median(Amp_2);
```

```
    RealAmp(i)=sqrt(S1A_1(i)^2+S1A_2(i)^2);
    doubleRealAmp(i)=double(RealAmp(i));
    Theta_1(i)=180*atan(((S1A_2(i)/S1A_1(i))));
    doubleTheta_1(i)=double(Theta_1(i));
      RealAmp_1(i)=S1A_2(i)*SC;
      RealAmp_2(i)=S2A_2(i)*SC;
    Phase_1(i)=360*Theta_1(i)/(2*pi);
     doubleRealAmp_1(i)=double(RealAmp_1(i));
     doubleRealAmp_2(i)=double(RealAmp_2(i));
    %Take derivative of calculated amplitde in each frequency
interval and
    %record them.
     if i>1
         X_1(i-1)=S_iz*((((S1A_1(i)-S1A_1(i-1))/f_step)));
     doubleCurrent=double(X_1);
     end
%Transfer parameter into double to extract and plot in origin
doubleAmp_1=double(Amplitude_Overall_1);
doubleAmp_2=double(Amplitude_Overall_2);
doublePha_1=double(Phase_1);
doublePha_2=double(Phase_2);
end
%Plot
figure(1)
plot(f_range,Phase_1,'r')
hold on
plot(f_range,Phase_2,'g')
grid on
legend('Maximum Sol','Minimum Sol');
xlabel('frequency(Hz)');ylabel('Phase Change(Deg)');
figure(2)
plot(f_range,S1A_1,'b')
 hold on
plot(f_range,S1A_2,'r')
grid on
legend('A','B');
xlabel('frequency(Hz)');ylabel('Displacement(a.u)');
figure(3)
plot(f_range,RealAmp_1,'b')
hold on
plot(f_range,RealAmp_2,'r')
hold on
load Data.mat
m=Data.('Frequency');
n=abs(Data.('Experiment_Forward'));
o=abs(Data.('Experiment_Backward'));
plot(m,n,'.')
hold on
plot(m,0,'.')
grid on
xlabel('frequency(Hz)');ylabel('Current(a.u)');

figure(3)
plot(freq,X_1,'b')
hold on
load Data.mat
m=Data.('Frequency');
n=Data.('-4bm');
```

Appendix

```
plot(m,n,'.')
hold on
plot(freq,X_2,'r')
grid on
legend('Maximum Sol','Minimum Sol');
 xlabel('frequency(Hz)');ylabel('In-phase Current(A)');
toc
```

File 2: Newton-Raphson Iteration part

```matlab
function [NR_Iteration] =
NewtonRaphson1dof(tol,m,k,beta,aMax,maxIter,W)

% This function calculates the output for the modal backbone curve of
the
% 1dof oscillator

% Array with the oscillation amplitudes of the mass computed with N-R
NR_Iteration = zeros(1,length(W));

% For each pulsation and value N-R is applied to solve the equation
% G(amplitude,w)=0
for i=1:length(W)
    % n: number of iterations
    n = 1;
    % The initial value of the amplitude for the N-R loop is aMax
    amplitude = aMax;
    % Initial evaluation of the equation G(amplitude,W(i))
    F = NMBeq1dof(m,k,beta,W(i),amplitude);
    % NEWTON-RAPHSON LOOP
    while norm(F)>tol && n<=maxIter
        F = NMBeq1dof(m,k,beta,W(i),amplitude);
        J = NMBjac1dof(m,k,beta,W(i),amplitude);
        amplitude = amplitude - J\F;
        n = n+1;
    end

    % The solution computed, amplitude, is assigned to the output
matrix:
    % AmplitudeNMB
    if n<=maxIter,
        AmplitudeNMB(i) = amplitude;
    end
end

end
```

Appendix

File 3: Nonlinear Galerkin Matrix

```
function G = Galerkin_dof(m,k,beta,w,amplitude)
F = [[(-(3*beta__m*a_1^3*f__0^2*g__0^3*m__b)/8 + ((((-
(3*a_2^2*beta__m)/4 - 1)*f__0^2 + f^2)*m__b*g__0^3)/2 +
varepsilon__0*S*(V__dc^2 + (3*V__ac^2)/4))*a_1 +
varepsilon__0*S*V__dc*V__ac*g__0)*Q - a_2*f__0*g__0^3*m__b*f/2==0,-
(3*beta__m*f__0^2*a_2^3*Q*m__b*g__0^3)/8 + ((((-(3*a_1^2*beta__m)/4 -
1)*f__0^2 + f^2)*m__b*g__0^3)/2 + varepsilon__0*S*(V__dc^2 +
V__ac^2/4))*Q*a_2 + a_1*f__0*g__0^3*m__b*f/2==0]
];
End
```

File 4: Nonlinear Galerkin Jacobian Matrix

```
function J = Galerkin_jac1dof(m,k,beta,w,amplitude)

% This function returns the derivative J of the 1dof algebraic
equation
% for the modal backbone curve

J = [-(9*A__1^2*beta__m*f__0^2*g__0^3*m__b*L)/8 + (m__b*((-
(3*beta__m*A__2^2)/4 - 1)*f__0^2 + omega^2)*g__0^3/2 +
varepsilon__0*S*(V__dc^2 + (3*V__ac^2)/4))*L,
(9*A__1*beta__m*f__0^2*g__0^3*m__b*L*X__1)/4 + m__b*(-
(3*A__2*beta__m*L*X__2*f__0^2)/2 + 2*omega)*g__0^3/2, (-
3/4*m__b*beta__m*L*X__2*f__0^2*g__0^3*A__1 -
3/4*m__b*A__2*beta__m*f__0^2*g__0^3*L*X__1)*Q - f__0*g__0^3*m__b/2;
 -3/4*beta__m*f__0^2*g__0^3*m__b*L*X__1*Q*A__2 -
3/4*m__b*beta__m*L*X__2*f__0^2*g__0^3*A__1*Q + 1/2*f__0*g__0^3*m__b]
End
```

File 5: Thermomechanical Noise Fitting Model: Iteration File.

```matlab
clear
close all
clc

%%
tic
%tuning parameters
S_vsys =0.65;
f_0=97.8435e+6;
w_0=f_0*2*3.1415926;
%w_0=f_0;
Q=71.5e+3;
R=6.7e+12;


% Experimental data
load Data_35.mat
m=Data.('Frequency');
n=Data.('2V');

%fixed parameters
k_b=1.38065e-23;
m_eff=1.96279e-17;
Temp=298;

%frequency sweep
fmin=97.795e+6;
fstep=0.0001e+6;
fmax=97.895e+6;

%%
f_range=fmin:fstep:fmax;
for i=1:length(f_range)
    i;
    f=f_range(i);
    w=f*2*3.1415926;
    %w=f
    S_vt=sqrt(R^2*(((4*w_0*k_b*Temp)/(Q*m_eff))/((w_0^2-
w^2)^2+(w_0*w/Q)^2))+S_vsys^2)
    S_vtotal(i)=S_vt;
    S_xt=S_vt/R;
    S_xtotal(i)=S_xt*1e+12;
end
RMSE=sqrt(sum((n(i)-S_vtotal(i))^2)/numel(n));
avg_n=sum(n)/length(n);
RRMSE=100*RMSE/avg_n
figure(1)
plot(f_range,n,'.')
txt=['RRMSE error=' num2str(RRMSE),'%'];
text(fmax-0.2*(fmax-fmin),max(n)-0.001*(max(n)-
min(n)),txt,'fontsize',16)
txt=['R=' num2str(R/1e+12),'nV/pm'];
text(fmax-0.2*(fmax-fmin),max(n)-0.101*(max(n)-
min(n)),txt,'fontsize',16)
txt=['Q=' num2str(Q)];
text(fmax-0.2*(fmax-fmin),max(n)-0.201*(max(n)-
```

Appendix

```
min(n)),txt,'fontsize',16)
hold on
yyaxis left
ylabel('S_vtotal^{1/2}(V*Hz^{-1/2})','fontsize',16)
plot(f_range,S_vtotal,'black-','linewidth',1);
yyaxis right
ylabel('S_xtotal^{1/2}(pm*Hz^{-1/2})','fontsize',16)
plot(f_range,S_xtotal,'o-','linewidth',1);
xlim([fmin,fmax]);
grid on
xlabel('frequency(Hz)','fontsize',16);
toc
```

File 6: Thermomechanical Noise Fitting Model: Fitting and Plotting

```
load Data_23.mat
m_23=Data.('Frequency');
n_1=Data.('0V');
n_2=Data.('0p1V');
n_3=Data.('1V');
load Data_29.mat
m_29=Data.('Frequency');
n_4=Data.('0V');
n_5=Data.('0p1V');
n_6=Data.('1V');
load Data_30.mat
m_30=Data.('Frequency');
n_7=Data.('0V');
n_8=Data.('0p1V');
n_9=Data.('1V');
load Data_35.mat
m_35=Data.('Frequency');
n_10=Data.('0V');
n_11=Data.('0p1V');
n_12=Data.('1V');
figure subplot(431),plot(m_23,n_1);grid
on;xlim([min(m_23),max(m_23)]);ylim([0,6]);xlabel('frequency(Hz)','fo
ntsize',12);ylabel('S_{vtotal}^{1/2}(V*Hz^{-
1/2})','fontsize',12);legend({'V_g=0V,R23'},'fontsize',16);
subplot(432),plot(m_23,n_2);grid
on;xlim([min(m_23),max(m_23)]);ylim([0,6]);xlabel('frequency(Hz)','fo
ntsize',12);ylabel('S_{vtotal}^{1/2}(V*Hz^{-
1/2})','fontsize',12);legend({'V_g=0.1V,R23'},'fontsize',16);
subplot(433),plot(m_23,n_3);grid
on;xlim([min(m_23),max(m_23)]);ylim([0,6]);xlabel('frequency(Hz)','fo
ntsize',12);ylabel('S_{vtotal}^{1/2}(V*Hz^{-
1/2})','fontsize',12);legend({'V_g=1V,R23'},'fontsize',16);
subplot(434),plot(m_29,n_4);grid
on;xlim([min(m_29),max(m_29)]);ylim([0,25]);xlabel('frequency(Hz)','f
ontsize',12);ylabel('S_{vtotal}^{1/2}(V*Hz^{-
1/2})','fontsize',12);legend({'V_g=0V,R29'},'fontsize',16);
subplot(435),plot(m_29,n_5);grid
on;xlim([min(m_29),max(m_29)]);ylim([0,25]);xlabel('frequency(Hz)','f
ontsize',12);ylabel('S_{vtotal}^{1/2}(V*Hz^{-
1/2})','fontsize',12);legend({'V_g=0.1V,R29'},'fontsize',16);
subplot(436),plot(m_29,n_6);grid
on;xlim([min(m_29),max(m_29)]);ylim([0,25]);xlabel('frequency(Hz)','f
ontsize',12);ylabel('S_{vtotal}^{1/2}(V*Hz^{-
1/2})','fontsize',12);legend({'V_g=1V,R29'},'fontsize',16);
subplot(437),plot(m_30,n_7);grid
on;xlim([min(m_30),max(m_30)]);ylim([0,20]);xlabel('frequency(Hz)','f
ontsize',12);ylabel('S_{vtotal}^{1/2}(V*Hz^{-
1/2})','fontsize',12);legend({'V_g=0V,R30'},'fontsize',16);
subplot(438),plot(m_30,n_8);grid
on;xlim([min(m_30),max(m_30)]);ylim([0,20]);xlabel('frequency(Hz)','f
ontsize',12);ylabel('S_{vtotal}^{1/2}(V*Hz^{-
1/2})','fontsize',12);legend({'V_g=0.1V,R30'},'fontsize',16);
subplot(439),plot(m_30,n_9);grid
on;xlim([min(m_30),max(m_30)]);ylim([0,20]);xlabel('frequency(Hz)','f
ontsize',12);ylabel('S_{vtotal}^{1/2}(V*Hz^{-
1/2})','fontsize',12);legend({'V_g=1V,R30'},'fontsize',16);
```

Appendix

```
subplot(4,3,10),plot(m_35,n_10);grid
on;xlim([min(m_35),max(m_35)]);ylim([0,4.5]);xlabel('frequency(Hz)','
fontsize',12);ylabel('S_{vtotal}^{1/2}(V*Hz^{-
1/2})','fontsize',12);legend({'V_g=0V,R35'},'fontsize',16);
subplot(4,3,11),plot(m_35,n_11);grid
on;xlim([min(m_35),max(m_35)]);ylim([0,4.5]);xlabel('frequency(Hz)','
fontsize',12);ylabel('S_{vtotal}^{1/2}(V*Hz^{-
1/2})','fontsize',12);legend({'V_g=0.1V,R35'},'fontsize',16);
subplot(4,3,12),plot(m_35,n_12);grid
on;xlim([min(m_35),max(m_35)]);ylim([0,4.5]);xlabel('frequency(Hz)','
fontsize',12);ylabel('S_{vtotal}^{1/2}(V*Hz^{-
1/2})','fontsize',12);legend({'V_g=1V,R35'},'fontsize',16);
sgtitle('Cross-comparison between different beam
length','fontsize',30)
```

A.3 Coupled Oscillator Displacement Modelling

The method describes the nonlinear motion in chapter 3 was only for single degree of freedom. In future, for applications such as reservoir computing or neuromorphic computing that requires multiple nonlinear oscillators coupled with each other, model needs to be built based on n-th degree of freedom system. Although certain complexity is involved, my methodology of producing the model can still be applied with only a few changes. This capability of usage expansion comes from two points. First is the device design. The doubly-clamped silicon beam is a simple and common structure that gives rise to its excellent compatibility. This structure can be easily modified and combined with self-mechanical/electrical coupling or CMOS technology. As preliminaries, I will present an example of using same strategy to model a coupled oscillator.
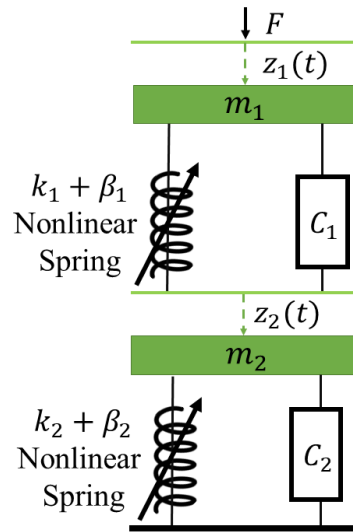
Figure A.1 Scheme of a forced 2 degree of freedom oscillators. $k, \beta, C, z(t), F$ are linear and nonlinear stiffness, damping coefficient, displacement, and external force, respectively.

Note that, for the simplicity, this section will skip the discussion of the coupler. But in practical scenarios, the use of coupler will also affect the motion of the system where its rigidity or stiffness can change the force applied on the coupled oscillator correspondingly. In that case, the force of the second oscillator as shown in Equation

(A.2) should be modelled separately by considering material properties of the coupler.

Each of the oscillators are modelled accordingly as,

$$m_1 z_1'' + C_1 z_1' + C_2(z_1' - z_2') + k_1 z_1 - k_2(z_1 - z_2)$$
$$+\beta_1 z_1^3 - \beta_2(z_1 - z_2)^3 = F \qquad (A.1)$$

$$m_2 z_2'' + C_2(z_1' - z_2') + k_2(z_1 - z_2) + \beta_2(z_1 - z_2)^3$$
$$= F \qquad (A.2)$$

Given the test function of each oscillator as,

$$z_1(t) = A_1 \cos(\omega t) + B_1 \sin(\omega t) \qquad (A.3)$$

$$z_2(t) = A_2 \cos(\omega t) + B_2 \sin(\omega t) \qquad (A.4)$$

where two degrees of freedom of oscillation introduce four orthogonal displacements. Hence, we need to construct four Galerkin functions to fulfill the solution. Marking the residual force of each freedom of oscillator as $R_1(t)$ and $R_2(t)$, I have

$$\mathbf{G} = \begin{pmatrix} \int_0^{\frac{2\pi}{\omega}} R_1(t) A_1 \cos(\omega t) \, dt & \int_0^{\frac{2\pi}{\omega}} R_2(t) A_2 \cos(\omega t) \, dt \\ \int_0^{\frac{2\pi}{\omega}} R_1(t) B_1 \sin(\omega t) \, dt & \int_0^{\frac{2\pi}{\omega}} R_2(t) B_2 \sin(\omega t) \, dt \end{pmatrix} = 0 \qquad (A.5)$$

Next, I will take partial derivatives of each function in Equation (A.5) with respect to A_1, A_2, B_1, B_2 concerning omega, yielding a 4×4 Jacobian matrix. To avoid a repetitive and tedious symbolic manipulation process, I will skip the description of this part here. The subsequent solution process can still employ the NRI method to obtain the numerical solutions for A_1, A_2, B_1, B_2. For this model, we can also substitute the previously defined parameters k_e, β_m, and β_e into the corresponding

parameters k and β in Equations (A.1) and (A.2) to characterise the voltage-dependent linear and nonlinear effects.

In summary, although I do not have actual coupled oscillator devices for detailed modelling and description, this section demonstrates the expandability of our novel methodology. For any n-th degrees of freedom, we can apply the same approach for modelling and solving, and importantly, we can embed our innovative voltage-dependent nonlinear parameter into the corresponding model. This has significant implications for future research.

Reference List

[1]   K. K. Young, "Short-channel effect in fully depleted SOI MOSFETs," *IEEE Transactions on Electron Devices,* vol. 36, no. 2, pp. 399-402, 1989, doi: 10.1109/16.19942.

[2]   R. R. Troutman, "VLSI limitations from drain-induced barrier lowering," *IEEE Journal of Solid-State Circuits,* vol. 14, no. 2, pp. 383-391, 1979, doi: 10.1109/JSSC.1979.1051189.

[3]   T. Y. Chan, J. Chen, P. K. Ko, and C. Hu, "The impact of gate-induced drain leakage current on MOSFET scaling," in *1987 International Electron Devices Meeting*, 6-9 Dec. 1987 1987, pp. 718-721, doi: 10.1109/IEDM.1987.191531.

[4]   A. Amerasekera, M. C. Chang, J. A. Seitchik, A. Chatterjee, K. Mayaram, and J. H. Chern, "Self-heating effects in basic semiconductor structures," *IEEE Transactions on Electron Devices,* vol. 40, no. 10, pp. 1836-1844, 1993, doi: 10.1109/16.277342.

[5]   J. Pelka and L. Baldi, "More-than-Moore Technologies and Applications," in *Nanoelectronics*, 2017, pp. 53-72.

[6]   W. Arden, M. Brillouët, P. Cogez, M. Graef, B. Huizing, and R. Mahnkopf, "More-than-Moore white paper," *Version,* vol. 2, p. 14, 2010.

[7]   E. Peeters, S. Vergote, B. Puers, and W. Sansen, "A highly symmetrical capacitive micro-accelerometer with single degree-of-freedom response," *Journal of Micromechanics and Microengineering,* vol. 2, no. 2, p. 104, 1992/06/01 1992, doi: 10.1088/0960-1317/2/2/006.

[8]   G. M. Rebeiz, C. D. Patel, S. K. Han, C. Ko, and K. M. J. Ho, "The Search for a Reliable MEMS Switch," *IEEE Microwave Magazine,* vol. 14, no. 1, pp. 57-67, 2013, doi: 10.1109/MMM.2012.2226540.

[9]   N. Abele, A. Villaret, A. Gangadharaiah, C. Gabioud, P. Ancey, and A. M. Ionescu, "1T MEMS Memory Based on Suspended Gate MOSFET," in *2006 International Electron Devices Meeting*, 11-13 Dec. 2006 2006, pp. 1-4, doi: 10.1109/IEDM.2006.346826.

[10]   L. Duraffourg and J. Arcamone, "From MEMS to NEMS," in *Nanoelectromechanical Systems*, 2015, pp. 1-11.

[11]   F. D. Bannon, J. R. Clark, and C. T. Nguyen, "High-Q HF microelectromechanical filters," *IEEE Journal of Solid-State Circuits,* vol. 35,

Reference List

no. 4, pp. 512-526, 2000, doi: 10.1109/4.839911.

[12]   K. L. Ekinci, Y. T. Yang, and M. L. Roukes, "Ultimate limits to inertial mass sensing based upon nanoelectromechanical systems," *Journal of Applied Physics,* vol. 95, no. 5, pp. 2682-2689, 2004/03/01 2004, doi: 10.1063/1.1642738.

[13]   K. Jensen, J. Weldon, H. Garcia, and A. Zettl, "Nanotube Radio," *Nano Letters,* vol. 7, no. 11, pp. 3508-3511, 2007/11/01 2007, doi: 10.1021/nl0721113.

[14]   J. D. Teufel *et al.*, "Sideband cooling of micromechanical motion to the quantum ground state," *Nature,* vol. 475, no. 7356, pp. 359-363, 2011/07/01 2011, doi: 10.1038/nature10261.

[15]   M. V. Andres, K. W. H. Foulds, and M. J. Tudor, "Nonlinear vibrations and hysteresis of micromachined silicon resonators designed as frequency-out sensors," *Electronics Letters,* vol. 23, no. 18, pp. 952-954, 1987, doi: 10.1049/el:19870670.

[16]   N. Ghaemi, A. Nikoobin, and M. R. Ashory, "A Comprehensive Categorization of Micro/Nanomechanical Resonators and Their Practical Applications from an Engineering Perspective: A Review," *Advanced Electronic Materials,* vol. 8, no. 11, p. 2200229, 2022/11/01 2022, doi:

[17]   E. Sage *et al.*, "Single-particle mass spectrometry with arrays of frequency-addressed nanomechanical resonators," *Nature Communications,* vol. 9, no. 1, p. 3283, 2018/08/16 2018, doi: 10.1038/s41467-018-05783-4.

[18]   M. Sansa, V. Nguyen, S. Baguet, C. Lamarque, R. Dufour, and S. Hentz, "Real time sensing in the non linear regime of nems resonators," in *2016 IEEE 29th International Conference on Micro Electro Mechanical Systems (MEMS)*, 24-28 Jan. 2016 2016, pp. 1050-1053, doi: 10.1109/MEMSYS.2016.7421814.

[19]   M. Sansa, M. Fernández-Regúlez, J. Llobet, Á. San Paulo, and F. Pérez-Murano, "High-sensitivity linear piezoresistive transduction for nanomechanical beam resonators," *Nature Communications,* Article vol. 5, p. 4313, 07/07/online 2014, doi: 10.1038/ncomms5313

[20]   M. Sansa *et al.*, "Frequency fluctuations in silicon nanoresonators," *Nature Nanotechnology,* Article vol. 11, p. 552, 02/29/online 2016, doi: 10.1038/nnano.2016.19

[21]   M. Sansa, M. Fernández-Regúlez, Á. San Paulo, and F. Pérez-Murano, "Electrical transduction in nanomechanical resonators based on doubly clamped bottom-up silicon nanowires," *Applied Physics Letters,* vol. 101, no. 24, p. 243115, 2012/12/10 2012, doi: 10.1063/1.4771982.

[22]   J. C. Coulombe, M. C. A. York, and J. Sylvestre, "Computing with networks of nonlinear mechanical oscillators," *PLOS ONE,* vol. 12, no. 6, p. e0178663,

Reference List

2017, doi: 10.1371/journal.pone.0178663.

[23]   M. Rafaie, M. H. Hasan, and F. M. Alsaleem, "Neuromorphic MEMS sensor network," *Applied Physics Letters,* vol. 114, no. 16, p. 163501, 2019/04/22 2019, doi: 10.1063/1.5081804.

[24]   F. M. Alsaleem, M. H. H. Hasan, and M. K. Tesfay, "A MEMS Nonlinear Dynamic   Approach   for   Neural   Computing,"   *Journal   of Microelectromechanical Systems,* vol. 27, no. 5, pp. 780-789, 2018, doi: 10.1109/JMEMS.2018.2864175.

[25]   F. A. Hassani, "Resonant nano-electro-mechanical sensors for molecular mass-detection," Thesis (Ph D) - University of Southampton, School of Electronics and Computer Science, 2012, Original typescript,, 2012. [Online].

[26]   A. F. Hassani, Y. Tsuchiya, and H. Mizuta, "In-Plane Resonant Nano-Electro-Mechanical Sensors: A Comprehensive Study on Design, Fabrication and Characterization   Challenges,"   *Sensors,*   vol.   13,   no.   7,   2013,   doi: 10.3390/s130709364.

[27]   Y. Tsuchiya *et al.*, "Characteristic resonance features of SOI-CMOS-compatible silicon nanoelectromechanical doubly-clamped beams up to 330 MHz," in *2018 IEEE Micro Electro Mechanical Systems (MEMS)*, 21-25 Jan. 2018 2018, pp. 515-518, doi: 10.1109/MEMSYS.2018.8346603.

[28]   S. Tiwari and R. N. Candler, "Using flexural MEMS to study and exploit nonlinearities: a review," *Journal of Micromechanics and Microengineering,* vol. 29, no. 8, p. 083002, 2019/06/10 2019, doi: 10.1088/1361-6439/ab23e2.

[29]   V. Gouttenoire *et al.*, "Digital and FM Demodulation of a Doubly Clamped Single-Walled Carbon-Nanotube Oscillator: Towards a Nanotube Cell Phone," (in English), *Small,* vol. 6, no. 9, pp. 1060-1065, May 7 2010, doi: 10.1002/smll.200901984.

[30]   V. Zega *et al.*, "Numerical Modelling of Non-Linearities in MEMS Resonators," *Journal of Microelectromechanical Systems,* vol. 29, no. 6, pp. 1443-1454, 2020, doi: 10.1109/JMEMS.2020.3026085.

[31]   H. Kou *et al.*, "Nonlinear characteristics of contact-induced vibrations of the rotating variable thickness plate under large deformations," *European Journal of Mechanics - A/Solids,* vol. 77, p. 103801, 2019/09/01/ 2019, doi:

[32]   C. Méndez, S. Paquay, I. Klapka, and J. P. Raskin, "Effect of geometrical nonlinearity on MEMS thermoelastic damping," *Nonlinear Analysis: Real World Applications,* vol. 10, no. 3, pp. 1579-1588, 2009/06/01/ 2009, doi:

[33]   N. Herisanu, B. Marinca, and V. Marinca, "Nonlinear Vibration of Double-Walled Carbon Nanotubes Subjected to Mechanical Impact and Embedded on Winkler–Pasternak Foundation," *Materials,* vol. 15, no. 23*,* doi:

Reference List

10.3390/ma15238599.

[34]   C. A. J. Fletcher, "Computational Galerkin Methods," in *Computational Galerkin Methods*, C. A. J. Fletcher Ed. Berlin, Heidelberg: Springer Berlin Heidelberg, 1984, pp. 72-85.

[35]   M. H. Matheny, L. G. Villanueva, R. B. Karabalin, J. E. Sader, and M. L. Roukes, "Nonlinear Mode-Coupling in Nanomechanical Systems," *Nano Letters,* vol. 13, no. 4, pp. 1622-1626, 2013/04/10 2013, doi: 10.1021/nl400070e.

[36]   P. Rafiee, G. Khatibi, and M. Zehetbauer, "A review of the most important failure, reliability and nonlinearity aspects in the development of microelectromechanical systems (MEMS)," *Microelectronics International,* vol. 34, no. 1, pp. 9-21, 2017, doi: 10.1108/MI-03-2015-0026.

[37]   H. Zhu and J. E. Y. Lee, "System-level circuit simulation of nonlinearity in micromechanical resonators," *Sensors and Actuators A: Physical,* vol. 186, pp. 15-20, 2012/10/01/ 2012,

[38]   D. Antonio, D. H. Zanette, and D. López, "Frequency stabilization in nonlinear micromechanical oscillators," *Nature Communications,* vol. 3, no. 1, p. 806, 2012/05/01 2012, doi: 10.1038/ncomms1813.

[39]   C. Samanta, N. Arora, and A. K. Naik, "Tuning of geometric nonlinearity in ultrathin nanoelectromechanical systems," *Applied Physics Letters,* vol. 113, no. 11, p. 113101, 2018/09/10 2018, doi: 10.1063/1.5026775.

[40]   V. Kaajakari, T. Mattila, A. Oja, and H. Seppa, "Nonlinear limits for single-crystal silicon microresonators," *Journal of Microelectromechanical Systems,* vol. 13, no. 5, pp. 715-724, 2004, doi: 10.1109/JMEMS.2004.835771.

[41]   L. Jin, J. Mei, and L. Li, "Nonlinear dynamics of a doubly clamped carbon nanotube resonator considering surface stress," *Rsc Advances,* vol. 5, no. 10, pp. 7215-7221, 2015.

[42]   K. Lu *et al.*, "Modal Coupling Effect in a Novel Nonlinear Micromechanical Resonator," *Micromachines,* vol. 11, no. 5, 2020, doi: 10.3390/mi11050472.

[43]   F. Ben, J. Fernando, J.-Y. Ou, and Y. Tsuchiya, "Development of Systematic Fitting Model for Nonlinear Nanoelectromechanical Resonance Analysis," in *2021 IEEE 34th International Conference on Micro Electro Mechanical Systems (MEMS)*, 25-29 Jan. 2021 2021, pp. 611-614, doi: 10.1109/MEMS51782.2021.9375461.

[44]   Y. Su, P. Xu, G. Han, C. Si, J. Ning, and F. Yang, "The Characteristics and Locking Process of Nonlinear MEMS Gyroscopes," *Micromachines,* vol. 11, no. 2, p. 233, 2020.

Reference List

[45]   F. Dinca, C. Teodosiu, and T. T. Soong, "Nonlinear and random vibrations," 1973.

[46]   R. Hooke, "De Potentia Restitutiva, or of Spring. Explaining the Power of Springing Bodies," 1678.

[47]   A. Erbe, H. Krömmer, A. Kraus, R. H. Blick, G. Corso, and K. Richter, "Mechanical mixing in nonlinear nanomechanical resonators," *Applied Physics Letters,* vol. 77, no. 19, pp. 3102-3104, 2000/11/06 2000, doi: 10.1063/1.1324721.

[48]   V. Sazonova, Y. Yaish, H. Üstünel, D. Roundy, T. A. Arias, and P. L. McEuen, "A tunable carbon nanotube electromechanical oscillator," *Nature,* vol. 431, no. 7006, pp. 284-287, 2004/09/01 2004, doi: 10.1038/nature02905.

[49]   H.-M. Jeong and S. K. Ha, "Dynamic analysis of a resonant comb-drive micro-actuator in linear and nonlinear regions," *Sensors and Actuators A: Physical,* vol. 125, no. 1, pp. 59-68, 2005/10/21/ 2005,

[50]   M. Palaniapan and L. Khine, "Nonlinear behavior of SOI free-free micromechanical beam resonator," *Sensors and Actuators A: Physical,* vol. 142, no. 1, pp. 203-210, 2008/03/10/ 2008,

[51]   D. K. Agrawal, J. Woodhouse, and A. A. Seshia, "Modeling nonlinearities in MEMS oscillators," *IEEE Transactions on Ultrasonics, Ferroelectrics, and Frequency Control,* vol. 60, no. 8, pp. 1646-1659, 2013, doi: 10.1109/TUFFC.2013.2747.

[52]   N. Kacem, H. Sébastien, S. Baguet, and R. Dufour, *From MEMS to NEMS: Modelling and characterization of the non linear dynamics of resonators, a way to enhance the dynamic range*. NSTI-Nanotech, 2008.

[53]   C. Samanta, P. R. Yasasvi Gangavarapu, and A. K. Naik, "Nonlinear mode coupling and internal resonances in MoS2 nanoelectromechanical system," *Applied Physics Letters,* vol. 107, no. 17, p. 173110, 2015/10/26 2015, doi: 10.1063/1.4934708.

[54]   N. Kacem, S. Hentz, D. Pinto, B. Reig, and V. Nguyen, "Nonlinear dynamics of nanomechanical beam resonators: improving the performance of NEMS-based sensors," *Nanotechnology,* vol. 20, no. 27, p. 275501, 2009/06/16 2009, doi: 10.1088/0957-4484/20/27/275501.

[55]   T. H. Stievater *et al.*, "Measurement of thermal-mechanical noise in MEMS microstructures," in *SPIE MOEMS-MEMS*, 2003.

[56]   J. Lee, Z. Wang, K. He, J. Shan, and P. X. L. Feng, "High Frequency MoS2 Nanomechanical Resonators," *ACS Nano,* vol. 7, no. 7, pp. 6086-6091, 2013/07/23 2013, doi: 10.1021/nn4018872.

Reference List

[57]   M. I. Younis and F. Alsaleem, "Exploration of New Concepts for Mass Detection in Electrostatically-Actuated Structures Based on Nonlinear Phenomena," *Journal of Computational and Nonlinear Dynamics,* vol. 4, no. 2, 2009, doi: 10.1115/1.3079785.

[58]   W. Zhang and K. L. Turner, "Application of parametric resonance amplification in a single-crystal silicon micro-oscillator based mass sensor," *Sensors and Actuators A: Physical,* vol. 122, no. 1, pp. 23-30, 2005/07/29/ 2005,

[59]   H. K. Lee, R. Melamud, S. Chandorkar, J. Salvia, S. Yoneoka, and T. W. Kenny, "Stable Operation of MEMS Oscillators Far Above the Critical Vibration Amplitude in the Nonlinear Regime," *Journal of Microelectromechanical Systems,* vol. 20, no. 6, pp. 1228-1230, 2011, doi: 10.1109/JMEMS.2011.2170821.

[60]   E. Kenig *et al.*, "Passive phase noise cancellation scheme," *Physical review letters,* vol. 108 26, p. 264102, 2012.

[61]   M. Pardo, L. Sorenson, and F. Ayazi, "An Empirical Phase-Noise Model for MEMS Oscillators Operating in Nonlinear Regime," *IEEE Transactions on Circuits and Systems I: Regular Papers,* vol. 59, no. 5, pp. 979-988, 2012,

[62]   L. G. Villanueva, R. B. Karabalin, M. H. Matheny, E. Kenig, M. C. Cross, and M. L. Roukes, "A Nanoscale Parametric Feedback Oscillator," *Nano Letters,* vol. 11, no. 11, pp. 5054-5059, 2011/11/09 2011,

[63]   L. G. Villanueva *et al.*, "Surpassing Fundamental Limits of Oscillators Using Nonlinear Resonators," *Physical Review Letters,* vol. 110, no. 17, p. 177208, 04/26/ 2013,

[64]   O. Shoshani, D. Heywood, Y. Yang, T. W. Kenny, and S. W. Shaw, "Phase Noise Reduction in an MEMS Oscillator Using a Nonlinearly Enhanced Synchronization Domain," *Journal of Microelectromechanical Systems,* vol. 25, no. 5, pp. 870-876, 2016, doi: 10.1109/JMEMS.2016.2590881.

[65]   A. Bouchaala *et al.*, "Nonlinear-Based MEMS Sensors and Active Switches for Gas Detection," *Sensors*, vol. 16, no. 6*,* doi: 10.3390/s16060758.

[66]   B. Andò, S. Baglio, C. Trigona, N. Dumas, L. Latorre, and P. Nouet, "Nonlinear mechanism in MEMS devices for energy harvesting applications," *Journal of Micromechanics and Microengineering,* vol. 20, no. 12, p. 125020, 2010/11/18 2010, doi: 10.1088/0960-1317/20/12/125020.

[67]   G. Dion, S. Mejaouri, and J. Sylvestre, "Reservoir computing with a single delay-coupled non-linear mechanical oscillator," *Journal of Applied Physics,* vol. 124, no. 15, 2018, doi: 10.1063/1.5038038.

[68]   B. J. Sheu, D. L. Scharfetter, P. K. Ko, and M. C. Jeng, "BSIM: Berkeley

Reference List

short-channel IGFET model for MOS transistors," *IEEE Journal of Solid-State Circuits,* vol. 22, no. 4, pp. 558-566, 1987, doi: 10.1109/JSSC.1987.1052773.

[69]   C. Multiphysics, "Introduction to comsol multiphysics®," *COMSOL Multiphysics, Burlington, MA, accessed Feb,* vol. 9, no. 2018, p. 32, 1998.

[70]   P. C. Kohnke, "ANSYS," in *Finite Element Systems: A Handbook*, C. A. Brebbia Ed. Berlin, Heidelberg: Springer Berlin Heidelberg, 1982, pp. 19-25.

[71]   G. Duffing, "Forced oscillations with variable natural frequency and their technical significance," *Vieweg, Braunschschweig,* 1918.

[72]   K. Lachmann, "Beitrag zum Schwingungsproblem von Duffing," *Mathematische Annalen,* vol. 99, no. 1, pp. 479-492, 1928/12/01 1928, doi: 10.1007/BF01459109.

[73]   K. O. Friedrichs, "Integration in the complex plane," *Electrical Engineering,* vol. 61, no. 3, pp. 139-143, 1942, doi: 10.1109/EE.1942.6436209.

[74]   I. Kovacic and M. J. Brennan, *The Duffing equation: nonlinear oscillators and their behaviour*. John Wiley & Sons, 2011.

[75]   C. Maclaurin, *An account of Sir Isaac Newton's philosophical discoveries*. Georg Olms Verlag, 1750.

[76]   H. Poincaré, "On the three-body problem and the equations of dynamics," *Acta Math,* vol. 13, no. 1, 1890.

[77]   J.-H. He, "Modified Lindstedt–Poincare methods for some strongly non-linear oscillations: Part I: expansion of a constant," *International Journal of Non-Linear Mechanics,* vol. 37, no. 2, pp. 309-314, 2002/03/01/ 2002,

[78]   J. C. Butcher, "A history of Runge-Kutta methods," *Applied Numerical Mathematics,* vol. 20, no. 3, pp. 247-260, 1996/03/01/ 1996,

[79]   A. S. Bernardez, "Nonlinear Normal Modes in Mechanical Systems: Concept and Computation with Numerical Contiuation," PhD., ESCUELA TÉCNICA SUPERIOR DE INGENIEROS INDUSTRIALES, Madrid, 2016.

[80]   A. M. S. Bouchaala, "Size effect of a uniformly distributed added mass on a nanoelectromechanical resonator," *Microsystem Technologies,* vol. 24, no. 6, pp. 2765-2774, 2018/06/01 2018, doi: 10.1007/s00542-018-3752-2.

[81]   W. Thomson, *Theory of vibration with applications*. CrC Press, 1996.

[82]   M. Karakaplan, "Fitting Lorentzian peaks with evolutionary genetic algorithm based on stochastic search procedure," *Analytica Chimica Acta,* vol. 587, no. 2, pp. 235-239, 2007/03/28/ 2007,

Reference List

[83]   E. Süli and D. F. Mayers, *An introduction to numerical analysis*. Cambridge university press, 2003.

[84]   S. Matlab, "Matlab," *The MathWorks, Natick, MA,* 2012.

[85]   M. Despotovic, V. Nedic, D. Despotovic, and S. Cvetanovic, "Evaluation of empirical models for predicting monthly mean horizontal diffuse solar radiation," *Renewable and Sustainable Energy Reviews,* vol. 56, pp. 246-260, 2016/04/01/ 2016

[86]   J. H. Scofield, "A Frequency-domain description of a lock-in amplifier," *American Journal of Physics* Journal vol. 62, 2, pp. 129-133, 1994.

[87]   W. A. Daxwanger and G. K. Schmidt, "Skill-based visual parking control using neural and fuzzy networks," in *1995 IEEE International Conference on Systems, Man and Cybernetics. Intelligent Systems for the 21st Century*, 1995, vol. 2: IEEE, pp. 1659-1664.

[88]   S. Stassi, I. Cooperstein, M. Tortello, C. F. Pirri, S. Magdassi, and C. Ricciardi, "Reaching silicon-based NEMS performances with 3D printed nanomechanical resonators," *Nature Communications,* vol. 12, no. 1, p. 6080, 2021/10/19 2021, doi: 10.1038/s41467-021-26353-1.

[89]   S. T. Bartsch, M. Arp, and A. M. Ionescu, "Junctionless Silicon Nanowire Resonator," *IEEE Journal of the Electron Devices Society,* vol. 2, no. 2, pp. 8-15, 2014, doi: 10.1109/JEDS.2013.2295246.

[90]   James Fernando, Fang Ben, Jun-Yu Ou, and Y. Tsuchiya, "Spectral Characterisation and Tuning Effect of Pico-metre-scale Thermomechanical Motion for Silicon NEMS resonators," *International Conference of Micro and Nano Engineering,* Conference 2021.

[91]   S. Zaitsev, O. Shtempluck, E. Buks, and O. Gottlieb, "Nonlinear damping in a micromechanical oscillator," *Nonlinear Dynamics,* vol. 67, no. 1, pp. 859-883, 2012/01/01 2012, doi: 10.1007/s11071-011-0031-5.